

AD-A188 355

FATIGUE CRACK-GROWTH RESISTANCE OF ALUMINUM ALLOYS
UNDER SPECTRUM LOADING (U) NORTHRUP CORP HAWTHORNE CA
AIRCRAFT GROUP G V SCARICH ET AL DEC 85

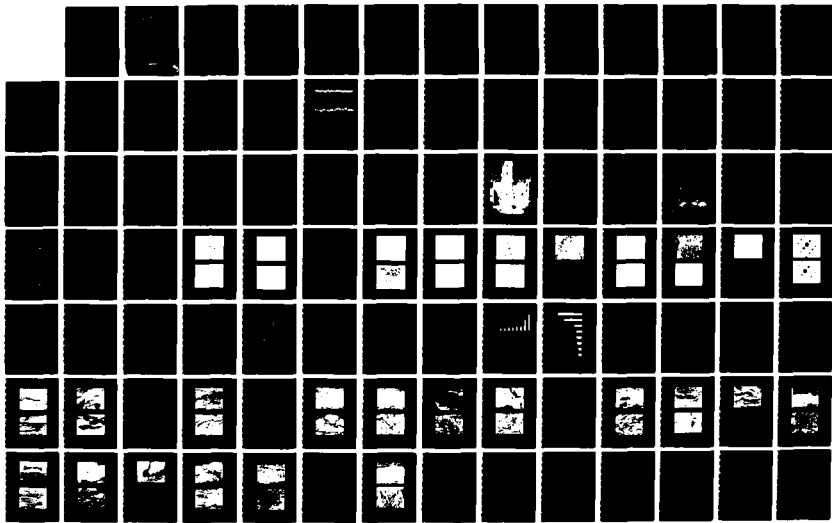
1/2

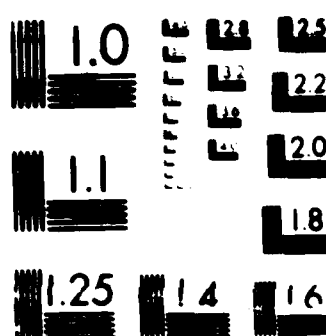
UNCLASSIFIED

NOR-85-141-VOL-2 N00014-82-C-0425

F/G 11/6.1

NL





MICROCOPY RESOLUTION TEST CHART
NATIONAL BUREAU OF STANDARDS

AD-A180 355

①

FATIGUE CRACK-GROWTH RESISTANCE OF ALUMINUM ALLOYS UNDER SPECTRUM LOADING

Volume II — Aluminum Lithium Alloys

G. V. SCARICH
K. M. BRESNAHAN
P. E. BRETZ

NORTHROP CORPORATION
AIRCRAFT DIVISION
ONE NORTHROP AVENUE
HAWTHORNE, CALIFORNIA 90250

DECEMBER 1985
NOR 85-141

TECHNICAL REPORT
FINAL REPORT FOR PERIOD 30 SEPTEMBER 1981 THROUGH 31 MARCH 1985
CONTRACT NO. N00019-82-C-0425

APPROVED FOR PUBLIC RELEASE; DISTRIBUTION IS UNLIMITED

DEPARTMENT OF THE NAVY
NAVAL AIR SYSTEMS COMMAND
WASHINGTON, D.C. 20381

LIBRARY COPY

JAN 24 1986

LANGLEY RESEARCH CENTER
LIBRARY, NASA
HAMPTON, VIRGINIA

NORTHROP

Aircraft Division
Aircraft Group
Northrop Corporation
One Northrop Avenue
Hawthorne, California 90280

MAY 11 1987



87-5-11-027

UNCLASSIFIED

SECURITY CLASSIFICATION OF THIS PAGE

ADA180355

REPORT DOCUMENTATION PAGE

1a. REPORT SECURITY CLASSIFICATION UNCLASSIFIED		1b. RESTRICTIVE MARKINGS	
2a. SECURITY CLASSIFICATION AUTHORITY		3. DISTRIBUTION/AVAILABILITY OF REPORT Approved for public release; distribution is unlimited	
2b. DECLASSIFICATION/DOWNGRADING SCHEDULE			
4. PERFORMING ORGANIZATION REPORT NUMBER(S) NOR 85-141, Volume II		5. MONITORING ORGANIZATION REPORT NUMBER(S)	
6a. NAME OF PERFORMING ORGANIZATION Northrop Corporation Aircraft Division		6b. OFFICE SYMBOL (If applicable)	
6c. ADDRESS (City, State and ZIP Code) One Northrop Avenue Hawthorne, California 90250		7a. NAME OF MONITORING ORGANIZATION Naval Air Systems Command	
7b. ADDRESS (City, State and ZIP Code) Department of the Navy Washington, DC 20301			
8a. NAME OF FUNDING/SPONSORING ORGANIZATION Naval Air Systems Command		8b. OFFICE SYMBOL (If applicable)	
8c. ADDRESS (City, State and ZIP Code) Department of the Navy Washington, D.C. 20361		9. PROCUREMENT INSTRUMENT IDENTIFICATION NUMBER N00019-82-C-0425	
11. TITLE (Include Security Classification) See Cover		10. SOURCE OF FUNDING NOS.	
		PROGRAM ELEMENT NO.	PROJECT NO.
		TASK NO.	WORK UNIT NO.
12. PERSONAL AUTHOR(S) G.V. Scarich, K.M. Bresnahan (Northrop), and P.E. Bretz (Alcoa)			
13a. TYPE OF REPORT Technical Report		13b. TIME COVERED FROM 30 Sept 82 TO 31 Mar 85	
14. DATE OF REPORT (Yr., Mo., Day) DECEMBER 1985		15. PAGE COUNT 120	
16. SUPPLEMENTARY NOTATION Volume I of this report, "Commercial 2XXX and 7XXX Alloys," contains the results of the balance of the effort of this contract.			
17. COSATI CODES			18. SUBJECT TERMS (Continue on reverse if necessary and identify by block number) Aluminum Alloys Fatigue Crack Growth Fracture Toughness Aluminum Lithium Spectrum Loading Constant-Amplitude Loading Microstructure Retardation Variable-Amplitude Loading Temper Planar Slip
19. ABSTRACT (Continue on reverse if necessary and identify by block number) The objective of this program is to develop metallurgical guidelines and test methodologies for selection and development of spectrum fatigue-resistant, high-strength aluminum alloys for aircraft structural application. This volume (II) describes the results of characterizations of six experimental alloys containing substantial amounts of lithium. Chemistry, temper, and grain structure were varied to produce systematically controlled microstructures. The six alloys were characterized for chemical composition, microstructure, tensile properties, and fracture toughness. Fatigue crack propagation (FCP) tests were conducted on specimens of each alloy for both constant-amplitude loading and two F-18 load spectrums. One of the spectrums was dominated by tension loads (TD) and the other spectrum contained tension and compression loads (TC) of nearly equal magnitude. The spectrum FCP testing was performed at the maximum peak stress of 145 MPa (21 ksi). Pertinent fracture surface features were documented on the spectrum fatigue specimens. → <i>Kegel et al</i> → The alloys were also tested using two independent modifications of the baseline (TD and TC) spectrums. One modification, referred to as racetrack (designated TDR or TCR), was used to eliminate 43 percent of the low-amplitude cycles to reduce testing time. The second modification involved the elimination of all compression load points from the TC spectrum (designated TCZ). This modification was made to determine the importance of compressive load cycles. All testing was performed in humid air (relative humidity >90 percent).			
20. DISTRIBUTION/AVAILABILITY OF ABSTRACT UNCLASSIFIED/UNLIMITED <input checked="" type="checkbox"/> SAME AS RPT <input type="checkbox"/> DTIC USERS <input type="checkbox"/>		21. ABSTRACT SECURITY CLASSIFICATION UNCLASSIFIED	
22a. NAME OF RESPONSIBLE INDIVIDUAL W.L. Koegel		22b. TELEPHONE NUMBER (Include Area Code) (212) 692-6025	22c. OFFICE SYMBOL NAVAIR-5304B6

UNCLASSIFIED

SECURITY CLASSIFICATION OF THIS PAGE

An investigation of twelve commercial 2XXX and 7XXX alloys, discussed in Volume I of this report, indicated that strengthening precipitates are a primary microstructural parameter influencing cyclic crack growth. The alloys with a dominant strengthening phase, that is shearable by dislocations, have a greater resistance to spectrum FCP than alloys that are strengthened primarily by non-shearable precipitates. Shearable precipitates allow concentrated planar slip to develop, while nonshearable precipitates tend to homogenize slip through dislocation looping and cross-slip.

The chemistry/temper variants provided by the commercial 2XXX and 7XXX alloys did not result in large systematic differences in the degree of slip planarity. Therefore, the mechanism(s) by which planar slip leads to greater resistance to spectrum FCP, relative to homogeneous deformation, could not be clearly established by the characterization of these alloys. Six alloys with systematically controlled microstructures (SCM) were produced to establish the effect of slip planarity on FCP. Alloys with substantial lithium additions were chosen for evaluation because of the tendency of the Al_3Li (δ') strengthening precipitate to deform by shearing, which leads to concentrated planar slip, especially in underaged conditions. The T-type ($\text{Al}_x\text{Cu}_y\text{Li}_z$) and S' (Al_2CuMg) strengthening phases, which tend to be nonshearable, disperse slip in peak aged conditions.

The nominal compositions of the alloys with SCM were Al-3 Cu-2 Li-0.1 Zr and Al-3 Cu-2 Li-1 Mg-0.1 Zr (weight percentages). Underaged and peak aged tempers of these compositions were studied. The materials were produced in the form of wrought plate. The grain structure consisted of coarse, unrecrystallized, pancake-shaped grains typical of wrought plate in aluminum alloys containing Al_3Zr dispersoid phase. A thermomechanical process (TMP) variant of the Al-3 Cu-2 Li-0.1 Zr composition was also studied to determine the effects of grain structure on spectrum FCP. Although this TMP was intended to result in a fine, recrystallized grain structure, the actual result was a mixture of fine, equiaxed, recrystallized grains and relatively coarse, unrecrystallized, pancake-shaped grains.

The following alloy designation code is used to identify the alloys with SCM. The first two (or three in the Mg-containing alloys) digits of the code indicate the nominal elemental percentages of the major alloying elements (Cu first, Li second, Mg third), the first letter represents grain size (C for coarse, M for mixed), and the last character indicates the temper (U for underaged, A for peak aged).

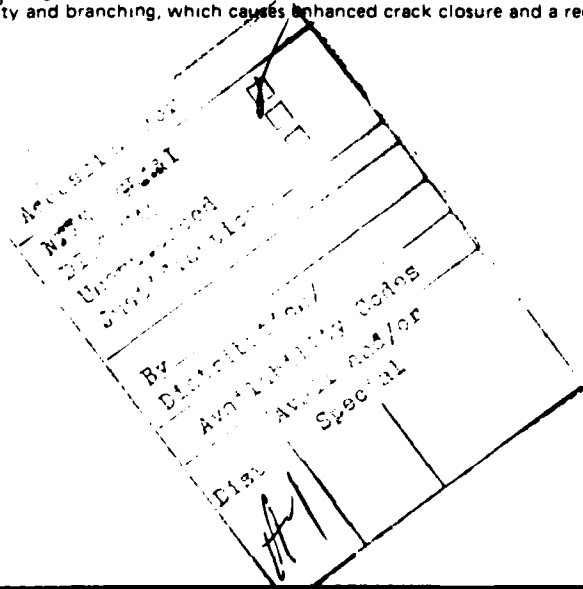
For constant-amplitude FCP ($R = 0.33$), the significant observations were: (1) resistance to FCP is dependent on temper especially in the near-threshold regime, (2) the underaged condition demonstrates greater FCP resistance relative to the peak aged condition for a given chemistry/grain structure, and (3) the 32 Cu alloy possesses the greatest resistance to FCP. All six SCM exhibited rough fracture surfaces, and in some cases, fretting oxide debris covered areas of the fracture surfaces indicating contact between the opposing fracture surfaces.

Several observations can be made based on the TD and TC spectrum FCP test results:

1. The fatigue life was longer in the underaged condition for each alloy chemistry/grain structure relative to the peak aged condition of that alloy, regardless of the particular spectrum.
2. The 32 CU alloy demonstrated greatest FCP resistance to the TD spectrum followed by the 321 CU alloy, while the 321 CU alloy possessed the greatest resistance to the TC spectrum followed by the 32 CU alloy.
3. The underaged alloys showed the greatest difference in life between the TD and TC spectrums, with the 32 CU alloy having only 25 percent of the TD life under the TC spectrum.
4. For a given temper in the Al-Cu-Li-Zr chemistry, the coarse-grained alloys have longer lives than the mixed grain size alloys.
5. The lives of the coarse-grained alloys with and without magnesium are similar for the same temper, but the magnesium-free alloy generally exhibited slightly longer lives.
6. All three of the experimental underaged alloys had longer spectrum fatigue lives than the commercial alloys evaluated in this program (see Volume I of this report).

The relative ranking of the six alloys remained unchanged under the racetrack modification with the exception of the TCR spectrum, where the positions of the 32 CU and 321 CU alloys were reversed. The TCZ spectrum resulted in the longest spectrum life relative to the other spectrums for the underaged condition; however, this trend was not evident for the peak aged condition. The TCZ modification reversed the TC ranking of the 32 CU and the 321 CU alloys, but the relative rankings of the other four alloys remained unchanged. In all of the alloys, the TCZ modified spectrum resulted in longer life relative to the TC spectrum life for a given alloy, indicating that compression loads tend to reduce spectrum fatigue life.

The most significant trend in the FCP data (constant and variable load amplitude) is that the underaged alloys with predominant planar slip deformation had longer fatigue lives than the peak aged that deform more homogeneously. The characteristics of the age-hardening precipitates control the degree of slip planarity, with the predominant strengthening phase being the shearable Al_3Li (δ') in the underaged temper leading to enhanced slip planarity. Concentrated planar slip results in greater crack path tortuosity and branching, which causes enhanced crack closure and a reduction in stress intensity at the crack tip.



UNCLASSIFIED

SECURITY CLASSIFICATION OF THIS PAGE

PREFACE

This report was prepared by the Northrop Corporation, Aircraft Division, Hawthorne, California, under Naval Air Systems Command Contract N00019-82-C-0425. Ms. G. Weaver of Naval Air Systems Command (Code AIR-5304B4) was the project engineer.

Northrop Corporation, Aircraft Division, was the prime contractor, with Mr. G.V. Scarich serving as the program manager. Mr. K.M. Bresnahan was involved in the analysis of the deformation behavior, which included the correlation of fracture features with microstructure. Mr. S. Hsu was responsible for all the spectrum testing and data reduction while Mr. P.G. Porter was responsible for spectrum selection, generation and modification.

Aluminum Company of America, Alcoa Technical Center, was a major participant in the program. Dr. P.E. Bretz served as the Alcoa program manager and Principal Investigator. Alcoa was intimately involved in all the phases of the program and was primarily responsible for determination of baseline mechanical properties, microstructural characterization, and fracture surface/microstructure interpretation.

The contractor report number is NOR 85-141. This report covers work from 30 September 1982 through 31 March 1985, and it consists of two volumes.

Volume I, Commercial 2XXX and 7XXX Alloys

Volume II, Aluminum Lithium Alloys.

The authors also wish to acknowledge R. Schmidt formerly of NAVAIR; A.P. Divecha of NSWC; and B.J. Mays, A.H. Freedman, G.R. Chanani, S.W. Averill, J. Luck, D.R. Drott, J.P. Bouffard and J.M. Wilson of Northrop; J.T. Staley, R.R. Sawtell, and A.K. Vasudevan of Alcoa, for their cooperation and support during the various phases of the program.

CONTENTS

<u>Section</u>		<u>Page</u>
1	INTRODUCTION	1
2	EXPERIMENTAL PROCEDURE	5
2.1	Material Production and Processing	5
2.2	Chemical Analysis and Density Determination	6
2.3	Metallography and Fractography	6
2.4	Tensile Tests	6
2.5	Fracture Toughness Tests	6
2.6	Fatigue-Crack Propagation (FCP) Tests Under Constant Load Amplitude	7
2.7	Spectrum Testing	8
2.7.1	Spectrum Selection and Definition	8
2.7.2	Spectrum Modification	12
2.7.3	Specimen Preparation	23
2.7.4	Testing	25
2.7.5	Test Analysis Procedure	27
3	RESULTS AND DISCUSSION	29
3.1	Chemistry and Density	29
3.2	Microstructural Evaluation	29
3.3	Tensile and Fracture Toughness Results	48
3.4	Fatigue-Crack Growth Results Under Constant Amplitude Loading	48
3.5	Spectrum Test Results	52
3.5.1	Ranking of Materials	58
3.5.2	Spectrum Crack Growth Behavior	58
3.5.3	Effects of Load History	60
3.6	FRACTOGRAPHIC ANALYSIS OF SPECTRUM FATIGUE SPECIMENS	60
3.6.1	Macroscopic Appearance	60
3.6.2	Microscopic Fracture Mechanisms	63
4	SUMMARY AND CONCLUSIONS	83
	REFERENCES	87
<u>Appendix</u>		
A	CONSTANT AMPLITUDE FATIGUE CRACK GROWTH RATE, da/dN VERSUS ΔK	93

CONTENTS (Continued)

<u>Appendix</u>		<u>Page</u>
B	CRACK LENGTH VERSUS SIMULATED FLIGHT HOURS a VERSUS H	101
C	SPECTRUM CRACK GROWTH RATE VERSUS MAXIMUM PEAK STRESS INTENSITY da/dH VERSUS K_{hmax}	109

ILLUSTRATIONS

<u>Figure</u>		<u>Page</u>
1	Representative Portions of Stress History of Each Spectrum	9
2	Definition of Terms	10
3	Spectrum Generation Procedure	12
4	Exceedance Curves	13
5	Racetrack Method of Spectrum Modification	21
6	Spectrum Specimen	24
7	Spectrum Test Setup	26
8	Comparison of Ranges of K_{hmax} Vs a	27
9	Microstructure	30
10	Location of the Six Rolling Texture Components in (111) Pole Figure Usually Found in Aluminum Alloy, Plotted in One Quadrant	32
11	(111) Pole Figures for the Three Microstructures Showing Incomplete Rolling Textures.....	33
12	Alloy 321C8	36
13	Alloy 321CU	39
14	Alloy 32CU	41
15	Alloy 32C8	43
16	Alloy 32MX	44
17	Alloy 32MX Electron Diffraction Patterns	46
18	Yield Strength Versus Fracture Toughness	50
19	Constant Load Amplitude Fatigue Crack Growth Rate Data....	51
20	Stress Intensity Needed to Obtain a Given Fatigue-Crack Growth Rate Under Constant Amplitude Loading	53
21	Spectrum Fatigue Lives.....	55
22	Spectrum Fatigue Lives for TD and TC Spectrums	56
23	Spectrum FCGR Curves.....	57
24	Maximum Peak Stress Intensity Needed to Obtain a Given Spectrum FCGR.....	59

ILLUSTRATIONS (Continued)

<u>Figure</u>		<u>Page</u>
25	Fracture Surface of Alloy 32C8, TD Spectrum, Showing Relatively Coarse Surface Topography.....	61
26	Fracture Surface of Alloy 32CU, TD Spectrum, Showing Extremely Coarse Surface Topography	62
27	Fracture Surface of Alloy 32C8, TD Spectrum, at $a = 6.4 \text{ mm}(0.25 \text{ in.})$	64
28	Fracture Surface of Alloy 32C8, TD Spectrum, at $a = 19.2 \text{ mm} (0.75 \text{ in.})$	66
29	Fracture Surface of Alloy 32CU, TD Spectrum	67
30	Fracture Surface of Alloy 32CU, TD Spectrum, at $a = 19.1 \text{ mm} (0.75 \text{ in.})$	68
31	Fracture Surface of Alloy 321CU, TD Spectrum, at $a = 6.4 \text{ mm} (0.25 \text{ in.})$	69
32	Fracture Surface of Alloy 321C8, TD Spectrum, at $19.1 \text{ mm} (0.75 \text{ in.})$	71
33	Fracture Surface of Alloy 32M8, TD Spectrum, at $a = 6.4 \text{ mm} (0.25 \text{ in.})$	74
34	Fracture Surface of Alloy 32M8, TD Spectrum, at $19.1 \text{ mm} (0.75 \text{ in.})$	75
35	Fracture Surface of Alloy 32CU, TC Spectrum	76
36	Fracture Surface of Alloy 321C8, TC Spectrum.....	78
37	Fracture Surface of Alloy 321CU, TC Spectrum	79
38	Fracture Surface of Alloy 32MU, TC Spectrum	81

TABLES

<u>Table</u>		<u>Page</u>
1	Spectral Density Function	14
2	Peak/Valley Coupling Matrix	16
3	Measured Compositions and Densities.....	29
4	Guinier X-ray Results Showing Relative Volume Fractions of Phases Present	35
5	Tensile and Fracture Toughness Results	49
6	Stress Intensity Range to Obtain a Given Fatigue- Crack Growth Rate Under Constant-Amplitude Loading	54
7	Spectrum Fatigue Results	54
8	Ranking of Materials in Spectrum Fatigue by Maximum Peak Stress Intensity to Obtain a Given Fatigue Crack Growth Rate.....	59

ABBREVIATIONS AND SYMBOLS

a	Crack-length
a_i	Initial crack length
a_c	Current crack length
a_f	Final crack length
B	Specimen thickness
COD	Crack opening displacement
da/dH	Spectrum crack-growth rate
da/dN	Crack-growth rate (constant amplitude)
F	Failure
FCGR	Fatigue-crack growth rate
FCP	Fatigue-crack propagation
H	Simulated flight hours or half height of compact tension specimen
K	Stress-intensity factor
K_{eff}	Effective stress intensity
K_{hmax}	Stress-intensity factor at largest (highest) peak of spectrum
K_{hmin}	Stress-intensity factor at smallest (lowest) valley of spectrum
K_{max}	Maximum stress intensity factor
K_{Ic}	Plane strain fracture toughness
K_Q	Conditional fracture toughness, test did not meet all the ASTM E399 validity criteria
L	Longitudinal
L-T	Crack growth on plane normal to the longitudinal direction (L) of the plate in a direction transverse (T) to the longitudinal (rolling) direction (per ASTM E399)
N	Number of cycles
P	Load
P_{cl}	Crack closure load
P_{hmax}	Load at largest (highest) peak of a spectrum
P_{hmin}	Load at smallest (lowest) valley in a spectrum
P_{max}	Peak load
P_{sm}	Mean spectrum load

1. INTRODUCTION

The survey of spectrum fatigue behavior for commercial 2XXX and 7XXX aluminum alloys conducted in Phases I and II⁽¹⁻⁴⁾ of this study suggested that a primary microstructural parameter which influences cyclic crack growth is the nature of precipitation (i.e., temper), which controls slip character. When the presence of metastable precipitates permits slip to be inhomogeneous (planar), fatigue crack propagation (FCP) rates are lower than when incoherent precipitates encourage homogeneous deformation by dislocation looping.

Although not addressed specifically in Phases I and II, the influence of grain structure on FCP resistance has been thoroughly documented in the literature.⁽⁵⁻¹⁴⁾ The theme which runs throughout this variety of work on Ti alloys, steels, Ni-based superalloys, and aluminum alloys is that increased grain size reduces crack growth rates substantially, particularly in the near-threshold region. Bretz, et al.,⁽¹³⁾ addressed specifically the case of aluminum alloys, and showed that grain size effects are due to a combination of crack closure and crack deflection/branching mechanisms. Vasudevan and Bretz⁽¹⁴⁾ recently reviewed microstructural effects on FCP in aluminum alloys, and Suresh⁽¹⁵⁻¹⁶⁾ has provided a model to explain both closure and deflection/branching effects.

The decision to use Al-Li alloys as the basis for systematically-controlled microstructures (SCM) in the current phase was made with the foregoing metallurgical effects on FCP behavior in mind. The tendency of these alloys, particularly binary Al-Li, to deform by planar slip as a result of shearing of the coherent Al_3Li (δ') precipitates has been known for some time. An early study by Sanders⁽¹⁷⁾ and a recent review of Al-Li metallurgical fundamentals⁽¹⁸⁾ discuss this relationship between precipitation and planar slip. The ability to change the degree of slip planarity in Al-Li alloys by varying aging treatment is of particular interest. In binary Al-Li alloys, planar slip is enhanced as aging progresses toward peak strength. This tendency toward coarse planar slip gradually decreases as overaging leads to a

reduction in the volume fraction of coherent Al_3Li precipitates and an increase in the amount of equilibrium AlLi (δ) phase. The δ is incoherent and tends to form at grain boundaries, with the subsequent development of a δ' PFZ. The δ phase also can precipitate within grains, and its nonshearable nature results in dislocation looping and greater homogeneity of deformation within these grains. As will be discussed later in this report, however, the influence of aging on slip planarity in ternary and quaternary alloys is somewhat different.

Wrought product grain structure in Al-Li alloys frequently is controlled by additions of Zr, which forms the Al_3Zr phase. This precipitate acts as a dispersoid to prevent grain boundary migration,⁽¹⁷⁾ and usually results in an unrecrystallized microstructure in the final product. One method to vary grain size/structure is to intentionally omit Zr from the alloy to obtain a totally recrystallized, large-grained alloy. In the present work, we chose instead to use thermomechanical processing to vary grain structure in alloys of otherwise identical composition, including Zr content. The goal was to obtain two structures: one, an unrecrystallized structure with a relatively large high-angle boundary spacing (a coarse structure); and the other, a recrystallized alloy with a small grain size (a fine structure). These two structures would permit an examination of grain size effects directly.

The particular choice of Al-Li alloy compositions was aided by the early work of Sanders⁽¹⁷⁾ and by extensive alloy development activities ongoing at Alcoa. Sanders had shown that Al-Cu-Li alloys had substantially higher strength potential than those from the Al-Mg-Li system; furthermore, the latter suffer from the tendency to form grain boundary Al_2MgLi precipitates, which reduce elongation to failure and toughness significantly. Of course, high strength is a particularly desirable feature in aerospace alloys, so that an Al-Cu-Li alloy would be a natural choice. In addition, the first commercial Al-Li alloy, 2020, was of the Al-Cu-Li family, so much was known about this system. Internal Alcoa alloy development activities already had identified an alloy of this type which appeared to have very attractive properties for aerospace application. Subsequently, this alloy composition was refined and has been registered with the Aluminum Association as 2090 (Al-2.7Cu-2.2Li-0.12Zr); this alloy is designed to be a replacement for high-strength, 7075-T6X products at a 7 percent density reduction.⁽¹⁹⁾ Additional studies

of the Al-Cu-Li system were going on concurrently in a separate NAVAIR-funded contract⁽²⁰⁾ to study fatigue, fracture, and corrosion behavior of Al-Li alloys. This work was expected to provide substantial background information on the alloy system and permit cross-fertilization of ideas.

Because the Al-Cu-Li system appeared very attractive for study, we decided to look at both aging (i.e., deformation mode) and grain structure effects in a nominally Al-3Cu-2Li-0.12Zr alloy (identical composition to that in Reference 20). Similarly, we chose an Al-3Cu-2Li-1Mg-0.12Zr alloy because background information on it also was anticipated from the work of Vasudevan.⁽²⁰⁾ Quaternary alloys from this system (Al-Cu-Li-Mg) have been studied extensively, and several with commercial potential have been registered recently (AA designations 8090, 8091, 8092). Thus, the Al-Li alloy choices were made to make the best use of available information and to permit study of compositions which appeared to have commercial potential at the time (1982-1983).

2. EXPERIMENTAL PROCEDURE

The six alloys with systematically controlled microstructures (SCM) were produced and evaluated as described below. The evaluation procedures were the same as those used in Phase II of this program.⁽²⁾

The acceptability of each alloy was verified by chemical composition analysis and by tensile and fracture toughness (K_{Ic}) tests as described in this section. Also described in this section are the fatigue crack-growth test procedures, the background on the spectra selected for use in the program, and the modifications of these spectra.

2.1 MATERIAL PRODUCTION AND PROCESSING

The alloys were cast into ingots weighing nominally 36 kg. (80 lb.), using facilities at the Alcoa Technical Center. After a high-temperature soaking cycle to homogenize the composition, the ingots were scalped to rolling sections and rolled to 7.6-mm (0.30-inch) thick plate. This gauge was chosen to maximize the amount of product obtained while providing the minimum of 6.4 mm (0.25 inch) desired for FCG specimens. The alloys with varied grain size were fabricated using a different thermomechanical processing (TMP) schedule than was used for the other alloys, in order to change the grain structure. Since, however, TMP technology is not the subject of this contract, the actual rolling schedules and thermal practices used will not be discussed.

After fabrication, each plate was solution heat treated, cold water quenched, and stretched 2 percent to relieve residual stresses. For the Al-3Cu-2Li-0.1Zr alloy chemistry, the solution treatment temperature was 552°C (1025°F); for the Al-3Cu-2Li-1Mg-0.1Zr alloy chemistry, 527°C (980°F). The aging treatments consisted of 16 hours at either 163°C (325°F) or 190°C (375°F) to produce underaged or peak aged structures, respectively.

2.2 CHEMICAL ANALYSIS AND DENSITY DETERMINATION

The chemical composition of each of the plates was determined on remelt samples of material (about 65 g each) cut from the plates. A quantometer (atomic emission spectrometer) interfaced with a minicomputer was used to obtain the analyses.

The density was determined by displacement in water.

2.3 METALLOGRAPHY AND FRACTOGRAPHY

Specimens for optical metallography were taken from each alloy plate to ensure that the observed microstructures were typical of those in the spectrum specimens. Standard metallographic procedures were used in preparing all the specimens. The specimens were examined both in the as-polished condition and following etching with Keller's reagent. Specimens for fractographic analysis were cleaned ultrasonically in an acetone bath, rinsed in alcohol, and gold-coated to improve resolution. Fractographs of the fracture surface of each specimen were obtained at crack lengths, a , of 6.4 mm (0.25 inch) and 19 mm (0.75 inch), using a scanning electron microscope (SEM).

2.4 TENSILE TESTS

Tensile tests were conducted in accordance with ASTM Standard Method B557. All tests were performed at room temperature in laboratory air on specimens taken in the longitudinal (L) orientation with respect to the rolling direction.

2.5 FRACTURE TOUGHNESS TESTS

The SCM alloys were produced in a thickness (0.3-inch) which precluded valid plane strain K_{Ic} testing per ASTM Standard Test Method E399, even in peak strength temper. To estimate the toughness of these alloys, a three-point slow bend test was used. This test is conducted in accordance with ASTM Standard Test Method E812-81 for determining the crack strength of high-strength metallic materials. The test data are analyzed using an equation suggested by Ronald, et al.,⁽²¹⁾ to calculate an indicator toughness value K_{Ich} , in fracture mechanics units. This relationship is:

$$K_{ICh}^2 = \frac{E}{2(1 - \nu^2)} \cdot (W/A),$$

where E is the elastic modulus, ν is Poisson's ratio, W is the energy absorbed during fracture, and A is the cross-sectional area of the uncracked ligament. Alcoa experience with this test suggests that there is a one-to-one correlation between K_{Ic} and the indicator value K_{ICh} up to about 35 ksi $\sqrt{\text{in.}}$, beyond which the indicator value exceeds K_{Ic} .

2.6 FATIGUE-CRACK PROPAGATION (FCP) TESTS UNDER CONSTANT LOAD AMPLITUDE

Constant load amplitude FCP tests were conducted over low, intermediate, and high-stress intensity factor ranges (ΔK) on modified C(T) specimens ($B = 6.4$ mm (0.25 inch), $W = 64.8$ mm (2.55 inch), and $H/W = 0.486$) in the longitudinal (L-T) orientation. All testing was performed on closed loop, servo-hydraulic test machines at a load ratio ($R = P_{\min}/P_{\max}$) equal to 0.33 and at a test frequency of 25 Hz. The test environment was room temperature laboratory air with high humidity (relative humidity > 90 percent).

The precracking of each specimen was conducted at R of 0.33 with visual crack length measurement. Upon attaining the desired precrack length, a , an automated test system utilizing a computer for data acquisition and machine control was used to obtain the crack-growth rate (da/dN) data. Crack length was monitored continuously by an elastic compliance technique, enabling the stress intensity factor, K, to be controlled according to the equation:

$$K = K_0 \exp [C (a_c - a_i)]$$

where K_0 is the initial cyclic stress intensity corresponding to the starting crack length, a_i ; a_c is the current crack length, and C is the constant with the dimension of 1/length.⁽²²⁾ A double cantilever clip-on displacement gage was used for monitoring crack opening displacements (CODs). The K-decreasing tests (near-threshold) were conducted using a value for the parameter C of -0.059 mm^{-1} (-1.5 inch^{-1}), and the K-increasing tests (intermediate and high K) were conducted using values of C between 0.069 mm^{-1} (1.75 inch^{-1}) and 0.098 mm^{-1} (2.5 inch^{-1}). Several visual crack

length measurements were also made during each test to verify the compliance measurements.

The test procedures strictly adhered to the ASTM Standard Test Method E647 for "Constant-Load-Amplitude Fatigue Crack-Growth Rates Above 10^{-8} m/Cycle," and to the proposed ASTM Standard test practice for measurement of near-threshold growth rates, $da/dN 10^{-8}$ m/cycle.⁽²³⁾

The crack-closure load (P_{cl}) was monitored periodically by recording the load (P) and COD signals and plotting P versus COD. The series of P_{cl} data as a function of crack length were then used to calculate ΔK_{eff} values, where $\Delta K_{eff} = P_{max} - P_{cl}$.

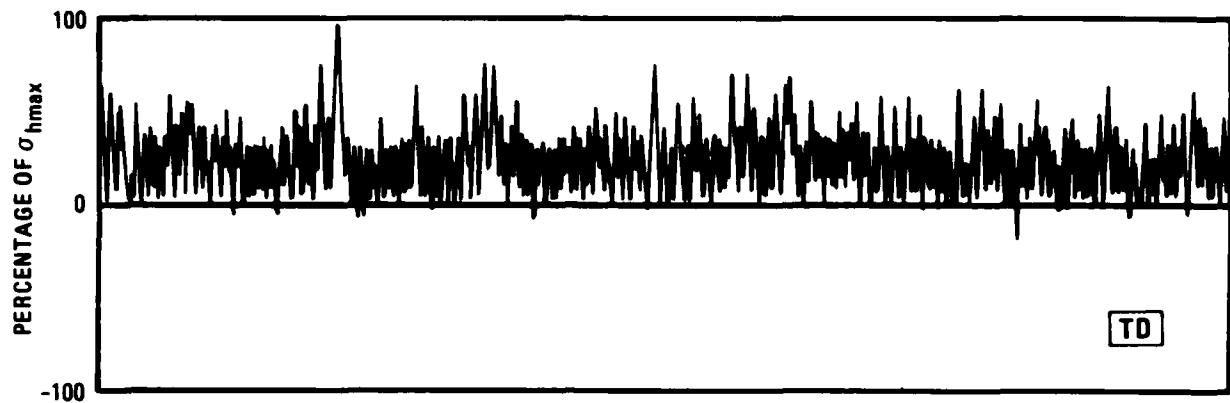
2.7 SPECTRUM TESTING

Two different F-18 spectrums were selected for this program. Also, these two spectrums were modified to reveal effects of compression load cycles and small amplitude load cycles and to shorten the testing time. These additional spectrums resulted from these modifications. Using these five spectrums, the six materials in the program were evaluated for their spectrum fatigue-crack growth behavior. In this section, the spectrums, modifications, and spectrum test procedures and analysis are described.

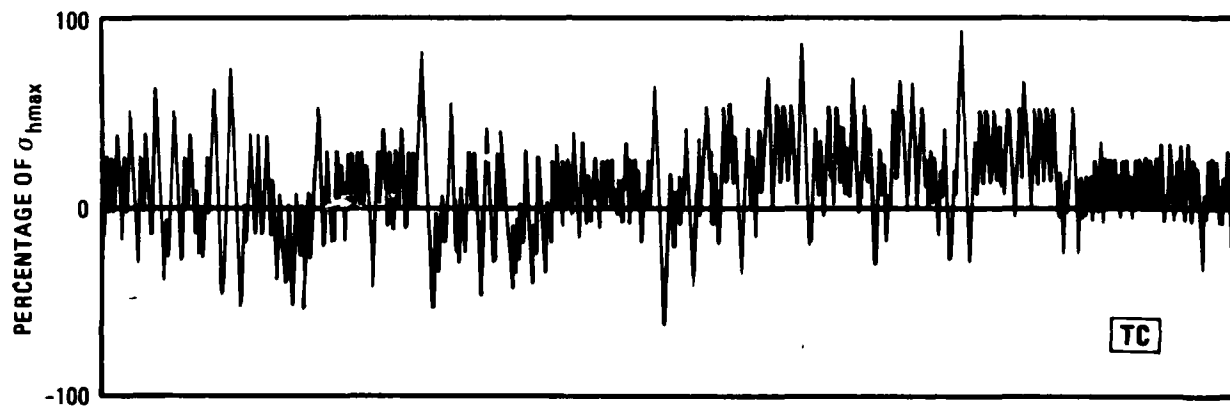
2.7.1 Spectrum Selection and Definition

Portions of the two F-18 spectrums are shown in Figure 1, while Figure 2 shows the terminology used to describe spectrum test parameters. One is a tension-dominated spectrum representing the lower wing root load history; and the other is a tension-compression spectrum representing the horizontal tail hinge moment load history. Both spectrums were computer-generated for the two components of the same aircraft assuming an identical sequence of events.

One "pass" of this basic event spectrum consists of a sequence of 250 flights representing 300 flight hours. One pass of the tension-dominated (TD) spectrum (wing root) has 4,705 load peaks and an equal number of valleys while the tension-compression (TC) spectrum (horizontal tail hinge) has 7,852 load peaks and an equal number of valleys. Since the service life of the F-18 aircraft is 6,000 hours, one service life is obtained by completion of

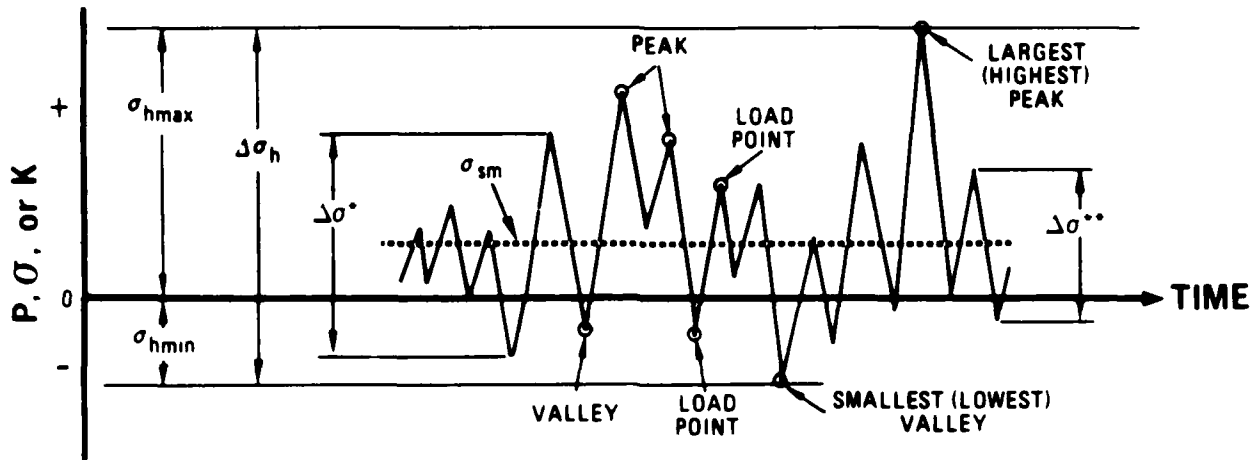


a. TENSION-DOMINATED SPECTRUM (WING ROOT)



b. TENSION-COMPRESSION SPECTRUM (HORIZONTAL TAIL HINGE)

FIGURE 1. REPRESENTATIVE PORTIONS OF STRESS HISTORY OF EACH SPECTRUM



- P_{\max} , σ_{\max} , OR K_{\max} = PEAK LOAD, STRESS, OR STRESS INTENSITY FACTOR
- P_{\min} , σ_{\min} , OR K_{\min} = MINIMUM LOAD, STRESS, OR STRESS INTENSITY FACTOR
- ΔP , $\Delta \sigma$, OR ΔK = RANGE OF LOAD, STRESS, OR STRESS INTENSITY FACTOR: ALGEBRAIC DIFFERENCE BETWEEN SUCCESSIVE VALLEY AND PEAK (POSITIVE OR INCREASING) OR BETWEEN SUCCESSIVE PEAK AND VALLEY (NEGATIVE OR DECREASING)
- $P_{h\max}$, $\sigma_{h\max}$, OR $K_{h\max}$ = LOAD, STRESS, OR STRESS INTENSITY FACTOR AT LARGEST (HIGHEST) PEAK OF A SPECTRUM
- $P_{h\min}$, $\sigma_{h\min}$, OR $K_{h\min}$ = LOAD, STRESS, OR STRESS INTENSITY FACTOR AT SMALLEST (LOWEST) VALLEY, I.E., THE LOWEST ALGEBRAIC VALUE IN A SPECTRUM
- ΔP_h , $\Delta \sigma_h$, OR ΔK_h = OVERALL LOAD, STRESS, OR STRESS INTENSITY RANGE, I.E., THE ALGEBRAIC DIFFERENCE BETWEEN THE LARGEST PEAK AND THE SMALLEST VALLEY OF A SPECTRUM
- P_{sm} OR σ_{sm} = SPECTRUM MEAN LOAD OR STRESS, ALGEBRAIC AVERAGE OF ALL THE PEAK AND VALLEY STRESSES OR LOADS OF A SPECTRUM

NOTES: 1. STRESS IS GROSS STRESS
 2. STRESS INTENSITY IS A FUNCTION OF CRACK LENGTH
 *ALSO CALLED POSITIVE OR INCREASING LOAD RANGE
 **ALSO CALLED NEGATIVE OR DECREASING LOAD RANGE

FIGURE 2. DEFINITION OF TERMS

the total of 20 passes of the above sequence. The F-18 is designed to last four lifetimes, i.e., 24,000 flight hours.

The F-18 was used as a basis for selection of spectrums, stresses, and lives; therefore, a very brief and simplified description of the F-18 design follows. The F-18 (more precisely, F/A-18A) is a Navy carrier-based fighter/attack aircraft. The life requirements for analysis of components are based on both durability and damage tolerance criteria. These criteria differ from the U.S. Air Force requirements of MIL-A-83444 in which the damage tolerance is based on fatigue crack-growth from assumed initial flaws to

various inspectability criteria. The F-18 durability and damage tolerance requirements include various combinations of fatigue-crack initiation, assumed initial flaws, and growth requirements with a different number of lifetimes for each combination. The initial flaw size (or initiation) requirements are less severe than the Air Force requirements; however, the F-18 must endure more severe spectra and longer inspection intervals.

A discussion of the spectrum generation procedure follows, and a schematic chart of the procedure is shown in Figure 3. The first 100 flights out of a total of 250 flights are carrier operations which initiate with a catapult launch and end with an arrested landing. The following 150 flights are field operations ending with a field landing. Field carrier landing practices are also dispersed at intervals during the field operation phase of the spectrum.

Each flight is flown at one of four critical points defined by a weight, speed, and altitude. Symmetrical events (pitch and level flight) within a flight are defined by a peak and valley load factor (n_z) sequence. Asymmetric conditions (rolls) are defined by a given roll rate (p) which gives a positive and negative load perturbation to the associated symmetrical load. Landings are defined by type (arrested landings, touch-and-go, field, etc.) and sink speed.

The load sequence for a particular location on the aircraft structure is obtained for each defined event from a table linking load magnitude with load factor (n_z) at each critical point condition; roll rate and load factor at each critical point condition; and with sink speed for each type of landing. The table is obtained from the results of a finite element model run of the complete structure loaded by a range of unit conditions. The load values are normalized by dividing them by the load for a reference condition. This normalized load sequence is then "laundered" to eliminate small perturbations and "pass through" event peaks which are smaller than the valley of the previous event. After the laundering operation, the final load sequence is stored on a permanent file to be called up for analysis or the creation of a test tape. A listing of the spectrum is also made available in the cycle-by-cycle format. Exceedance data are summarized in the form of a graph, a table of peak and valley occurrences (spectral density function), and a tabular matrix of peak-valley couplings tabulated in increments of five percent of the maximum

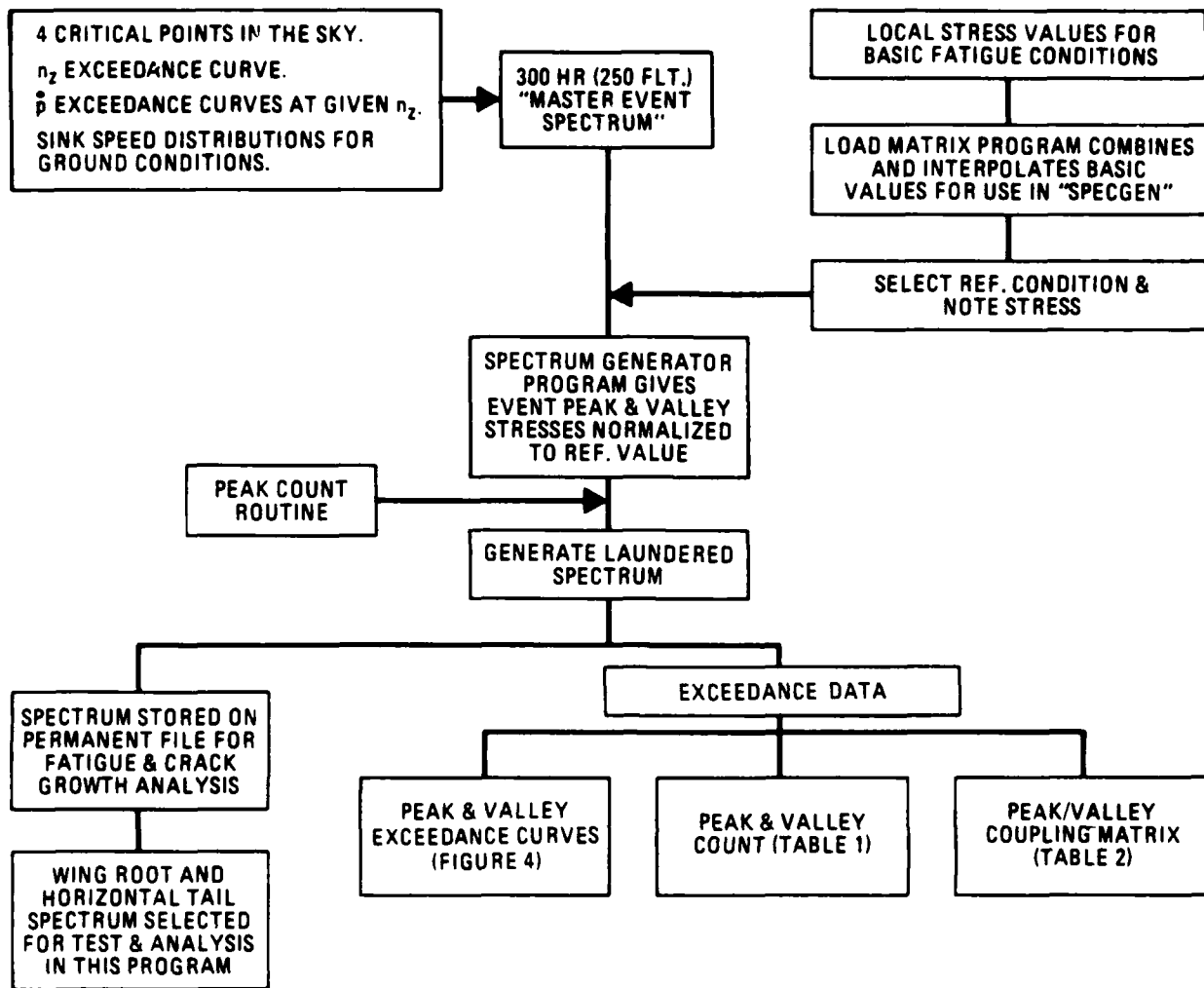
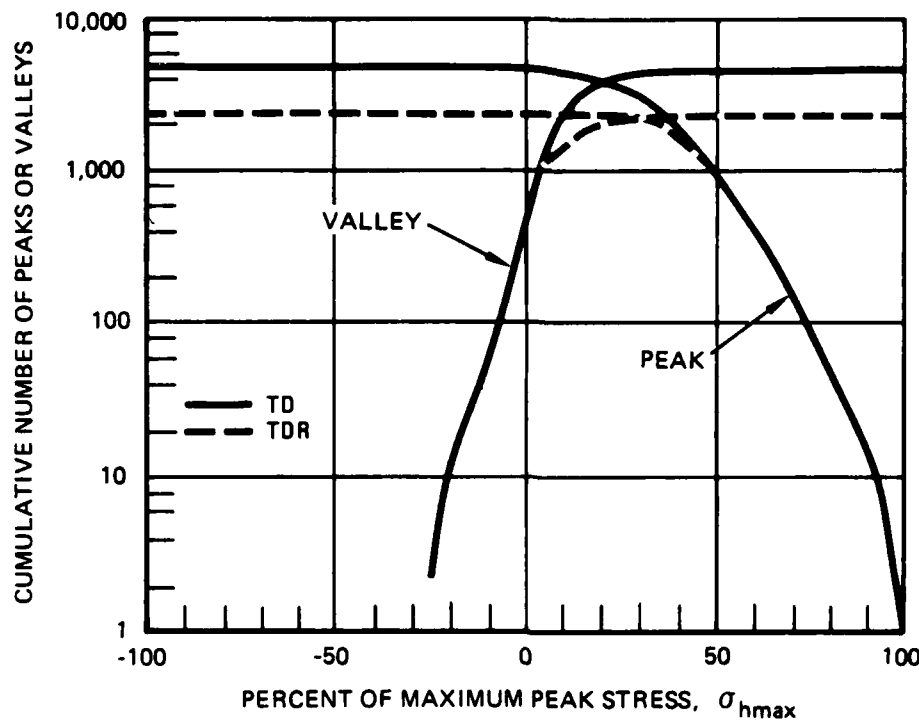


FIGURE 3. SPECTRUM GENERATION PROCEDURE

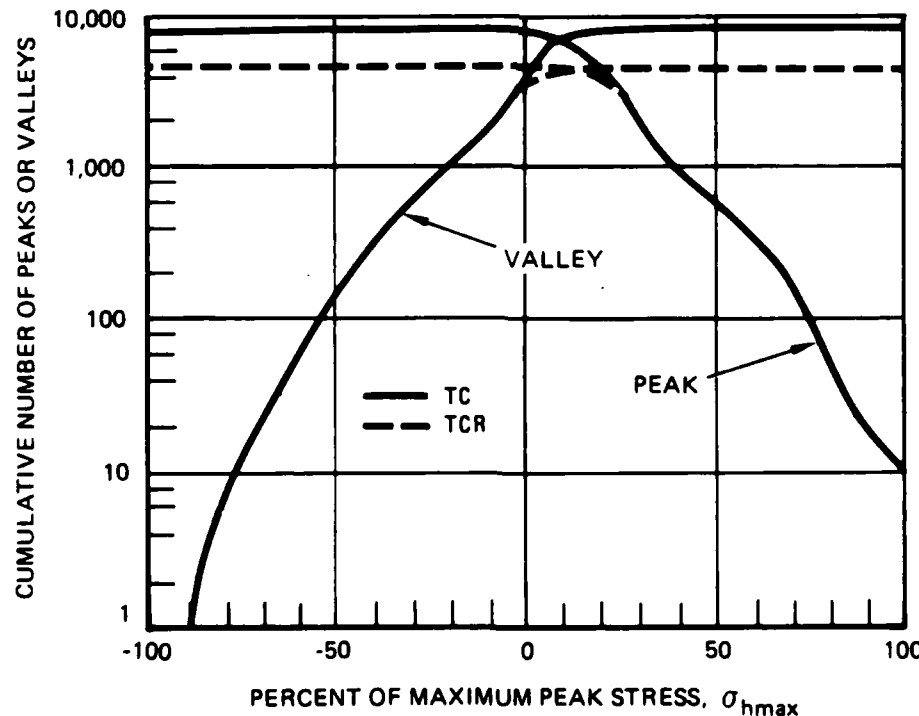
spectrum load. These summaries for the spectrums used are presented in Figure 4 and Tables 1 and 2.

2.7.2 Spectrum Modification

Two modifications were performed independently on the baseline spectra. One modification had two goals: (1) to eliminate low amplitude cycles to reduce testing time without changing the ranking (relative life), and (2) to determine the importance of low amplitude cycles on the overall spectrum life. The second modification was made to determine the importance of compression cycles.



a. TENSION-DOMINATED SPECTRUM (WING ROOT)



b. TENSION-COMPRESSION SPECTRUM (HORIZONTAL TAIL HINGE)

FIGURE 4. EXCEEDANCE CURVES

TABLE 1. SPECTRAL DENSITY FUNCTION

a. TENSION-DOMINATED (WING ROOT) SPECTRUM AND RACETRACK MODIFIED VERSION

PERCENT OF MAXIMUM PEAK LOAD	NUMBER OF EVENTS ^a TD (TDR)				
	PEAKS TD	VALLEYS TD	AMPLITUDES ^b TD	MEAN LEVELS ^c TD	
P = 100	1 (1)	— —	0 (0)	— —	
95 ≤ P < 100	7 (7)	0 (0)	0 (0)	0 (0)	
90 ≤ P < 95	8 (8)	0 (0)	0 (0)	0 (0)	
85 ≤ P < 90	14 (14)	0 (0)	0 (0)	0 (0)	
80 ≤ P < 85	20 (20)	0 (0)	0 (0)	0 (0)	
75 ≤ P < 80	42 (41)	0 (0)	0 (0)	0 (0)	
70 ≤ P < 75	63 (64)	0 (0)	0 (0)	0 (0)	
65 ≤ P < 70	112 (109)	0 (0)	0 (0)	5 (2)	
60 ≤ P < 65	189 (182)	1 (0)	0 (0)	15 (5)	
55 ≤ P < 60	123 (116)	1 (0)	0 (0)	17 (10)	
50 ≤ P < 55	367 (257)	2 (0)	2 (1)	60 (26)	
45 ≤ P < 50	379 (344)	3 (0)	12 (17)	144 (81)	
40 ≤ P < 45	560 (788)	11 (3)	24 (34)	351 (250)	
35 ≤ P < 40	770 (529)	42 (2)	89 (108)	620 (379)	
30 ≤ P < 35	978 (444)	69 (4)	258 (323)	943 (700)	
25 ≤ P < 30	99 (47)	169 (20)	565 (667)	1706 (1140)	
20 ≤ P < 25	168 (0)	305 (45)	1085 (1219)	2198 (1438)	
15 ≤ P < 20	98 (0)	437 (111)	2274 (2032)	1355 (1037)	
10 ≤ P < 15	335 (0)	589 (301)	2290 (856)	453 (200)	
5 ≤ P < 10	372 (0)	1192 (685)	1210 (0)	1348 (33)	
0 ≤ P < 5	0 (0)	1345 (922)	1601 (0)	187 (6)	
-5 ≤ P < 0	0 (0)	404 (400)	— —	6 (0)	
-10 ≤ P < -5	0 (0)	91 (91)	— —	2 (0)	
-15 ≤ P < -10	0 (0)	21 (21)	— —	0 (0)	
-20 ≤ P < -15	0 (0)	11 (11)	— —	0 (0)	
-25 ≤ P < -20	0 (0)	10 (10)	— —	0 (0)	
-30 ≤ P < -25	0 (0)	2 (2)	— —	0 (0)	
-35 ≤ P < -30	0 (0)	0 (0)	— —	0 (0)	
-40 ≤ P < -35	0 (0)	0 (0)	— —	0 (0)	
-45 ≤ P < -40	0 (0)	0 (0)	— —	0 (0)	
-50 ≤ P < -45	0 (0)	0 (0)	— —	0 (0)	
-55 ≤ P < -50	0 (0)	0 (0)	— —	0 (0)	
-60 ≤ P < -55	0 (0)	0 (0)	— —	0 (0)	
-65 ≤ P < -60	0 (0)	0 (0)	— —	0 (0)	
-70 ≤ P < -65	0 (0)	0 (0)	— —	0 (0)	
-75 ≤ P < -70	0 (0)	0 (0)	— —	0 (0)	
-80 ≤ P < -75	0 (0)	0 (0)	— —	0 (0)	
-85 ≤ P < -80	0 (0)	0 (0)	— —	0 (0)	
-90 ≤ P < -85	0 (0)	0 (0)	— —	0 (0)	
-95 ≤ P < -90	0 (0)	0 (0)	— —	0 (0)	
-100 < P < -95	0 (0)	0 (0)	— —	0 (0)	
P = -100	— —	0 (0)	— —	0 (0)	
TOTALS	4705 (2629)	4705 (2628)	9410 (5257)	9410 (5257)	

a SEE FIGURE 3 FOR DEFINITION OF TERMS

b ONE HALF OF LOAD RANGE

c AVERAGE OF PEAK AND VALLEY LOADS

TABLE 1. SPECTRAL DENSITY FUNCTION (Concluded)

b. TENSION-COMPRESSION (HORIZONTAL TAIL HINGE MOMENT) SPECTRUM AND MODIFICATIONS

PERCENT OF MAXIMUM PEAK LOAD	NUMBER OF EVENTS ^a , [TCZ] TC (TCR)											
	PEAKS [TCZ] TC (TCR)			VALLEYS [TCZ] TC (TCR)			AMPLITUDES ^b [TCZ] TC (TCR)			MEAN LEVELS ^c [TCZ] TC (TCR)		
	[10]	10	(10)	[0]	0	(0)	[0]	0	(0)	[0]	0	(0)
P = 100	[10]	10	(10)	-	-	-	[0]	0	(0)	-	-	-
95 ≤ P < 100	[7]	7	(7)	[0]	0	(0)	[0]	0	(0)	[0]	0	(0)
90 ≤ P < 95	[2]	2	(2)	[0]	0	(0)	[0]	0	(0)	[0]	0	(0)
85 ≤ P < 90	[22]	22	(22)	[0]	0	(0)	[0]	1	(1)	[0]	0	(0)
80 ≤ P < 85	[20]	20	(20)	[0]	0	(0)	[0]	3	(3)	[0]	0	(0)
75 ≤ P < 80	[19]	19	(19)	[0]	0	(0)	[0]	0	(0)	[0]	0	(0)
70 ≤ P < 75	[84]	84	(84)	[0]	0	(0)	[0]	6	(7)	[0]	0	(0)
65 ≤ P < 70	[47]	47	(47)	[0]	0	(0)	[0]	19	(21)	[0]	0	(0)
60 ≤ P < 65	[121]	121	(121)	[0]	0	(0)	[0]	79	(81)	[0]	0	(0)
55 ≤ P < 60	[3]	3	(3)	[0]	0	(0)	[0]	24	(34)	[5]	5	(5)
50 ≤ P < 55	[319]	319	(319)	[0]	0	(0)	[13]	67	(83)	[18]	5	(2)
45 ≤ P < 50	[84]	84	(84)	[0]	0	(0)	[18]	154	(187)	[27]	16	(12)
40 ≤ P < 45	[398]	398	(398)	[0]	0	(0)	[79]	125	(186)	[98]	50	(44)
35 ≤ P < 40	[126]	126	(108)	[0]	0	(0)	[201]	450	(510)	[224]	99	(72)
30 ≤ P < 35	[881]	881	(839)	[0]	0	(0)	[292]	423	(533)	[582]	529	(433)
25 ≤ P < 30	[2037]	2037	(1994)	[0]	0	(0)	[435]	998	(1163)	[494]	214	(152)
20 ≤ P < 25	[296]	296	(130)	[0]	0	(0)	[918]	1896	(1997)	[1016]	563	(373)
15 ≤ P < 20	[556]	556	(98)	[0]	0	(0)	[2093]	2077	(1862)	[2169]	1383	(1025)
10 ≤ P < 15	[1208]	1208	(63)	[237]	237	(134)	[4737]	4974	(2355)	[4479]	4794	(3736)
5 ≤ P < 10	[1273]	1273	(68)	[377]	377	(80)	[3069]	2835	(2)	[3695]	2504	(1355)
0 ≤ P < 5	[200]	201	(32)	[7099]	1621	(165)	[3571]	2373	(0)	[2619]	3127	(744)
-5 ≤ P < 0	[0]	61	(18)	[0]	2349	(1467)	-	-	-	[0]	1111	(334)
-10 ≤ P < -5	[0]	37	(15)	[0]	1288	(888)	-	-	-	[0]	577	(300)
-15 ≤ P < -10	[0]	16	(6)	[0]	325	(234)	-	-	-	[0]	261	(162)
-20 ≤ P < -15	[0]	15	(3)	[0]	633	(567)	-	-	-	[0]	182	(97)
-25 ≤ P < -20	[0]	0	(3)	[0]	210	(193)	-	-	-	[0]	127	(79)
-30 ≤ P < -25	[0]	1	(0)	[0]	228	(219)	-	-	-	[0]	66	(45)
-35 ≤ P < -30	[0]	0	(0)	[0]	123	(113)	-	-	-	[0]	40	(24)
-40 ≤ P < -35	[0]	0	(0)	[0]	140	(137)	-	-	-	[0]	33	(22)
-45 ≤ P < -40	[0]	0	(0)	[0]	70	(77)	-	-	-	[0]	9	(5)
-50 ≤ P < -45	[0]	0	(0)	[0]	113	(109)	-	-	-	[0]	7	(3)
-55 ≤ P < -50	[0]	0	(0)	[0]	49	(48)	-	-	-	[0]	2	(1)
-60 ≤ P < -55	[0]	0	(0)	[0]	28	(28)	-	-	-	[0]	0	(0)
-65 ≤ P < -60	[0]	0	(0)	[0]	17	(17)	-	-	-	[0]	0	(0)
-70 ≤ P < -65	[0]	0	(0)	[0]	17	(17)	-	-	-	[0]	0	(0)
-75 ≤ P < -70	[0]	0	(0)	[0]	10	(10)	-	-	-	[0]	0	(0)
-80 ≤ P < -75	[0]	0	(0)	[0]	4	(4)	-	-	-	[0]	0	(0)
-85 ≤ P < -80	[0]	0	(0)	[0]	1	(1)	-	-	-	[0]	0	(0)
-90 ≤ P < -85	[0]	0	(0)	[0]	3	(3)	-	-	-	[0]	0	(0)
-95 ≤ P < -90	[0]	0	(0)	[0]	1	(1)	-	-	-	[0]	0	(0)
-100 < P < -95	[0]	0	(0)	[0]	0	(0)	-	-	-	[0]	0	(0)
P = -100	-	-	-	[0]	0	(0)	-	-	-	-	-	-
TOTALS	[7713]	7852	(4513)	[7713]	7852	(4512)	[15426]	15704	(9025)	[15426]	15704	(9025)

a SEE FIGURE 3 FOR DEFINITION OF TERMS

b ONE HALF OF LOAD RANGE

c AVERAGE OF PEAK AND VALLEY LOADS

TABLE 2. PEAK/VALLEY COUPLING MATRIX (1 OF 4)

		a. TENSION-DOMINATED WING ROOT SPECTRUM (TD)																						
		55	50	45	40	35	30	25	20	15	10	5	0	-5	-10	-15	-20	-25	-30	-35	-40	-45	-50	
PERCENT OF MAXIMUM PEAK LOAD = VALLEYS = PEAKS	55	100																						
	50	95	100																					
55	50	90	95	100																				
	45	85	90	95	100																			
50	45	80	85	90	95	100																		
	40	75	80	85	90	95	100																	
45	40	70	75	80	85	90	95	100																
	35	65	70	75	80	85	90	95	100															
40	35	60	65	70	75	80	85	90	95	100														
	30	55	60	65	70	75	80	85	90	95	100													
35	30	50	55	60	65	70	75	80	85	90	95	100												
	25	45	50	55	60	65	70	75	80	85	90	95	100											
30	25	40	45	50	55	60	65	70	75	80	85	90	95	100										
	20	35	40	45	50	55	60	65	70	75	80	85	90	95	100									
25	20	30	35	40	45	50	55	60	65	70	75	80	85	90	95	100								
	15	25	30	35	40	45	50	55	60	65	70	75	80	85	90	95	100							
20	15	20	25	30	35	40	45	50	55	60	65	70	75	80	85	90	95	100						
	10	15	20	25	30	35	40	45	50	55	60	65	70	75	80	85	90	95	100					
15	10	15	20	25	30	35	40	45	50	55	60	65	70	75	80	85	90	95	100					
	5	10	15	20	25	30	35	40	45	50	55	60	65	70	75	80	85	90	95	100				
10	5	10	15	20	25	30	35	40	45	50	55	60	65	70	75	80	85	90	95	100				
	0	5	10	15	20	25	30	35	40	45	50	55	60	65	70	75	80	85	90	95	100			
5	0	5	10	15	20	25	30	35	40	45	50	55	60	65	70	75	80	85	90	95	100			
	-5	0	5	10	15	20	25	30	35	40	45	50	55	60	65	70	75	80	85	90	95	100		
0	-5	0	5	10	15	20	25	30	35	40	45	50	55	60	65	70	75	80	85	90	95	100		
	-10	0	5	10	15	20	25	30	35	40	45	50	55	60	65	70	75	80	85	90	95	100		
-5	-10	0	5	10	15	20	25	30	35	40	45	50	55	60	65	70	75	80	85	90	95	100		
	-15	0	5	10	15	20	25	30	35	40	45	50	55	60	65	70	75	80	85	90	95	100		
-10	-15	0	5	10	15	20	25	30	35	40	45	50	55	60	65	70	75	80	85	90	95	100		
	-20	0	5	10	15	20	25	30	35	40	45	50	55	60	65	70	75	80	85	90	95	100		
-15	-20	0	5	10	15	20	25	30	35	40	45	50	55	60	65	70	75	80	85	90	95	100		
	-25	0	5	10	15	20	25	30	35	40	45	50	55	60	65	70	75	80	85	90	95	100		
-20	-25	0	5	10	15	20	25	30	35	40	45	50	55	60	65	70	75	80	85	90	95	100		
	-30	0	5	10	15	20	25	30	35	40	45	50	55	60	65	70	75	80	85	90	95	100		
-25	-30	0	5	10	15	20	25	30	35	40	45	50	55	60	65	70	75	80	85	90	95	100		
	-35	0	5	10	15	20	25	30	35	40	45	50	55	60	65	70	75	80	85	90	95	100		
-30	-35	0	5	10	15	20	25	30	35	40	45	50	55	60	65	70	75	80	85	90	95	100		
	-40	0	5	10	15	20	25	30	35	40	45	50	55	60	65	70	75	80	85	90	95	100		
-35	-40	0	5	10	15	20	25	30	35	40	45	50	55	60	65	70	75	80	85	90	95	100		
	-45	0	5	10	15	20	25	30	35	40	45	50	55	60	65	70	75	80	85	90	95	100		
-40	-45	0	5	10	15	20	25	30	35	40	45	50	55	60	65	70	75	80	85	90	95	100		
	-50	0	5	10	15	20	25	30	35	40	45	50	55	60	65	70	75	80	85	90	95	100		
-45	-50	0	5	10	15	20	25	30	35	40	45	50	55	60	65	70	75	80	85	90	95	100		
	-55	0	5	10	15	20	25	30	35	40	45	50	55	60	65	70	75	80	85	90	95	100		
-50	-55	0	5	10	15	20	25	30	35	40	45	50	55	60	65	70	75	80	85	90	95	100		
	-60	0	5	10	15	20	25	30	35	40	45	50	55	60	65	70	75	80	85	90	95	100		
-55	-60	0	5	10	15	20	25	30	35	40	45	50	55	60	65	70	75	80	85	90	95	100		
	-65	0	5	10	15	20	25	30	35	40	45	50	55	60	65	70	75	80	85	90	95	100		
-60	-65	0	5	10	15	20	25	30	35	40	45	50	55	60	65	70	75	80	85	90	95	100		
	-70	0	5	10	15	20	25	30	35	40	45	50	55	60	65	70	75	80	85	90	95	100		
-65	-70	0	5	10	15	20	25	30	35	40	45	50	55	60	65	70	75	80	85	90	95	100		
	-75	0	5	10	15	20	25	30	35	40	45	50	55	60	65	70	75	80	85	90	95	100		
-70	-75	0	5	10	15	20	25	30	35	40	45	50	55	60	65	70	75	80	85	90	95	100		
	-80	0	5	10	15	20	25	30	35	40	45	50	55	60	65	70	75	80	85	90	95	100		
-75	-80	0	5	10	15	20	25	30	35	40	45	50	55	60	65	70	75	80	85	90	95	100		
	-85	0	5	10	15	20	25	30	35	40	45	50	55	60	65	70	75	80	85	90	95	100		
-80	-85	0	5	10	15	20	25	30	35	40	45	50	55	60	65	70	75	80	85	90	95	100		
	-90	0	5	10	15	20	25	30	35	40	45	50	55	60	65	70	75	80	85	90	95	100		
-85	-90	0	5	10	15	20	25	30	35	40	45	50	55	60	65	70	75	80	85	90	95	100		
	-95	0	5	10	15	20	25	30	35	40	45	50	55	60	65	70	75	80	85	90	95	100		
-90	-95	0	5	10	15	20	25	30	35	40	45	50	55	60	65	70	75	80	85	90	95	100		
	-100	0	5	10	15	20	25	30	35	40	45	50	55	60	65	70	75	80	85	90				

TABLE 2. PEAK/VALLEY COUPLING MATRIX (2 OF 4)

U. RACE / HAKK MODIFIED TENSION-DOMINATED WING ROOT SPECTRUM (TDR)

A VALLEY ASSOCIATED WITH THE PRECEDING PEAK

TABLE 2. PEAK/VALLEY COUPLING MATRIX (3 OF 4)

A VALLEY ASSOCIATED WITH THE PRECEDING PEAK

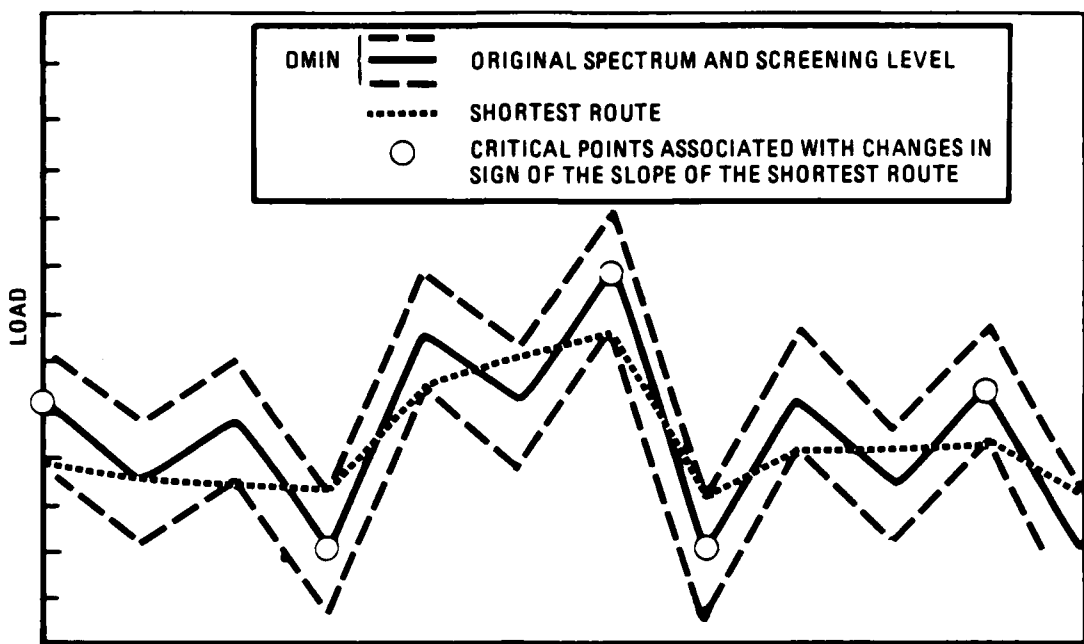
TABLE 2. PEAK/VALLEY COUPLING MATRIX (4 OF 4)

Percent of Maximum Peak Load	Number of Valid Trials
0	0
2	0
4	0
6	0
8	0
10	80
12	75
14	70
16	65
18	60
20	58
22	55
24	52
26	50
28	48
30	45
32	42
34	40
36	38
38	35
40	32
42	30
44	28
46	25
48	22
50	20
52	18
54	15
56	12
58	10
60	8
62	6
64	4
66	2
68	1
70	0
72	0
74	0
76	0
78	0
80	0
82	0
84	0
86	0
88	0
90	0
92	0
94	0
96	0
98	0
100	0

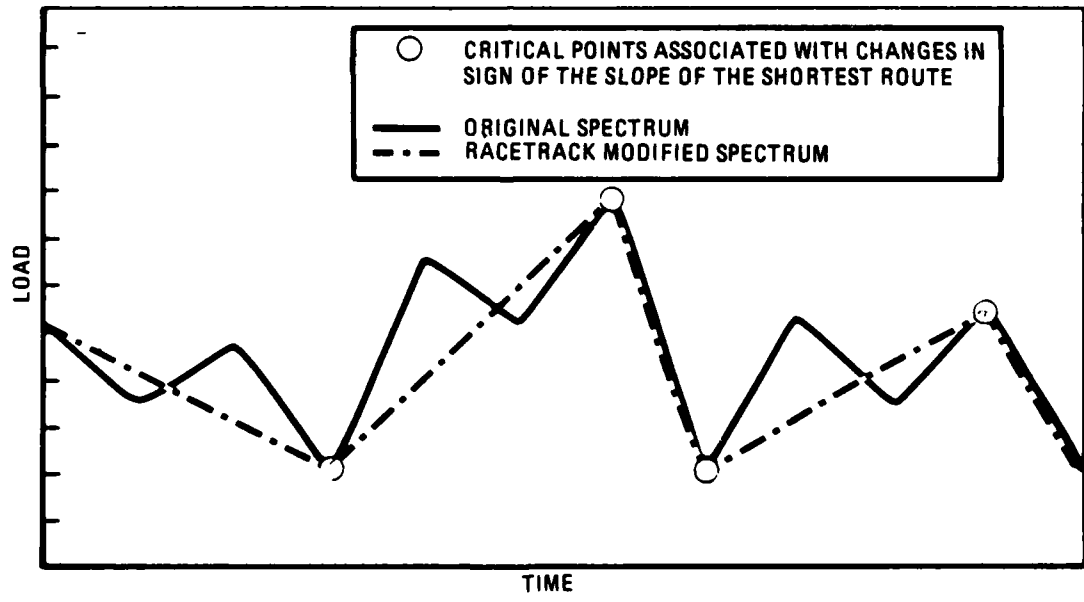
AVAILABILITY ASSOCIATED WITH THE PRECEDING PEAK

2.7.2.1 Racetrack Modification. The technique used to eliminate the small amplitude cycles was the "racetrack" method, which is a screening technique based on the determination of significant load reversals. The technique, shown graphically in Figure 5, utilizes the analogy of a racecourse of a specified width and is represented by the load-time trace of the load spectrum.⁽²⁴⁾ The number of direction changes required to traverse the course using the shortest route depends on the width specified for the course. Significant "corners" are identified as those involving a change in the sign of the slope of the shortest route. These may be thought of as "primary" direction changes. As the course width tends towards zero a change in primary direction is indicated at every load level. As the course width increases towards the other limit, it becomes possible to traverse the course with very few changes in primary direction. This "course width" or "screening level" is given the variable name DMIN and is defined as a fraction of the load used to normalize the spectrum. In the case of the spectrums used in this investigation this normalizing load has been taken to be equal to the value of the maximum tensile spectrum load (σ_{hmax}). Note that the primary load levels are identified and stored in the order that they occur and that there was a significant reduction in applied cycles.

Little information was available to suggest appropriate levels of DMIN, and the selection was complicated by the two competing goals of this modification, one of reducing cycles and the other of determining the importance of low amplitude cycles. The results of applying the racetrack modification with a DMIN of 0.25 on the TD and TC spectrums are shown in Tables 1, 2 (2 of 4), and 2 (4 of 4); and Figure 4. The racetrack modified spectra are designated TDR and TCR, respectively. As shown in Table 1 the numbers of load points are reduced by 44 and 43 percent, respectively (from 9410 load points for the TD spectrum to 5257 load points for the TDR spectrum and from 15704 load points for the TC spectrum to 9025 load points for the TCR spectrum). This reduces the testing time by a like amount and would also reduce spectrum prediction calculation time. The higher magnitude peaks, valleys, and amplitudes are unchanged with a gradual reduction in the number of these features at lower magnitudes and the complete elimination of the lowest magnitude features. Since little was known about the potential effects of this modification, only a single test was performed on each of the seven



a. METHODOLOGY



b. RESULT

FIGURE 5. RACETRACK METHOD OF SPECTRUM MODIFICATION

materials. Additional modifications are planned for future phases of the program, and then duplicate tests or tests with a smaller or larger DMIN can be performed.

2.7.2.2 Truncation of Compression Loads. The effects of tension overloads superimposed on constant-amplitude loading has been extensively evaluated,⁽²⁵⁻³⁴⁾ and it has been well established that the overloads retard fatigue-crack growth. Retardation has also been observed in spectrum loading, usually by comparing the spectrum fatigue behavior of a material tested under a spectrum and the behavior under that same spectrum with the highest loads truncated.⁽³⁵⁾ Some work has been done on the effects of compression loads following overloads superimposed on constant-amplitude loading. The effect of the underload is to reduce the retardation, although the resultant constant-amplitude fatigue-crack growth rates are still lower than without the overload/underload combination.⁽³⁶⁻³⁸⁾

The effects of underload/overload sequencing vary for spectrum fatigue. Hsu and McGee⁽³⁹⁾ added compression underloads to two otherwise all-tension spectra, a bomber and a transport spectrum. These underloads were added before or after high-tension loads. Tests were performed under essentially constant maximum peak stress intensity (K_{hmax} in the present report) conditions by load shedding, and spectrum-crack growth rates were measured. For the transport spectrum, results were obtained at two different levels of K_{hmax} . For the transport spectra at the higher level of K_{hmax} , the result was the same as would be expected from constant amplitude results;⁽³⁶⁻³⁸⁾ that is, a slower spectrum fatigue-crack growth rate for the underload/overload sequence than that for the overload/underload sequence. However, for both spectra at the lower value of K_{hmax} , the opposite was found. Schijve⁽³⁰⁾ reported results similar to these latter results. The high-amplitude gust-load cycles in an otherwise random spectrum were applied in either an underload/overload sequence or in a overload/underload sequence. He found that spectrum life for the underload/overload sequence of gust loads was 85 percent of that for the overload/underload sequence, which corresponds to a slower spectrum fatigue-crack growth rate for the overload/underload sequence, again opposite to the results for similar test with a

constant-amplitude loading baseline. These latter results show that applying results from constant-amplitude fatigue to spectrum fatigue can be misleading.

In the present study both baseline spectrums contain significant compression loads in random spectra. The spectrum with the higher magnitude compression loads (TC) was taken as the baseline and all loads below zero were eliminated from this spectrum by setting all loads less than zero equal to zero. This spectrum is designated TCZ. The number of load points was reduced only slightly as few linked load reversals occurred below zero load (278 load points eliminated from the 15704 load points of the TC spectrum). The summary for this spectrum is shown in Table 1. The TC spectrum contains many compressive load points with magnitudes up to about 95 percent of the maximum peak tensile load. The Phase II results showed that, for a given material and maximum peak stress, the spectrum life for the TCZ spectrum was always longer than the spectrum life for the TC spectrum. It was not clear whether the more damaging effect of the TC spectrum was due to the greater proportion of compressive loads in this spectrum or a difference in the characteristics of the tensile portions of the two spectra. By comparing the fatigue lives for the TC and TCZ spectra, which are identical except for the absence of compressive loads in the latter, the effect of the compressive portion of the complex spectrum on fatigue life can be determined. It is important to separate the effect of compressive loading on spectrum life because different material selection criteria may be needed for aircraft components which experience either a tension-dominated or a tension-compressive load spectrum.

2.7.3 Specimen Preparation

The spectrum fatigue specimens (Figure 6) were machined from the aluminum plates in the L-T orientation. The plates were nominally 8-mm (0.3-in.) thick; however, the plates with mixed microstructures require extensive TMT (32M8 and 32NU, see Section 3). Therefore, the specimens were thinner than the 6.3 mm (0.247 inch) shown in Figure 6; they ran from 4.9 to 5.2 mm (0.193- to 0.205-inch) thick - the maximum thickness after clean up of both surfaces. The specimen surfaces were polished and grids for measuring crack lengths were photographically applied on both sides. The grid spacing was 1.27 mm (0.050 inch). Jeweler's saw cuts, 0.2-mm wide

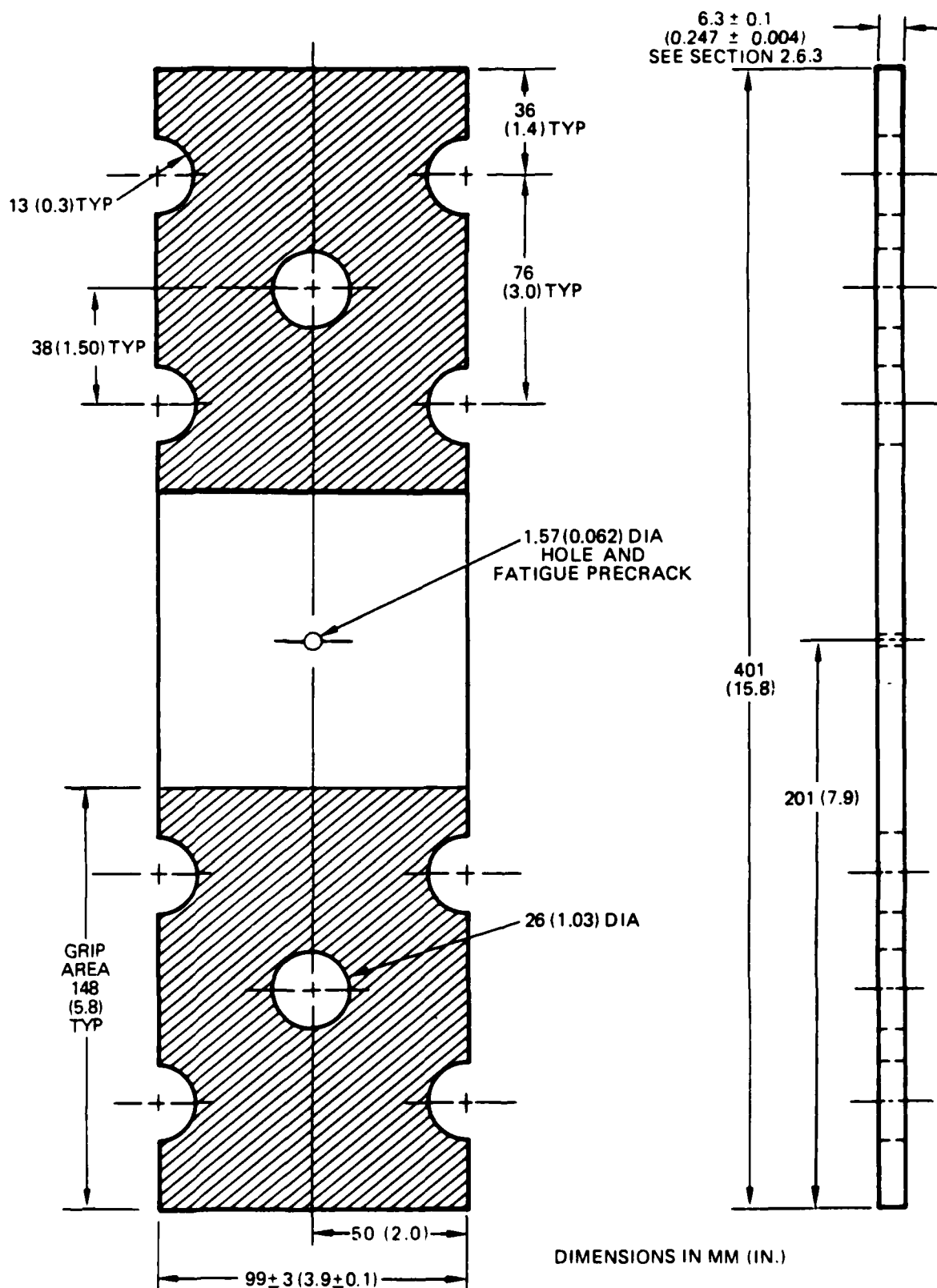


FIGURE 6. SPECTRUM SPECIMEN

and 1-mm deep (0.008-inch wide by 0.04-inch deep), were made at the centrally located hole which provided an adequate "flaw" for precracking the test specimens.

2.7.4 Testing

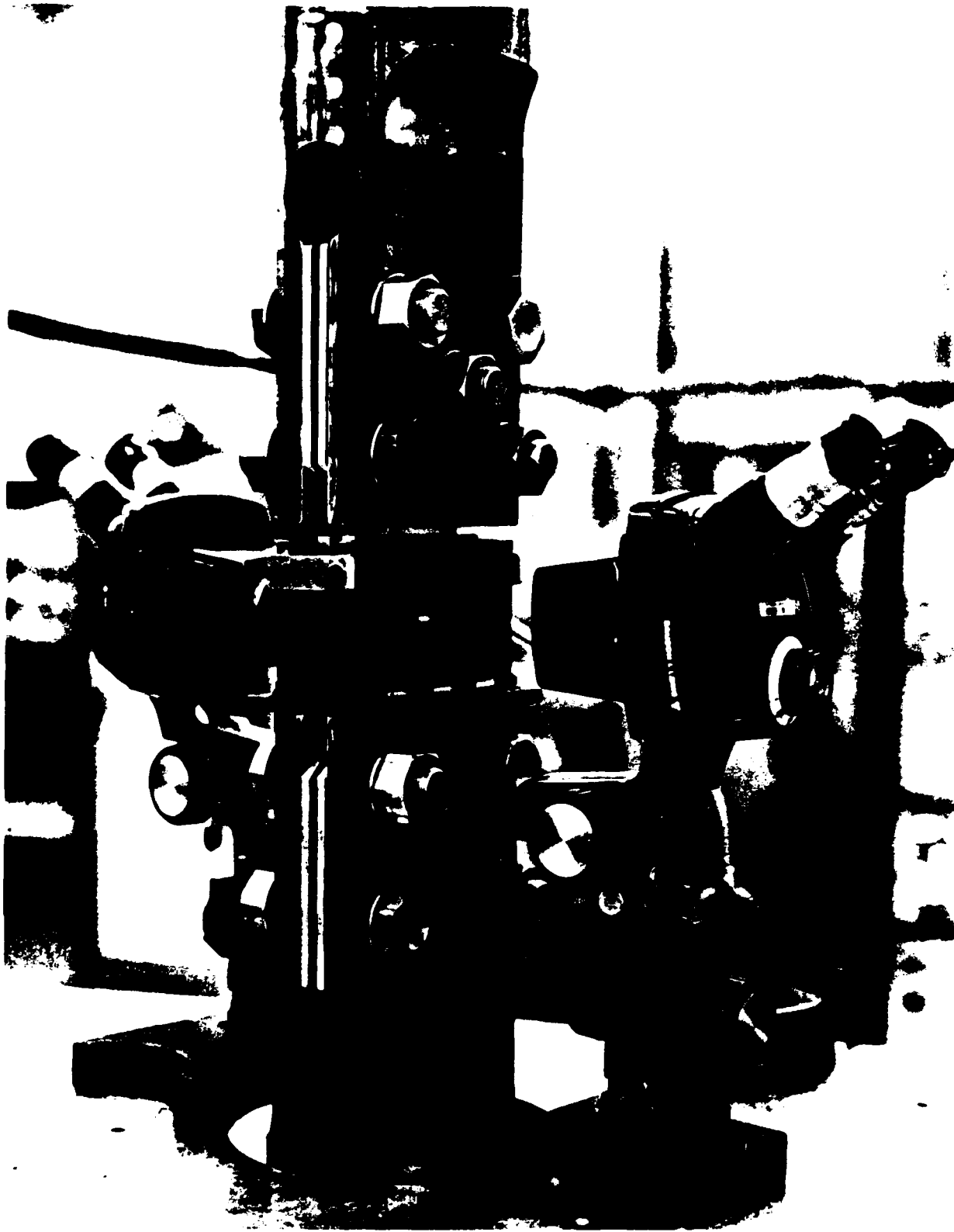
All spectrum tests were performed on a computer-controlled servo-hydraulic machine following the methods of ASTM E647 as appropriate. Pre-cracking was performed under constant amplitude fatigue loading at a stress ratio (R) of 0.1. The maximum stress at the final stages of precracking was approximately half of the subsequent maximum peak spectrum stress (σ_{hmax}). The final precrack length, a , was targeted at 3 mm (0.12 inch). The relative humidity for all spectrum testing was between 40 and 60 percent.

The load history data were stored on a magnetic tape. The stored data contained all the necessary information to control the test, including the desired waveform, frequency, and load points. The test setup is shown in Figure 7. Restraints were used to prevent buckling at high compressive loads.

Spectrum testing was conducted at a maximum peak stress (σ_{hmax}) of 145 MPa (21 ksi), corresponding to the lowest stress level that would meet test needs. The spectrum tests were performed using a sinusoidal waveform. The linear (theoretical) point-to-point load rate (peak to valley or valley to peak) was constant at 220 KN/sec. (50 kip/sec.). The choice of load rates was governed primarily by the test system response. The maximum frequency overrode the loading rate when necessary and ensured that even the very small load excursions were applied to the specimens.

A special feature termed Null Pacing was used to ensure that peak loads were obtained. When the error between command and feedback exceeded about one percent, the computer command rate automatically slowed down so that the peak and valley loads were met and overshoots did not occur.

Crack length measurements were made visually with reference to the photographically printed grid lines at four locations on the specimen (front and rear of specimen, right and left tip of crack). The accuracy of a reading was enhanced by the use of a zoom stereo microscope (7-30X) equipped with a 0.025-mm (0.001-inch) increment reticle.



80-03800-11

FIGURE 7. SPECTRUM TEST SETUP

2.7.5 Test Analysis Procedure

The two-point secant method was used to determine crack growth rate per ASTM E647. To minimize previous loading history effects, data points with crack growth rates greater than the first minimum crack growth rate were not plotted on the crack growth rate curves.

For comparison of the different materials, the lives, simulated flight hours for the crack to grow from an initial crack length, a_i , of 6 mm (0.24 inch) to failure was used. A comparison of the maximum peak stress intensities versus crack length is shown in Figure 8.

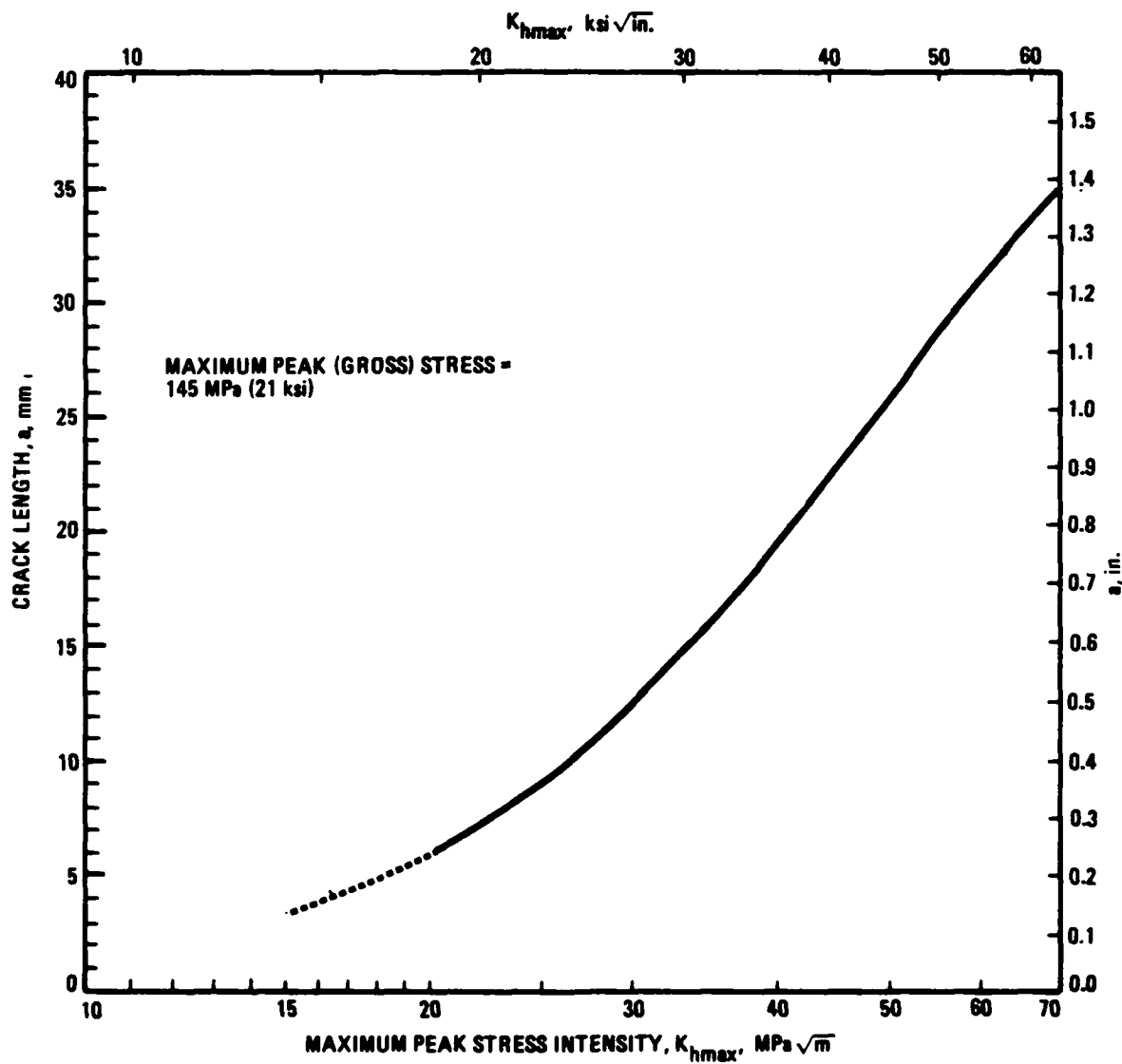


FIGURE 8. COMPARISON OF RANGES OF $K_{h\max}$ VS a

3. RESULTS AND DISCUSSION

The results for the aluminum-lithium alloys with systematically controlled microstructures will be compared to selected results from the evaluation of commercial aluminum alloys in the previous efforts of this program.

3.1 CHEMISTRY AND DENSITY

The chemical compositions and densities of the materials used for this evaluation are presented in Table 3.

TABLE 3. MEASURED COMPOSITIONS AND DENSITIES

ALLOY CODE*	NOMINAL COMPOSITION	SAMPLE NO.	COMPOSITION, WEIGHT PERCENT**						DENSITY	
			Cu	Li	Mg	Zr	Fe	Si	LB/IN. ³	(GM/CM ³)
321CU, 321C8	3Cu-2Li-1Mg	504796	2.8	2.00	0.65	0.11	0.06	0.04	0.0940	(2.60)
32CU	3Cu-2Li	505071	3.0	1.88	—	0.11	0.06	0.04	0.0947	(2.62)
32C8	3Cu-2Li	505199	3.0	1.92	—	0.13	0.06	0.03	0.0946	(2.62)
32MU, 32M8	3Cu-2Li	505310	3.0	1.94	—	0.13	0.06	0.04	0.0945	(2.62)

*FIRST DIGIT – NOMINAL PERCENTAGE OF COPPER
SECOND DIGIT – NOMINAL PERCENTAGE OF LITHIUM
THIRD DIGIT – NOMINAL PERCENTAGE OF MAGNESIUM
FIRST LETTER – GRAIN SIZE: M – MIXED, C – COARSE
LAST CHARACTER – TEMPER: U – UNDERAGED, 8 – PEAK AGED (T851)
**MEASURED BY ATOMIC EMISSION SPECTROSCOPY

3.2 MICROSTRUCTURAL EVALUATION

The microstructures of all six alloys are shown in three-dimensional optical micrographs in Figure 9; these were constructed by photographing the longitudinal, transverse, and rolling planes of each alloy at the center

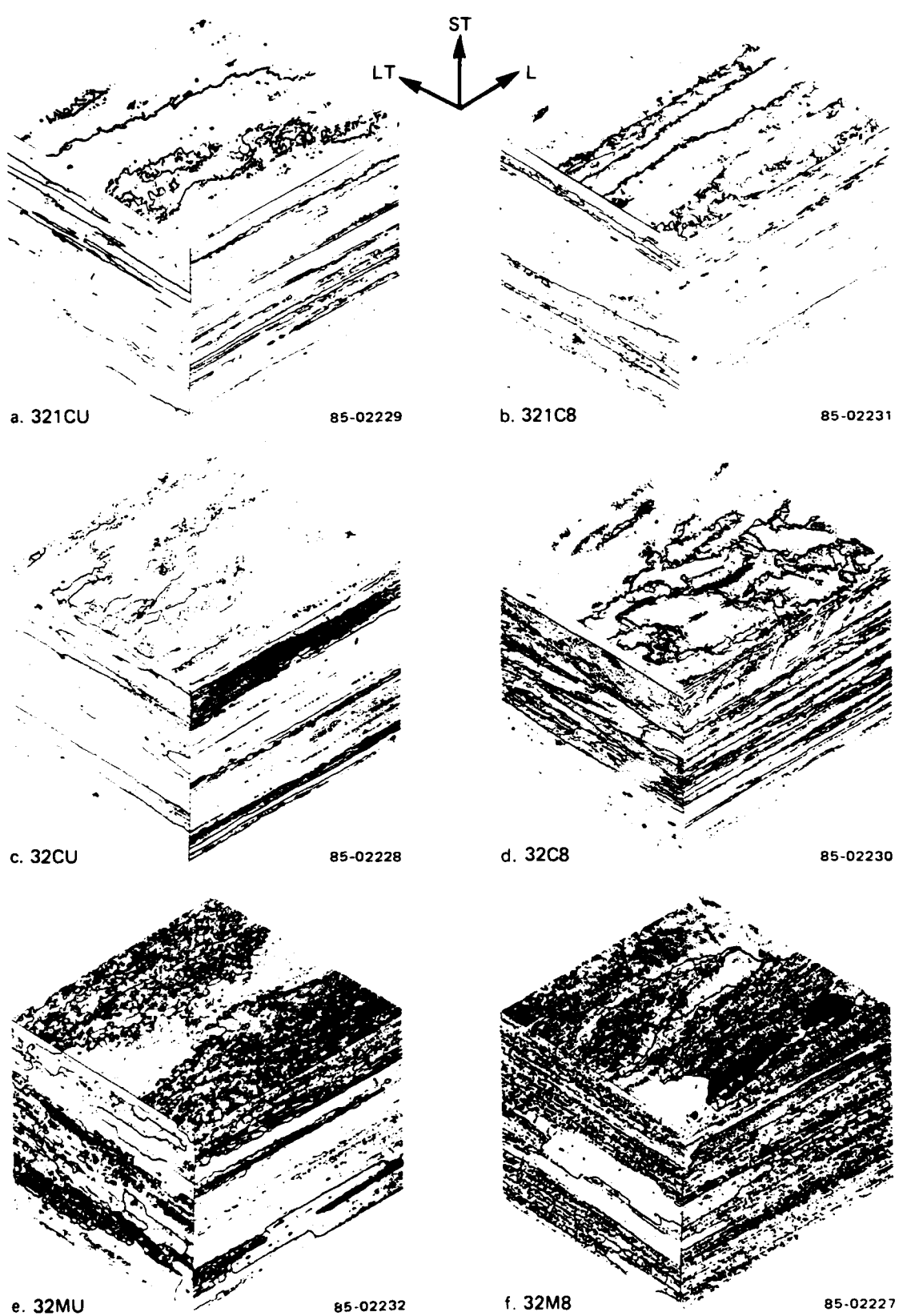


FIGURE 9. MICROSTRUCTURE

(T/2) plane and then assembling the separate views. The grain structures for the four coarse-grained alloys (Figures 9a through 9d) are all basically unrecrystallized. This same type of structure has been seen for similar alloys in a related NAVAIR-funded contract ⁽²⁰⁾ on Al-Li fracture and corrosion behavior. The coarse nature of these structures is a result of the relatively large distances between high-angle grain boundaries (the major boundaries in these micrographs). These high-angle boundary separations can be up to 100 μm in the plate thickness direction. In contrast, the mixed structure alloys (Figures 9e and 9f) are partially recrystallized, with both coarse and fine recrystallized grains along with the unrecrystallized structure.

The crystallographic textures of these alloys were determined by generating X-ray pole figures, using the transmission method. This technique is preferred because it provides important orientation information on the periphery of the pole figure, whereas the reflection method does not provide any peripheral data. The transmission method does not provide information in the center of the pole figure; however, there generally is very little unique texture data for aluminum alloys in this region.

Before discussing the textures of these specific alloys, a slight diversion to describe aluminum alloy textures in general is helpful. The classical retained rolling texture in aluminum alloys is a continuous series of components varying from $(\bar{1}01)[1\bar{2}1]$ through $(123)[63\bar{4}]$ to near $(\bar{1}12)[1\bar{1}1]$, where (hkl) are the indices of a plane parallel to the rolling plane, and $[uvw]$ are the indices of a crystallographic direction parallel to the rolling direction. This series of components is plotted in one quadrant of the (111) pole figure in Figure 10; the numbered points correspond to the six most common texture components. [According to convention, the north pole corresponds to the rolling direction (RD) and the center corresponds to the direction normal to the rolling plane (ND).] Notice that if these points were repeated in all four quadrants, there would be a continuum of intensities starting at the 90-degree and 270-degree locations along the periphery and extending inward on either side of, but not including, the equatorial plane. It is this hollow "tube" of intensities on either side of the equator which denotes the aluminum rolling texture. Complementary texture intensities also appear near

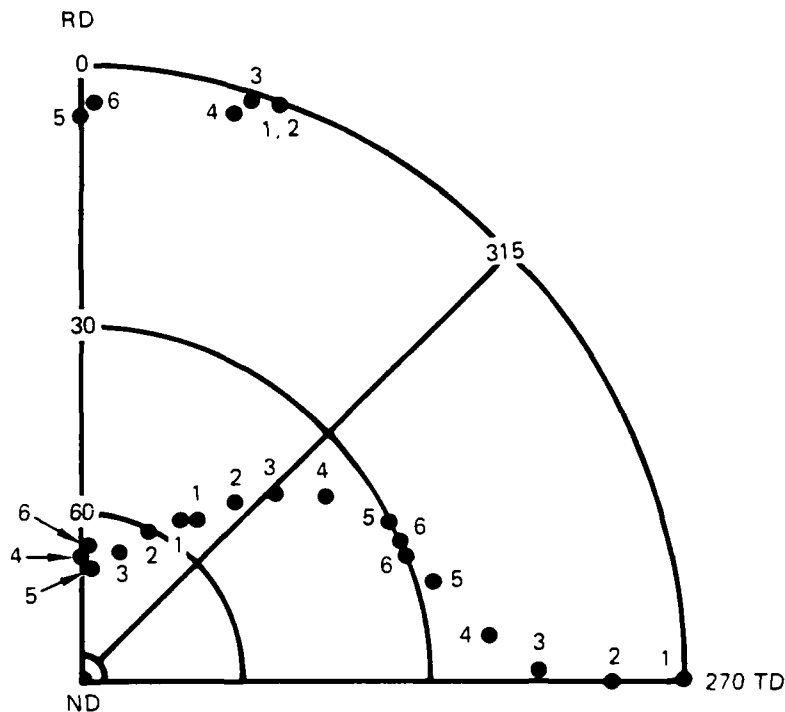
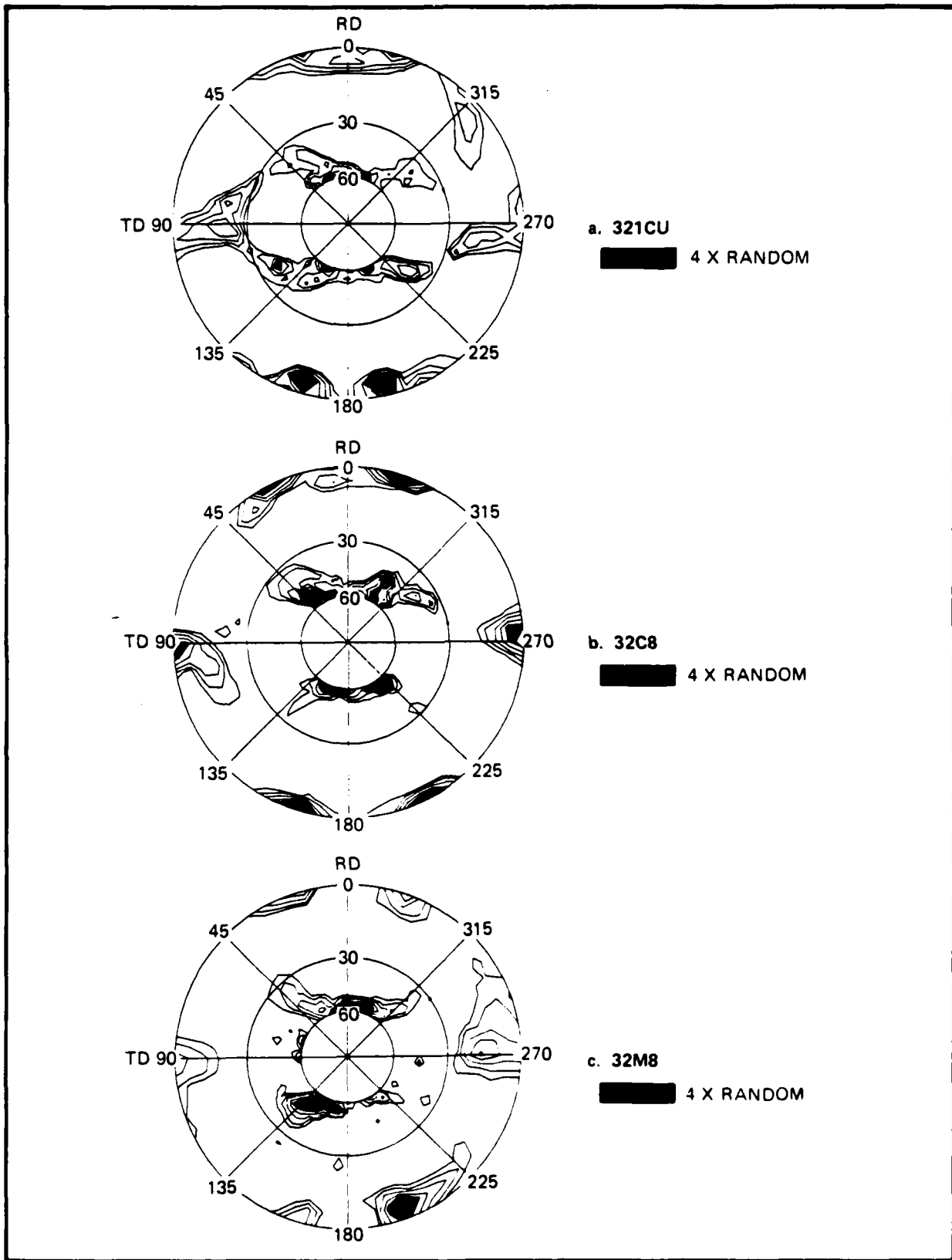


FIGURE 10. LOCATION OF THE SIX ROLLING TEXTURE COMPONENTS IN (111) POLE FIGURE USUALLY FOUND IN ALUMINUM ALLOY, PLOTTED IN ONE QUADRANT

the north and south poles and about 20 to 30 degrees on either side of the poles along the periphery.

The (111) pole figures for the three alloy types (321Cx, 32Cx, 32Mx) are shown in Figure 11; the regions of highest intensity (>4 times random) are shaded to highlight the strongest preferred orientations. Particularly for the 321Cx and 32Cx alloys, the type of preferred orientation basically is characteristic of the retained rolling texture usually found in aluminum alloys, with one exception. In these Al-Li alloys, the equatorial intensity tube is discontinuous near the 30-degree circle, suggesting that one or more of the preferred orientations which make up the tube is weak. These missing components appear to be between $(123)[6\bar{3}4]$ (the so-called "S" component of texture) and $(\bar{1}12)[1\bar{1}1]$ (the "copper" texture); these specific components are labeled 4 and 6, respectively, in Figure 10.

Since the 32Mx structure is partially recrystallized, some textural indication of the so-called "cube" component should be present in the pole figure. This component is denoted by intensity maxima along the four 45-degree lines



**FIGURE 11. (111) POLE FIGURES FOR THE THREE MICROSTRUCTURES
SHOWING INCOMPLETE ROLLING TEXTURES**

where they intersect the 30-degree circle. The pole figure for the 32M8 alloy shown in Figure 11c is asymmetric, but does indicate intensities greater than random for the cube component in the upper left quadrant. This is minimal evidence, at best, to corroborate the metallographic observations. However, the 32Mx duplex structure is rather coarse, and the X-ray technique samples only a small volume of material. It is possible that few recrystallized grains were present in the sampled volume, in which case little or no intensity in the cube orientation locations would appear on the pole figure.

Guinier X-ray analysis was used to determine the amounts of various phases present in each alloy after the two aging treatments. The results are shown in Table 4 as relative amounts of phases detected. Note that these results can be compared only within each type of phase; that is, a "medium" intensity for $\text{Al}_7\text{Cu}_2\text{Fe}$ indicates a greater volume fraction than "small" for the same phase, but does not indicate that there is a greater volume fraction of this phase than of Al_3Li with a "small" intensity. The data basically are consistent with that reported by Vasudevan, et al.⁽²⁰⁾ in a parallel contract investigating similar alloys. Aging from the -U temper to the -8 temper appears to slightly decrease the volume fraction of Al_3Li in the 32 alloys, and has no effect on the presence of the $\text{Al}_7\text{Cu}_2\text{Fe}$ constituent. For the 32Cx and 32Mx alloys, aging increases the fraction of the T_2' - T_2 transition phase, and also increases the amount of T_1 phase in the 32Mx alloys. The equilibrium AlLi phase was detected only in the 32Mx alloys, possibly due to the presence of the high-angle recrystallized grain boundaries which could serve as preferred nucleation sites for this phase. Somewhat surprisingly, the S' phase (Al_2CuMg) was not detected by Guinier analysis in the 321Cx alloys, despite the presence of 0.65 percent magnesium. As will be discussed below, however, clear evidence of this phase is available from transmission microscopy. The TEM studies also shed further light on the presence and nature of the several $\text{Al}_x\text{Cu}_y\text{Li}_z$ precipitates (T-type phases) which occur in this system.

A thorough characterization of the fine structure of these alloys was undertaken, using the transmission electron microscope. Pertinent details of these microstructures will be described below; however, more details on the microstructures of ternary and quaternary Al-Li-Cu(-Mg) alloys can be found in articles by Hardy and Silcock,⁽⁴⁰⁾ Schneider and Heimendahl,⁽⁴¹⁾

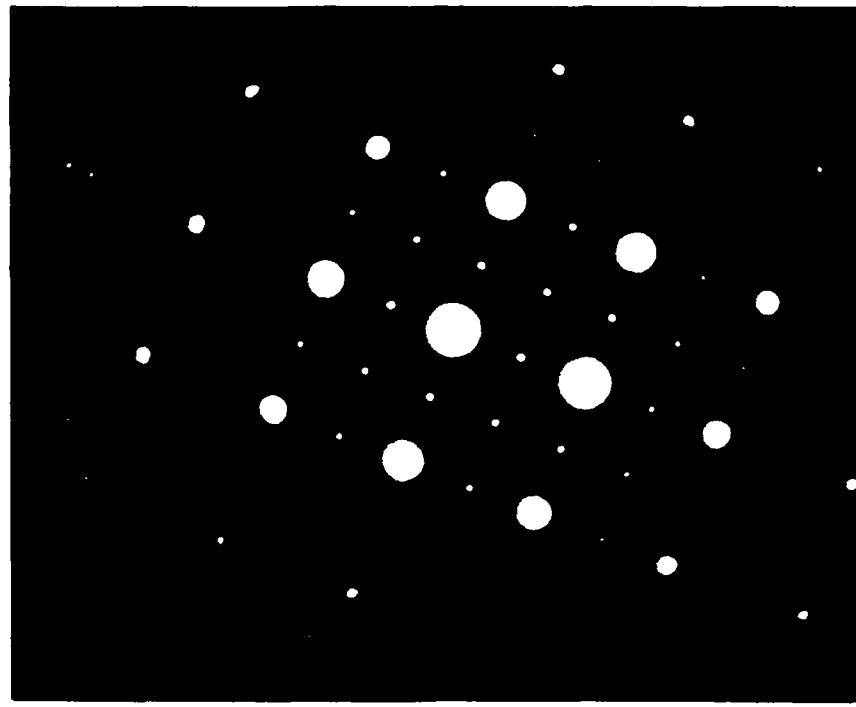
TABLE 4. GUINIER X-RAY RESULTS SHOWING RELATIVE VOLUME FRACTIONS OF PHASES PRESENT

ALLOY	Al_3Li δ'	AlLi δ	Al_2CuLi T_1	" Al_5CuLi_3 " $T_2'-T_2$	Al_2Cu θ	$\text{Al}_7\text{Cu}_2\text{Fe}$
321CU	MEDIUM	-	-	-	-	MEDIUM-
321C8	MEDIUM	-	-	-	TRACE	SMALL+
32CU	MEDIUM	-	-	-	-	MEDIUM-
32C8	MEDIUM-	-	-	V SMALL	-	MEDIUM-
32MU	SMALL+	V SMALL +	SMALL-	V SMALL+	-	SMALL+
32M8	SMALL	SMALL-	SMALL	SMALL-	-	SMALL+

NOTE: RELATIVE VOLUME FRACTIONS ARE RATED SMALL-MEDIUM-LARGE, WITH FINER GRADATIONS INDICATED BY "VERY" AND EITHER A "+" OR "--" SIGN.

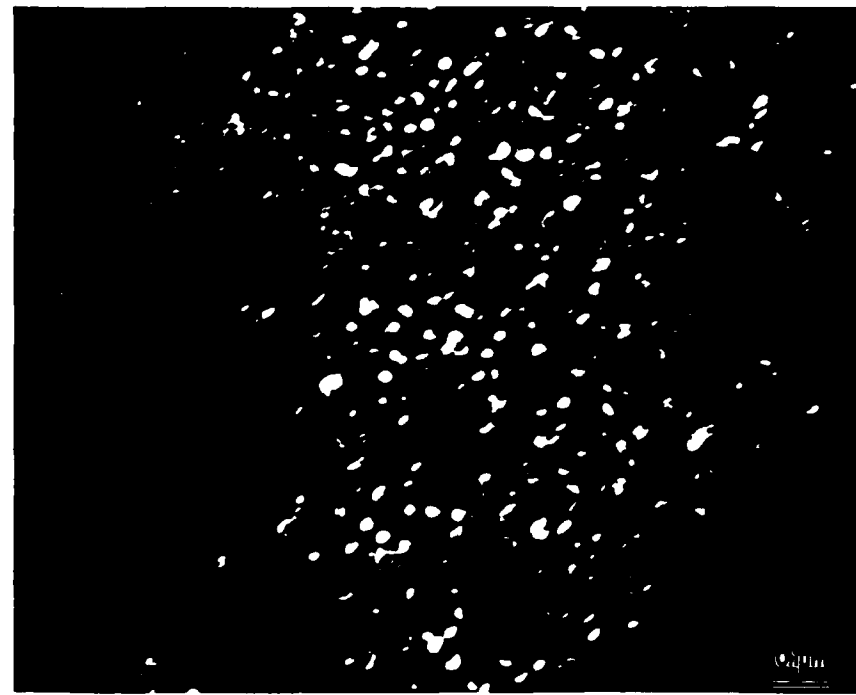
Sanders and co-workers,^(17,18) Starke and co-workers,⁽⁴²⁾ Vasudevan, et al.⁽²⁰⁾ (which describes alloys very similar to these), and Rioja and Ludwiczak⁽⁴³⁾ (a very thorough discussion of the Al-Cu-Li system).

Figure 12a shows a (100) zone axis (ZA) electron diffraction pattern (EDP) for the 321C8 alloy. Strong superlattice reflections at 1/2 (002) and 1/2 (022) positions indicate the presence of Al_3Li (δ'); weaker spots at 1/3 (022) and 2/3 (022) suggest the Al_2CuLi (T_1') phase, which occurs as platelets on [111] habit planes. The faint streaks along all four $\langle 100 \rangle$ directions emanating from the 1/2 (022) positions are characteristic of the Al_2CuMg (S') precipitate, although the low intensity indicates a relatively small volume fraction. Figure 12b is a dark field (DF) micrograph taken using the 1/2 (020) superlattice reflection, and shows a high density of δ' precipitates in the matrix. When the 2/3 (022) reflection is imaged, the T_1' phase can be seen (Figure 12c); the faces of some platelets can be seen because the [111] habit plane is inclined at 54 degrees to the ZA. Some S' precipitates are visible when the faint $\langle 100 \rangle$ streak near 1/2 [022] is imaged, as seen in Figure 12d. Recall that Guinier X-ray analysis did not detect any S' ; apparently the small volume fraction observable in the TEM is below the resolution limit for X-ray analysis.



85-03779-13

a. [100] ZA ELECTRON DIFFRACTION PATTERN SHOWING Al_3Li SUPERLATTICE REFLECTIONS, FAINT T_{1}' SPOTS, AND [100] STREAKING INDICATIVE OF Al_2CuMg



85-03779-12

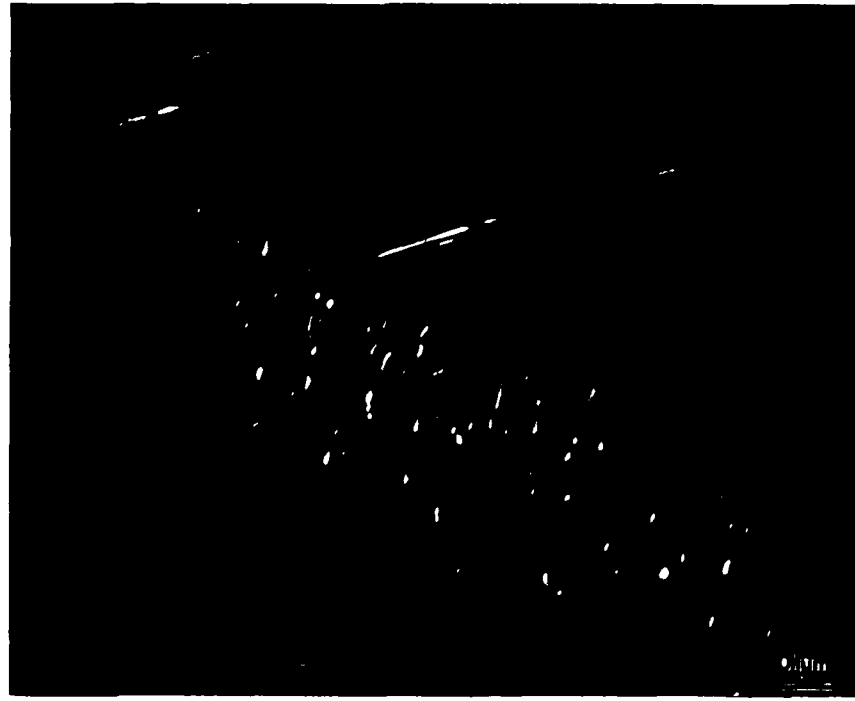
b. DF MICROGRAPH USING 1/2 (002) REFLECTION; [100] ZA.
UNIFORM SPHERICAL Al_3Li ARE VISIBLE

FIGURE 12. ALLOY 321C8



85-03779-11

c. DF MICROGRAPH USING 2/3 (022) REFLECTION; [100] ZA.
SOME T₁ PLATELETS ARE REFLECTING; THESE DO NOT APPEAR ON EDGE SINCE
THE [111] HABIT PLANE IS INCLINED TO THE ZA.



85-03779-10

d. DF MICROGRAPH USING [100] STREAK NEAR 1/2 (022) SPOT; [100] ZA.
SPHERICAL Al₃Li AND Al₂CuMg LATHS ON [012] HABIT PLANES ARE VISIBLE.

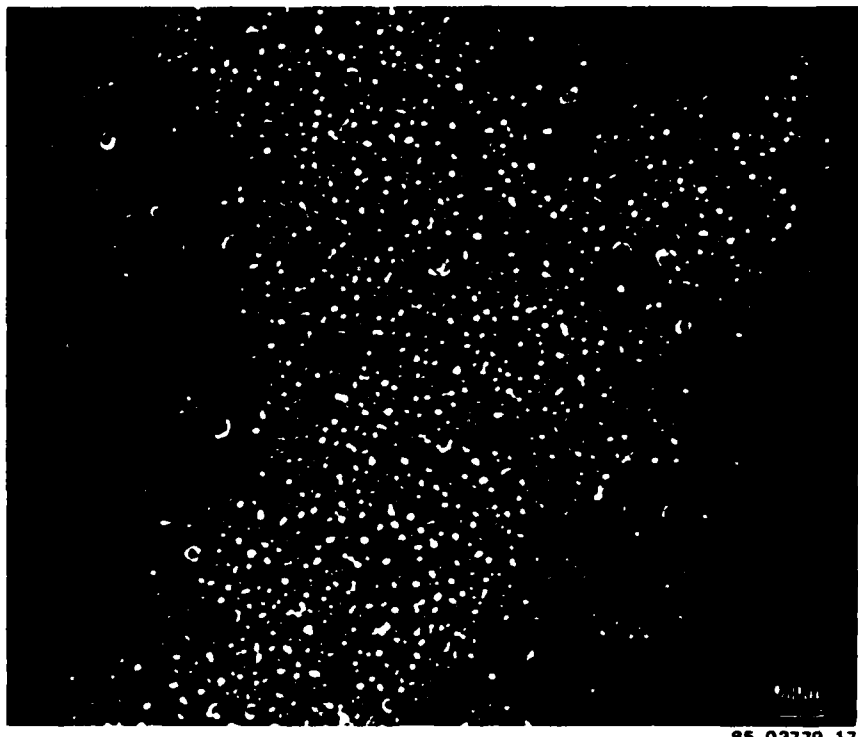
FIGURE 12. ALLOY 321C8 (CONT)

When this same alloy is underaged (321CU), the δ' precipitate radius is smaller (compare Figure 13a with 12b). The BF-DF pair in Figures 13b and 13c shows that no δ' PFZ is present on this low-angle grain boundary; in the T8 temper, only a small PFZ occurs (see below). The same region as in Figure 13b and 13c is shown in Figure 13d using a $\langle 100 \rangle$ streak and shows the somewhat non-uniform distribution of S' in the grain interior as well as precipitation along the grain boundary.

The (100) ZA FDP for the 32CU alloy (Figure 14a) appears very similar to that for the 32Cx alloys, with superlattice reflections, T_1' spots at 1/3 and 2/3 (022), and $\langle 100 \rangle$ streaking. Notice, though, that these $\langle 100 \rangle$ streaks are continuous through both 1/2 (002) and 1/2 (022) positions, unlike the S' streaks which appear around only the 1/2 (022) position. This continuous streaking suggests the presence of a T_2' phase with a [100] habit plane. Rioja and Ludwiczak⁽⁴³⁾ believed that this is the " $T_2'-T_2$ " phase identified by Guinier analysis in Table 4. Because these streaks are continuous through the superlattice reflections, a DF micrograph using the 1/2 (022) reflection (Figure 14b) reveals both spherical δ' and T_2' platelets (two orthogonal variants can be seen). Also, some evidence of δ' encapsulating the Al_3Zr dispersoids can be seen in Figure 14b; this phenomenon has been discussed at great length, most recently by Sanders, et al.,⁽⁴⁴⁾ at the third Al-Li Conference. A BF micrograph (Figure 14c) of a similar area shows the T_1' precipitates on [111] planes, with δ' visible in the background.

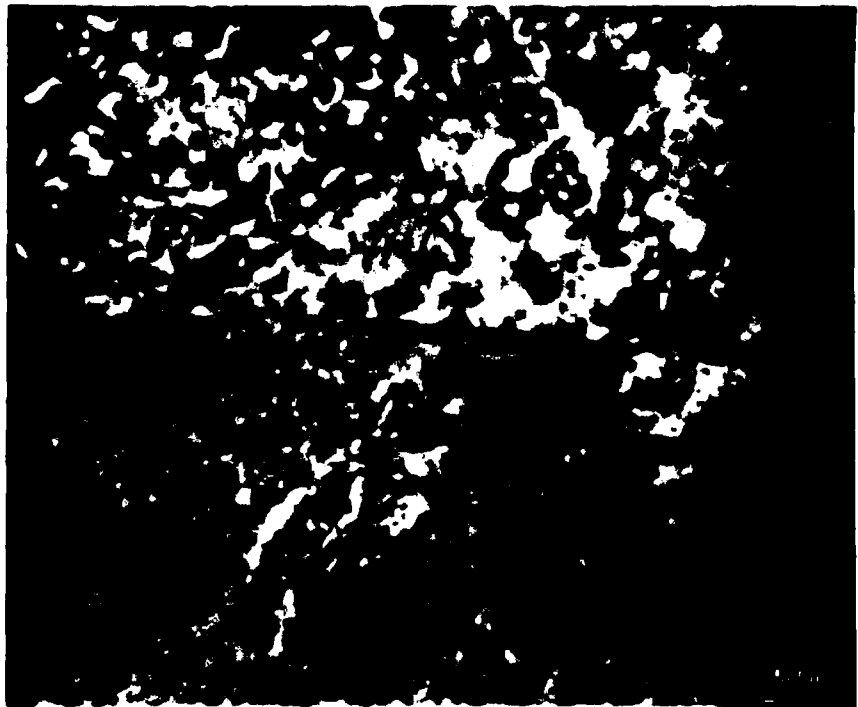
Further aging of the 32C alloy to the T8 condition increases the density of the T-type phases. Figure 15a shows the T_1' precipitates distributed uniformly through the matrix and copiously at the grain boundary. Note, though, that a T_1' PFZ does not occur on low-angle boundaries. A DF micrograph from a superlattice reflection, Figure 15b, shows a decreased volume fraction of δ' , continued encapsulation of Al_3Zr , and thickening of the T_2' phase.

The fine structure of the 32Mx alloys is very similar to that for the 32Cx alloys, as would be expected. The BF-DF pair for 32MU shown in Figures 16a and 16b reveal T_1' , T_2' , and δ' in the BF image, and δ' and T_2' in DF. Though not clearly seen in these micrographs, a small Al_3Li PFZ does occur. The peak-aged alloy (Figure 16c) shows a high density of T_1' precipitates on two [111] variants, one of which is inclined to the [112] ZA.



85-03779-17

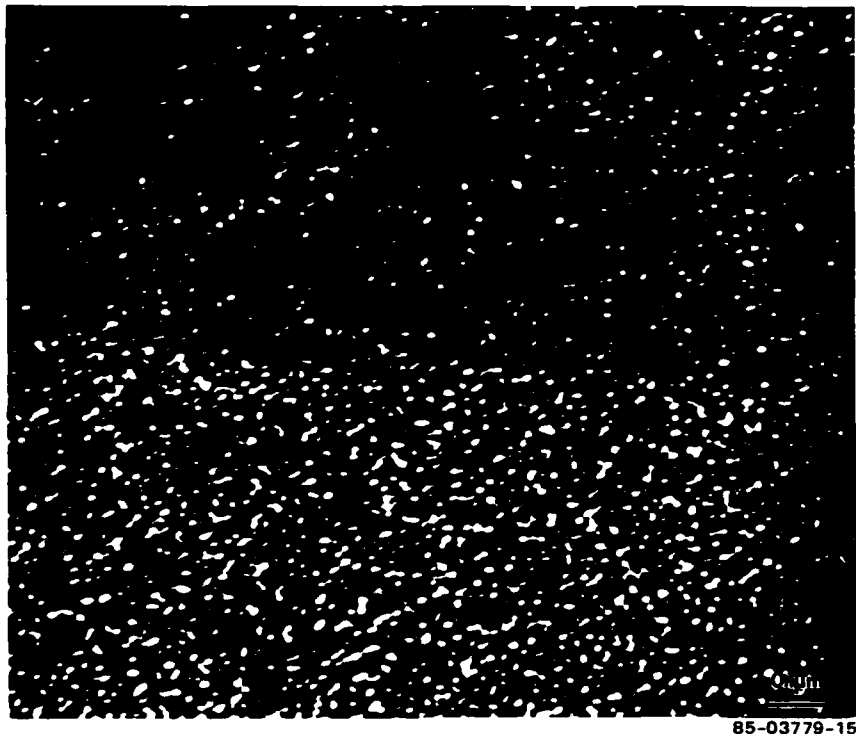
a. DF MICROGRAPH USING 1/2 (002) REFLECTION; [100] ZA
SMALL SPHERICAL Al₃Li ARE UNIFORMLY DISTRIBUTED, ALONG
WITH SOME ENCAPSULATION OF Al₃Zr DISPERSOIDS BY Al₃Li



85-03779-16

b. BF MICROGRAPH SHOWING A SUBGRAIN BOUNDARY AND SOME T₁

FIGURE 13. ALLOY 321CU



85-03779-15

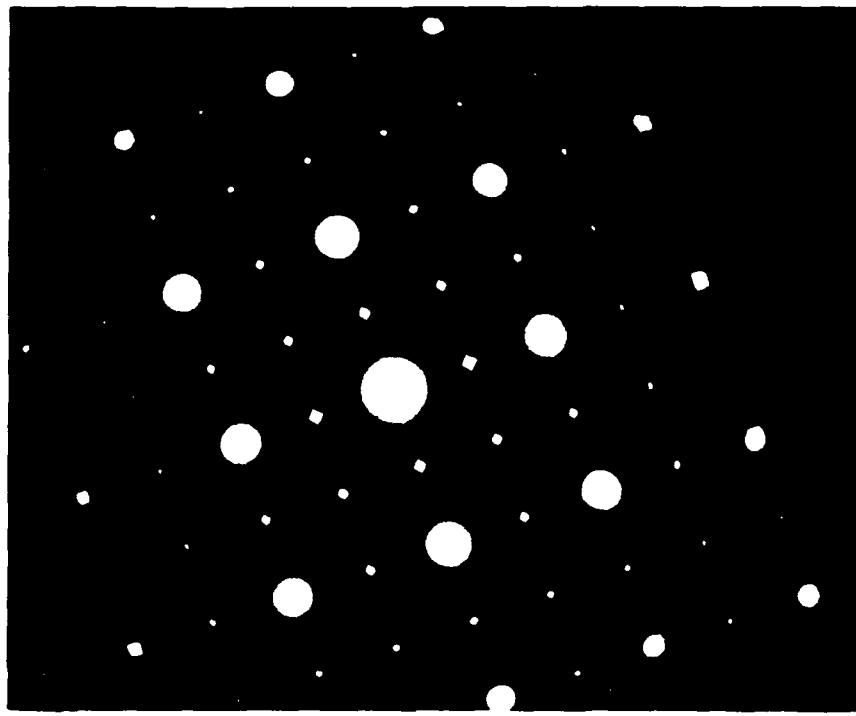
c. DF MICROGRAPH OF b, 1/2 (002) REFLECTION; [100] ZA
COPIOUS Al₃Li PRECIPITATION WITH NO SUBGRAIN BOUNDARY PFZ



85-03779-14

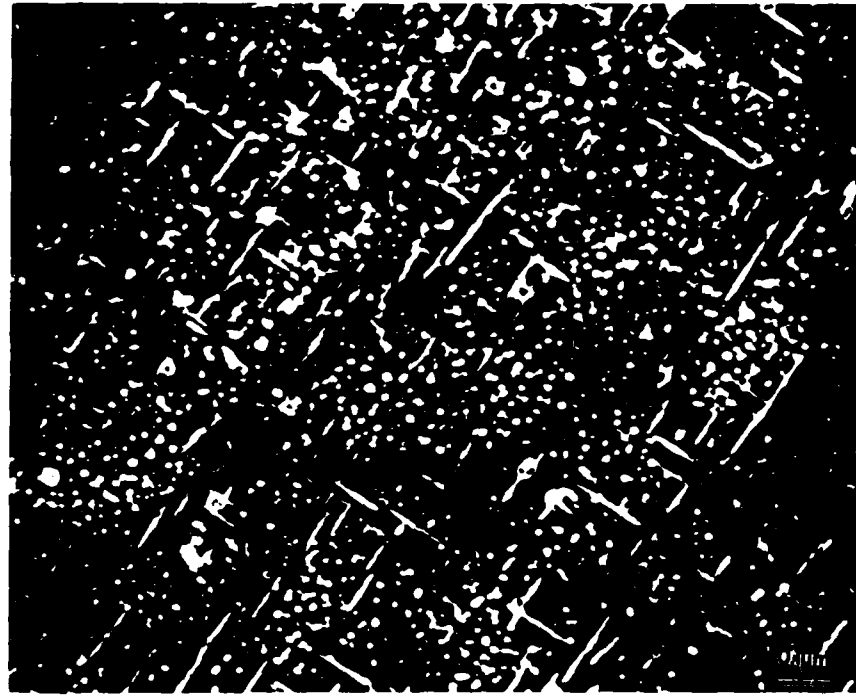
d. DF MICROGRAPH OF b, USING <001> STREAK; [100] ZA.
LOW DENSITY OF S' PLATELETS, INCLUDING SOME ON SUBGRAIN BOUNDARY.

FIGURE 13. ALLOY 321CU (CONT)



85-03779-20

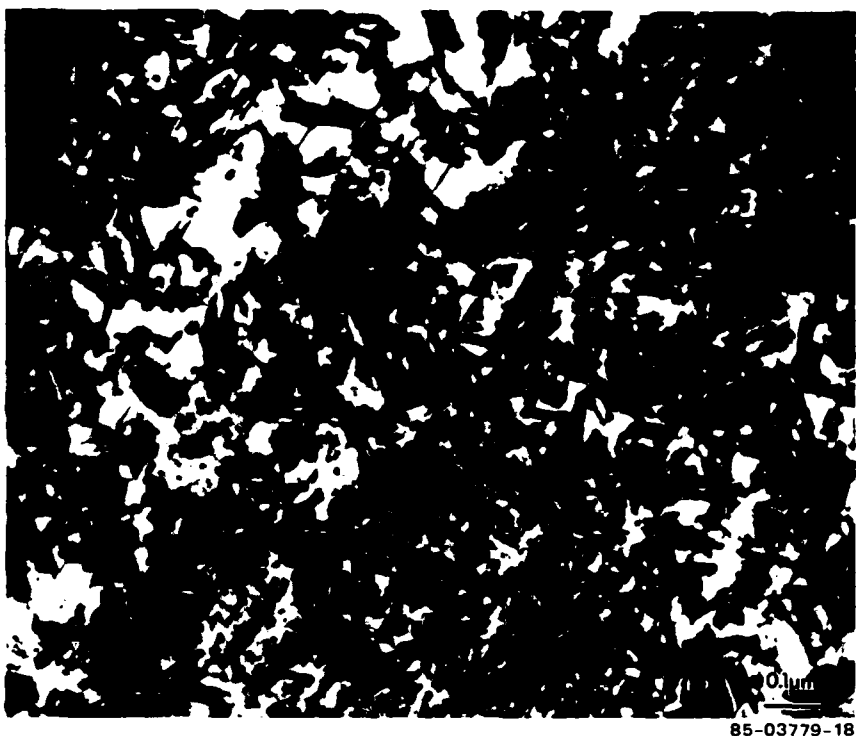
a. [100] ZA ELECTRON DIFFRACTION PATTERNS. Al₃Li SUPERLATTICE REFLECTIONS, T₁' SPOTS, AND [100] STREAKS INDICATING T₂' PRECIPITATES



85-03779-19

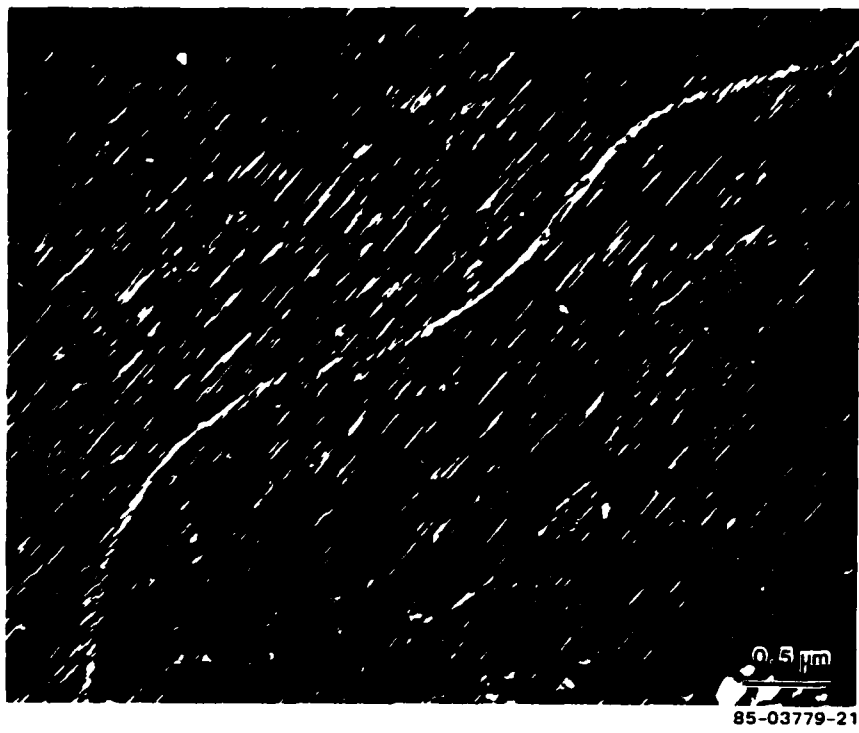
b. DF MICROGRAPH USING 1/2 (022) REFLECTION, [100] ZA. SPHERICAL Al₃Li AND T₂' PLATELETS ON [100] HABIT PLANES ARE VISIBLE

FIGURE 14. ALLOY 32CU

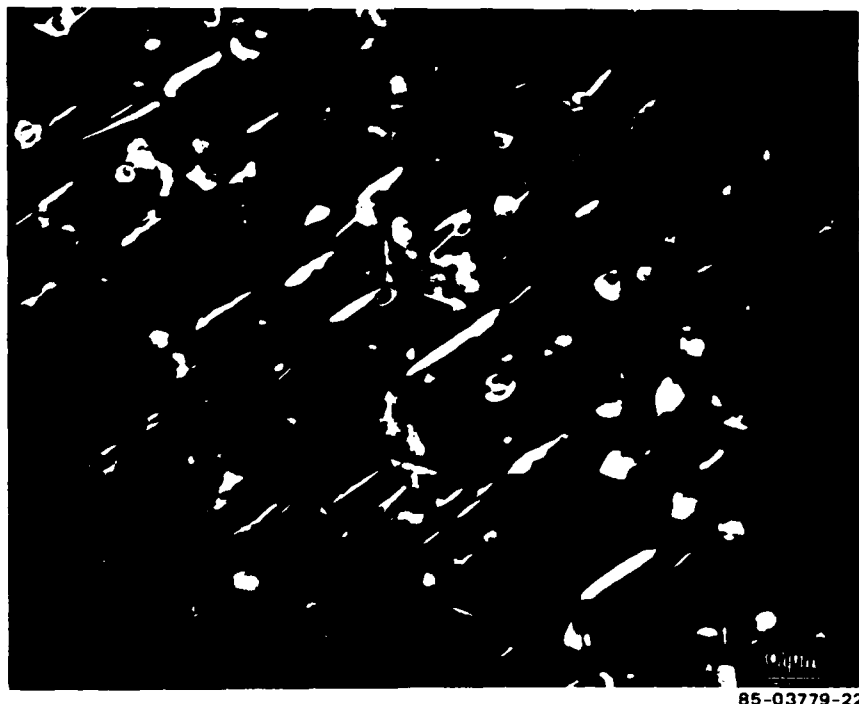


c. BF MICROGRAPH OF b. T₁' PLATELETS CAN BE DISTINGUISHED BY THE FRINGE CONTRAST WHILE SOME T₂' IS VISIBLE AS VERY THIN PLATELETS SEEN ON EDGE

FIGURE 14. ALLOY 32 CU (CONT)

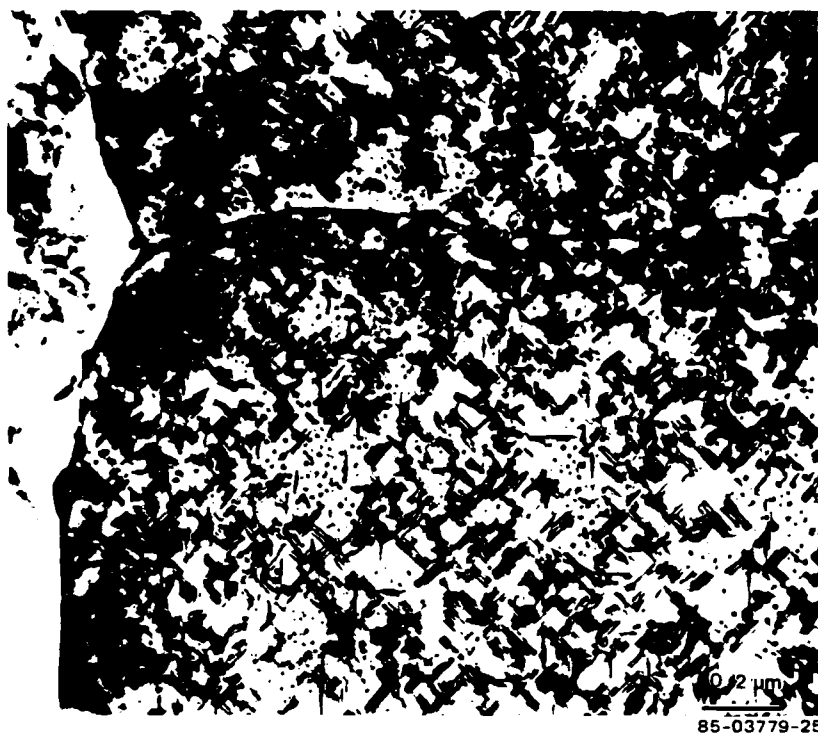


a. DF MICROGRAPH USING 2/3 (022) REFLECTION; [112] ZA. T_1' PRECIPITATES SEEN THROUGHOUT MATRIX AND ALONG SUBGRAIN BOUNDARY.

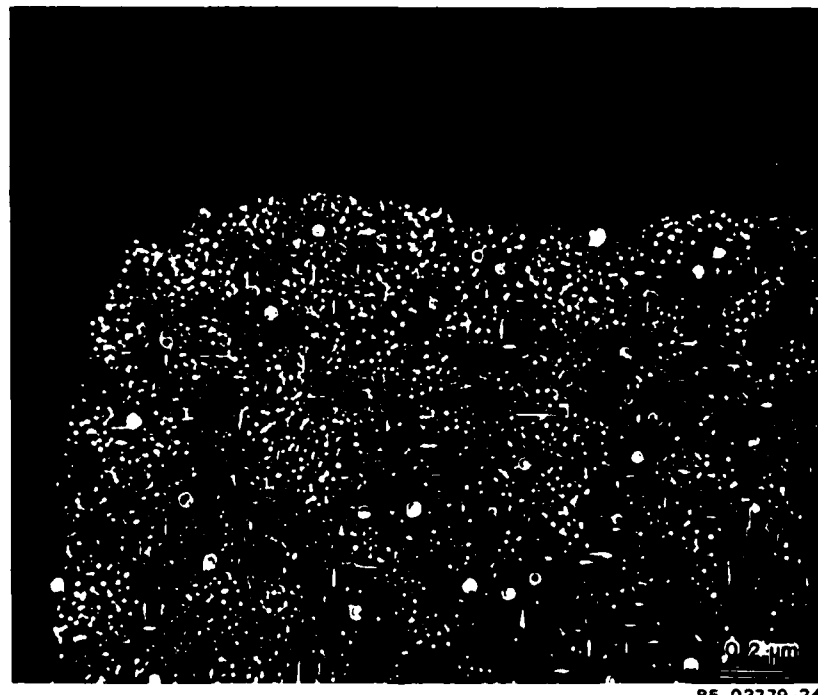


b. DF MICROGRAPH USING 1/2 (022) REFLECTION; [110] ZA. LOW DENSITY OF LARGE Al_3Li IN THIS T8 CONDITION, INCLUDING SOME Al_3Zr ENCAPSULATION. ONE VARIANT OF T_2' ALSO VISIBLE.

FIGURE 15. ALLOY 32C8

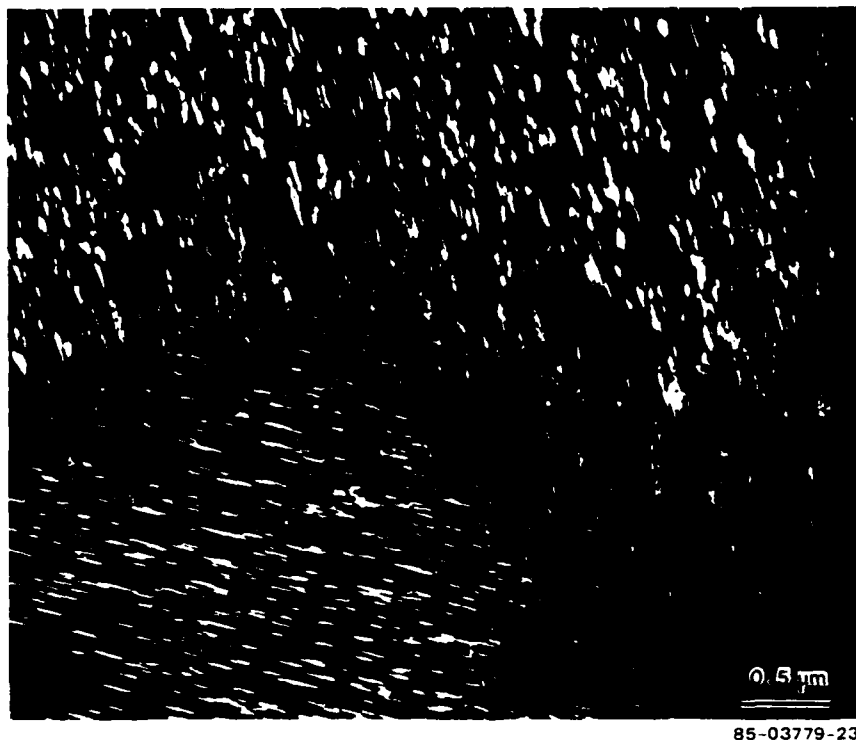


a. BF MICROGRAPH SHOWING δ' , T_1' , AND T_2' PRECIPITATES AND SOME LARGE GRAIN BOUNDARY PHASES IN UNDERAGED CONDITION.



b. ALLOY 32MU DF MICROGRAPH OF a, USING 1/2 (002) REFLECTION; [100] ZA. Al_3Li AND T_2' ARE VISIBLE. A CLOSE COMPARISON OF THIS WITH a INDICATES A SMALL PFZ.

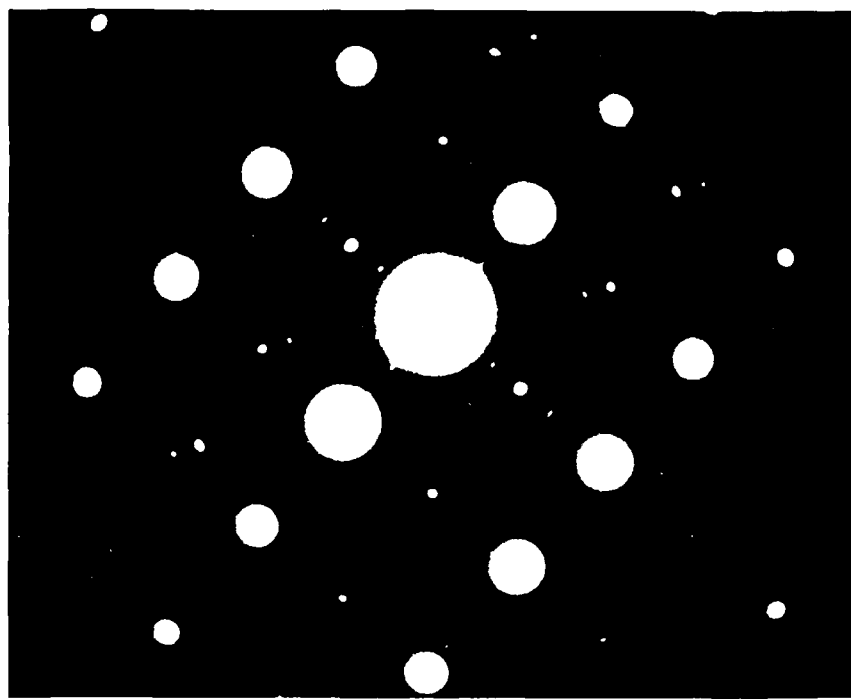
FIGURE 16. ALLOY 32MX



c. DF MICROGRAPH USING 2/3 (131) REFLECTION; [112] ZA. AT LEAST TWO VARIANTS OF T_1' ARE VISIBLE, ONE OF WHICH IS INCLINED TO THE ZA IN PEAK AGED CONDITION.

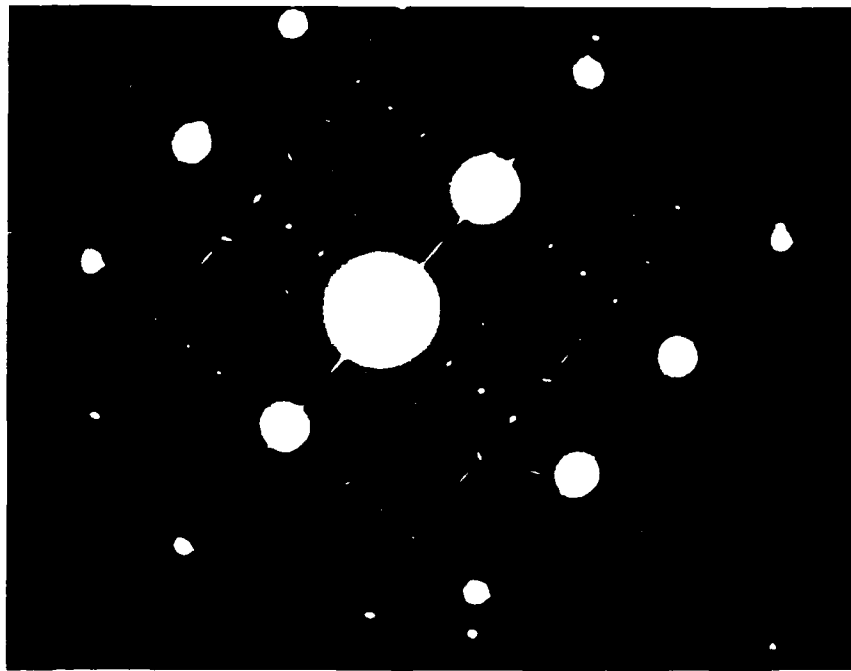
FIGURE 16. ALLOY 32MX (CONT)

Further evidence of the effect of aging on precipitation can be seen from the [112] ZA EDP's in Figure 17. These [112] patterns are especially relevant, since Rioja and Ludwiczak⁽⁴³⁾ have shown that this orientation is necessary to unambiguously identify the metastable T_1' and equilibrium T_1 phases. In the 32MU alloy, Figure 17b, strong superlattice reflections from Al_3Li are seen at 1/2 (022) and 1/2 (024). Weak spots at 1/4 and 3/4 (024) indicate some T_2' , while streaking in <111> directions and intensities at 1/3 and 2/3 (024) suggest the presence of T_1' . Further aging to peak strength (Figure 17b) sharpens the T_1' streaks noticeably, while the superlattice spots lose intensity and the T_2' spots become very difficult to resolve. These changes in intensity imply that aging toward peak strength causes the volume fraction of T_1' to increase at the expense of Al_3Li and, possibly, of T_2' . The Guinier X-ray results in Table 4 similarly show an increase in T_1' at the expense of Al_3Li during aging in the 32Mx alloys and a parallel decrease in Al_3Li in the 32Cx alloys. Notice, though, that a slight increase in T_2' with aging is suggested for the 32Mx alloys. The Al_3Li and T_1' phases are the dominant precipitates in all of these alloys from volume fraction considerations.



85-03779-27

a. UNDERAGED



85-03779-26

b. PEAK AGED

FIGURE 17. ALLOY 32MX – THESE ELECTRON DIFFRACTION PATTERNS SHOW THE EFFECT OF AGING ON PRECIPITATION. RELATIVE TO THE U TEMPER (A), THE T8 TEMPER (B) SHOWS A SHARPENING AND INCREASED INTENSITY OF THE T_1' STREAKS ALONG [111] DIRECTIONS, AND DECREASED INTENSITY FOR BOTH THE Al_3Li SUPERLATTICE SPOTS AND THE T_2' SPOTS AT 1/4 AND 3/4 (024).

however, so it is their relative changes which are most important with regard to mechanical behavior.

The preceding paragraphs have alluded to grain boundary structures in these alloys. Particularly in the C structure materials, which are unrecrystallized, most boundaries seen in the microscope are low-angle; these exhibit no PFZ in the U temper and only a small δ' PFZ at peak strength. Figure 15a especially shows uniform T_1' precipitation throughout the matrix as well as at the grain boundary, but no PFZ. Because the S' phase in the 321 alloys and T_2' in the 32 alloys tend to be inhomogeneously distributed within the matrix, it is difficult to discern any evidence of a grain boundary PFZ for either precipitate. The occasional high-angle boundary will exhibit a small δ' PFZ in the underaged temper and a larger one when peak aged. What is not seen, however, is substantial evidence of equilibrium AlLi precipitation at grain boundaries, which is responsible for PFZ formation in binary alloys.⁽⁴²⁾ Rather, it is the precipitation of the various ternary phases which is primarily responsible for depleting the grain boundary region of Li and causing PFZ formation.

Given this background information on the microstructures of these alloys, it is pertinent to discuss the influence of such structures on deformation and fracture behavior. Innumerable papers have described the tendency of Al-Li alloys to deform via planar slip due the presence of shearable δ' precipitates. This planar slip usually is argued to lead to strain localization, particularly in the unstrengthened PFZ which forms as a result of equilibrium AlLi precipitation on grain boundaries. Low ductility and intergranular fracture are rationalized in terms of failure in the PFZ, primarily as a result of the intense planar deformation causing severe stress concentrations at grain boundary pileups. The article by Starke, et al.⁽⁴²⁾ provides a brief but clear discussion of this subject.

While intense planar deformation is clearly the case in Al-Li binary alloys, it is not necessarily an accurate description of the deformation process in higher-order systems. The δ' PFZ in these alloys is very small, especially in the underaged (U) temper; consequently, there should not be a strong tendency toward strain localization along the grain boundary. Because the ternary precipitates, particularly T_1' , are distributed throughout the matrix and do not form a PFZ, there in fact is some strengthening by these

precipitates in the δ' PFZ. The abundance of T-phase precipitates, especially T_1' , in these alloys certainly mitigates the tendency toward planar slip, since these phases are not easily sheared. Similarly, the presence of S' in the 321Cx alloys also can contribute toward the breaking up of planar slip, thereby reducing the tendency toward low ductility and intergranular fracture usually associated with Al-Li alloys. This is analogous to a solution to the low ductility problem (42) which relies on the introduction of a large volume fraction of incoherent dispersoids to impede the formation of slip bands. Although the T_1' , T_2' , and S' metastable precipitates are only semicoherent, their large total volume fraction can be very effective in reducing the tendency toward planar slip. The observed reduction in δ' volume fraction with aging should further reduce strain localization. In fact, Vasudevan, et al.,⁽⁴⁵⁾ have shown that aging a 3Cu-2Li alloy toward peak strength does indeed reduce the δ' volume fraction (from 7 percent to 0.5 percent), increase the amount of T-phases (from 1 percent to 7 percent), and induce cross-slip. In summary, then we would expect that the T8 temper condition in these ternary and quaternary alloys will be less prone to planar deformation than the underaged temper.

3.3 TENSILE AND FRACTURE TOUGHNESS RESULTS

The mechanical properties determined are listed in Table 5. The relationship between yield strength and fracture toughness is shown in Figure 18. The mixed microstructure material had slightly lower strength and toughness properties compared to the coarser material. The magnesium-containing alloy has higher strength and toughness properties in the longitudinal direction.

3.4 FATIGUE-CRACK GROWTH RESULTS UNDER CONSTANT AMPLITUDE LOADING

Fatigue-crack growth data were generated for all alloys from near-threshold (ΔK_{th}) through intermediate ΔK values, with measured near-threshold FCG rates approaching 10^{-10} m/cycle (4×10^{-9} in/cycle). The FCGR data for the alloys are presented in Figures A-1 through A-6 in Appendix A. In Figure 19, the da/dN versus ΔK curves are shown and compared with 2020-T651 and 7050-T7451. In addition, the FCGR data are shown

TABLE 5. TENSILE AND FRACTURE TOUGHNESS RESULTS

LONGITUDINAL*						
ALLOY CODE	ULTIMATE STRENGTH MPa (KSI)	YIELD STRENGTH MPa (KSI)	EL (%)	K _{IC} **		
				MPa \sqrt{m}	(KSI $\sqrt{IN.}$)	
321CU	498 (72.2)	444 (64.4)	10.3	69.9	(163.6)	
321C8	543 (78.8)	516 (74.9)	5.5	23.7	(21.6)	
32CU	458 (66.4)	411 (59.6)	8.0	49.6	(145.1)	
32C8	500 (72.6)	460 (66.7)	7.8	40.7	(37.0)	
32MU	441 (64.0)	396 (57.4)	8.2	38.2	(34.8)	
32M8	458 (66.4)	418 (60.6)	7.0	21.5	(19.6)	
LONG TRANSVERSE						
ALLOY CODE	ULTIMATE STRENGTH MPa (KSI)	YIELD STRENGTH MPa (KSI)	EL (%)	K _{IC} **		
				MPa \sqrt{m}	(KSI $\sqrt{IN.}$)	
321CU	442 (64.1)	384 (55.7)	5.7	51.1	(46.5)	
321C8	495 (71.8)	465 (67.4)	4.5	24.8	(22.6)	
32CU	430 (62.3)	394 (57.1)	4.0	45.5	(41.4)	
32C8	495 (71.8)	479 (69.5)	2.8	26.5	(24.1)	
32MU	450 (65.3)	403 (58.5)	6.0	30.9	(28.1)	
32M8	470 (68.1)	451 (65.5)	1.2	18.5	(16.8)	

* LONGITUDINAL MODULUS WAS DETERMINED TO BE BETWEEN 11.4 AND 11.5 MSI (≈ 79 GPa) FOR ALL ALLOYS

** CHARPY TOUGHNESS INDICATOR VALUE, NOT A TRUE MEASUREMENT OF K_{IC} PER ASTM E399

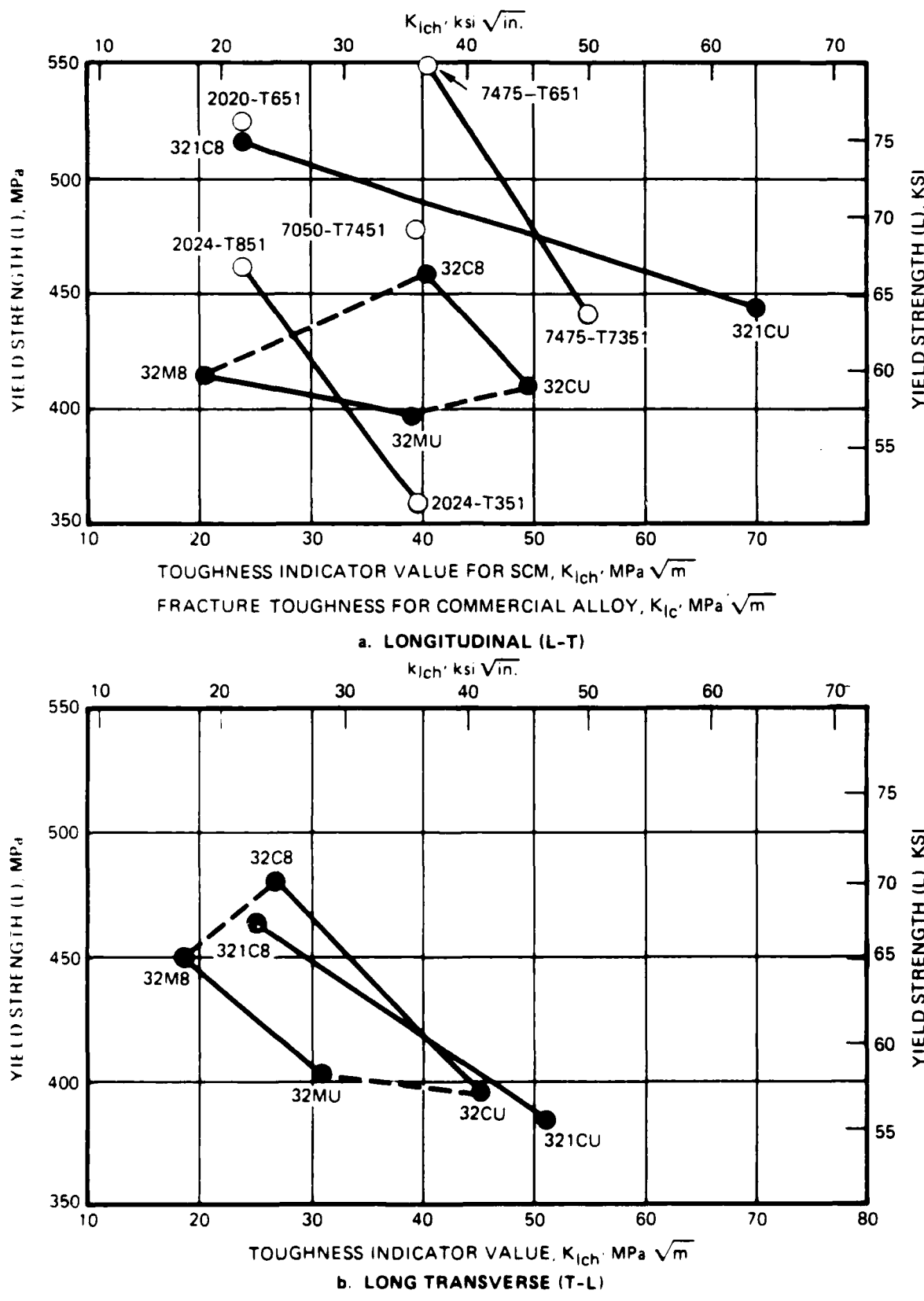


FIGURE 18. YIELD STRENGTH VERSUS FRACTURE TOUGHNESS

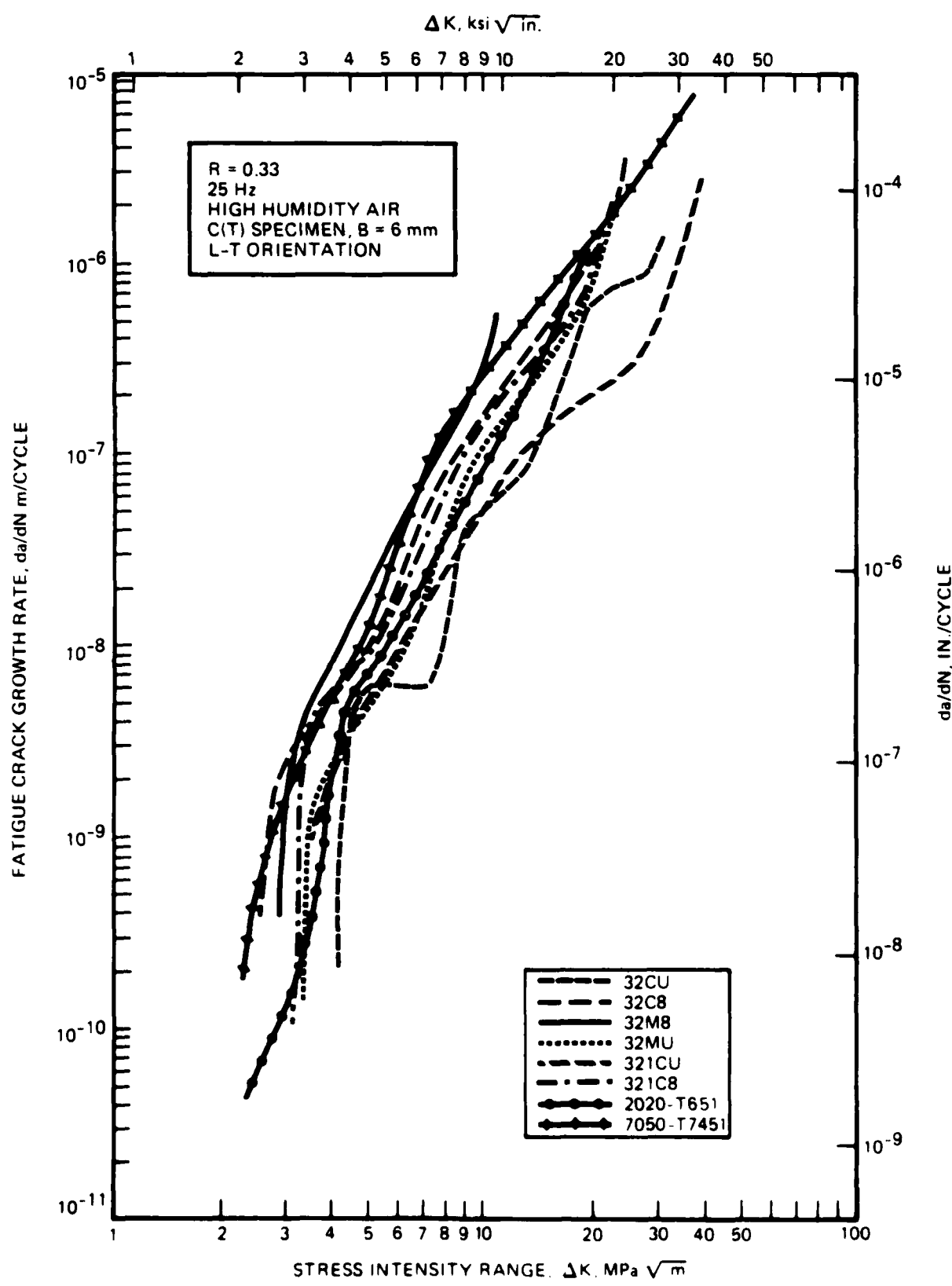


FIGURE 19. CONSTANT LOAD AMPLITUDE FATIGUE CRACK GROWTH RATE DATA

in Figure 20 and Table 6 as the stress intensity required to drive a fatigue crack at a specified rate. In Figure 20 the results are in ascending order of their spectrum fatigue lives (See Subsection 3.5, Figure 24). In general, the applied stress intensity necessary to drive the fatigue crack at a specified rate decreases in the same order as the spectrum fatigue life ranking.

The results in Figures A-1 through A-6 (Appendix A) are plotted in terms of both ΔK_{app} and ΔK_{eff} ; i.e., the applied and effective crack-tip driving forces, respectively. ΔK_{eff} represents the stress intensity range above the point of crack closure, and generally is believed to be that part of the applied ΔK responsible for crack growth.

The FCP data show that, particularly in the near-threshold region below about 10^{-8} m/cycle (4×10^{-7} in/cycle), crack-growth resistance is greater for each underaged alloy than for the corresponding peak aged material. This behavior is expected, based on the increased slip planarity in underaged microstructures. This type of deformation behavior enhances crack branching, which has been shown to exert a powerful influence on FCP behavior⁽²⁰⁾. Suresh,⁽⁴⁶⁾ for example, has demonstrated that branching reduces the stress intensity at the crack tip not only because of crack closure considerations, but also due to the inclination of the crack away from a path normal to the direction of applied stress.

3.5 SPECTRUM TEST RESULTS

The spectrum life results for each test are listed in Table 7 and shown graphically in Figure 21. In Figure 22 the results are shown in the order of their average under the TD and TDR spectrums making comparison of the materials easier. Crack length versus simulated flight hour data (a versus H) are shown graphically in Appendix B, while results for spectrum crack growth rate versus maximum peak stress intensity (da/dH versus K_{hmax}) are shown in Appendix C. For comparison, spectrum crack growth rate curves (da/dH versus K_{hmax}) for all six materials are shown in Figures 23a and 23b for the TD and TC spectrum. For easier comparison of resistance to spectrum crack growth among all ten materials for both spectra, the maximum peak stress intensities to obtain a given crack growth rate are shown in

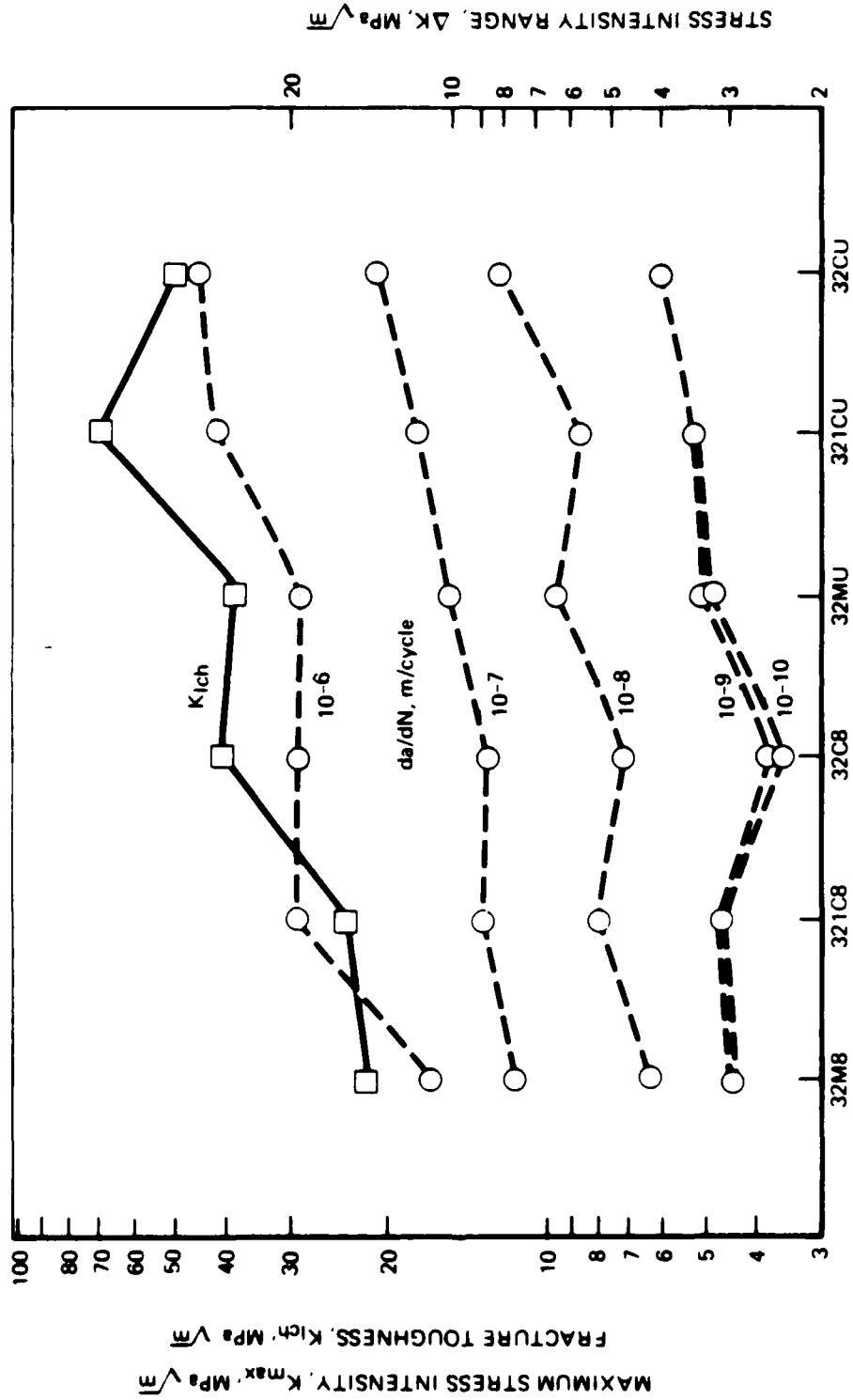


FIGURE 20. STRESS INTENSITY NEEDED TO OBTAIN A GIVEN FATIGUE-CRACK GROWTH RATE UNDER CONSTANT AMPLITUDE LOADING
($R = 0.33$, $> 90\%$ rh, L-T ORIENTATION)

TABLE 6. STRESS INTENSITY RANGE TO OBTAIN A GIVEN FATIGUE-CRACK GROWTH RATE UNDER CONSTANT-AMPLITUDE LOADING

FCGR	$\Delta K, \text{MPa} \sqrt{\text{m}}$ TO OBTAIN A GIVEN FCGR					$K_{I\text{ch}}^a$ ($\text{MPa} \sqrt{\text{m}}$)
	10^{-10} m/CYCLE	10^{-9} m/CYCLE	10^{-8} m/CYCLE	10^{-7} m/CYCLE	10^{-6} m/CYCLE	
ALLOY CODE						
321CU	3.46 ^b	3.49	5.69	11.6	28.0	69.9
321C8	3.10	3.19	5.25	8.79	19.7	23.7
32CU	4.02	4.06	7.97	13.7	30.2	49.6
32C8	2.31	2.47	4.70	8.55	19.2	40.7
32MU	3.21	3.33	6.32	10.1	19.3	38.2
32M8	2.91 ^b	2.96	4.20	7.53	10.9 ^b	21.5

^a CHARPY TOUGHNESS INDICATOR VALUE

^b EXTRAPOLATED

TABLE 7. SPECTRUM FATIGUE RESULTS

MAXIMUM PEAK STRESS, $\sigma_{\text{hmax}} = 145 \text{ MPa}$ (21 ksi)

CRACK GROWTH FROM 6mm (0.24 in.) TO FAILURE

SIMULATED FLIGHT HOURS, H					
SPECTRUM	TD	TDR	TC	TCR	TCZ
ALLOY CODE					
321CU	64.371	81.293	47.802	39.433	104,774
321C8	15.196	12.337	13.347	11.038	14,432
32CU	99.997	95.296	24.527	46.632	109,439
32C8	18.373	22.171	14.376	13.534	20,918
32MU	26.942	34.045	21.621	18.492	41,388
32M8	1.790	1.217	895	840	0*

* LESS THAN 1900 SIMULATED FLIGHT HOURS

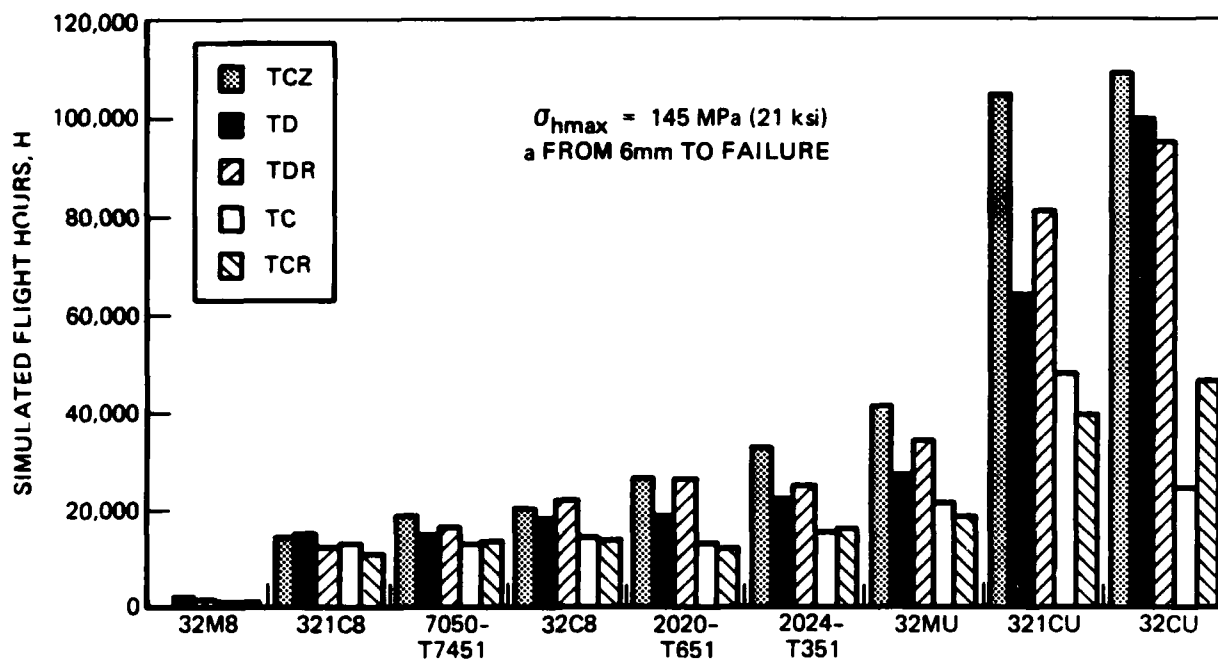


FIGURE 21. SPECTRUM FATIGUE LIVES

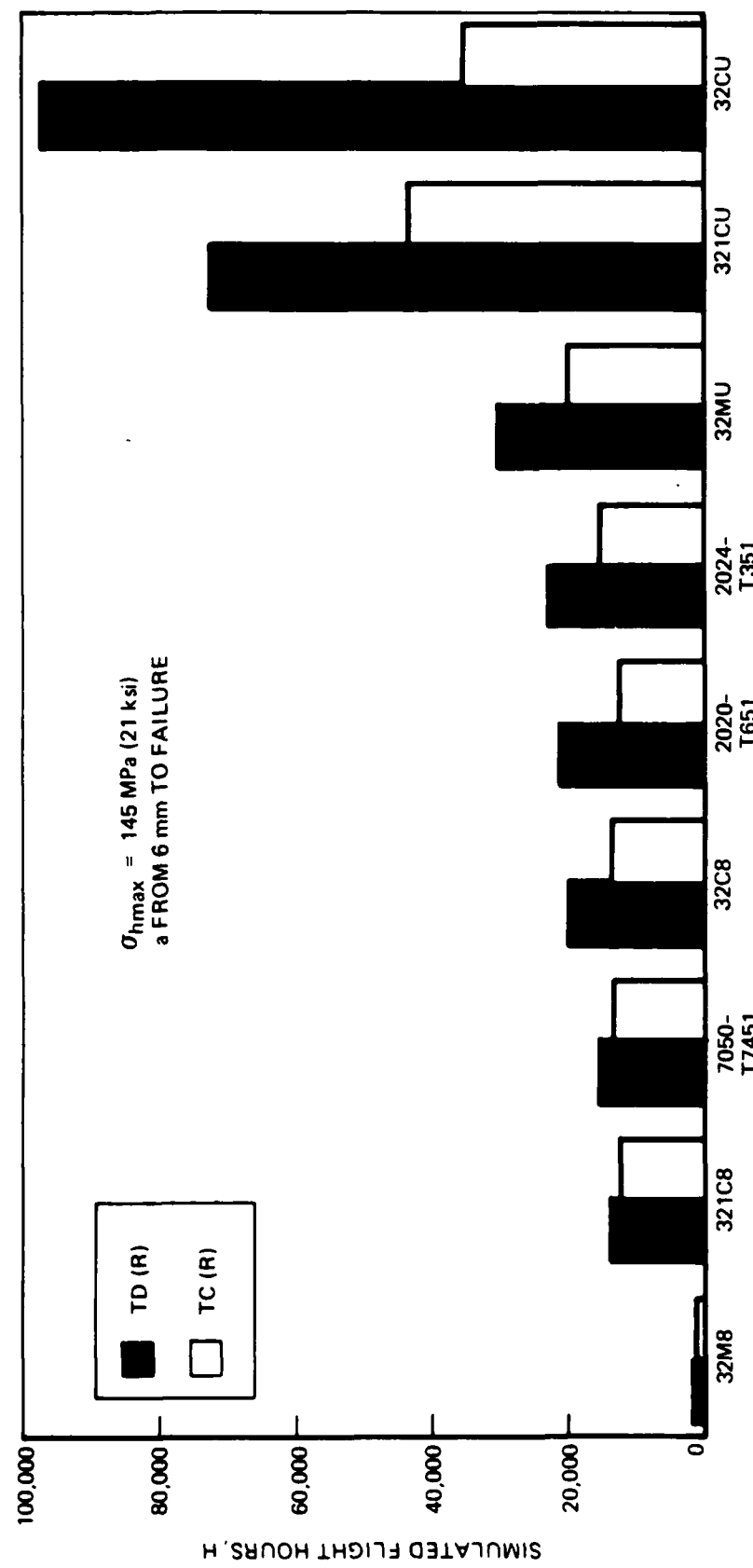
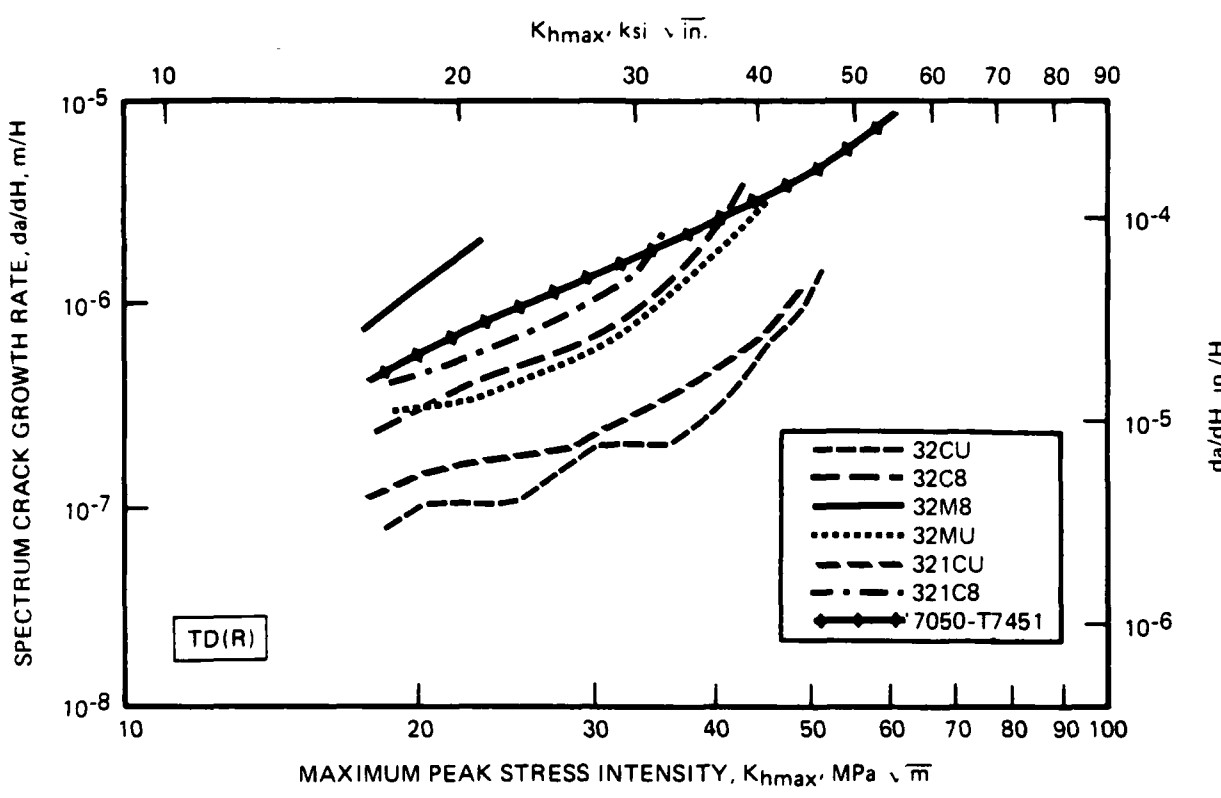
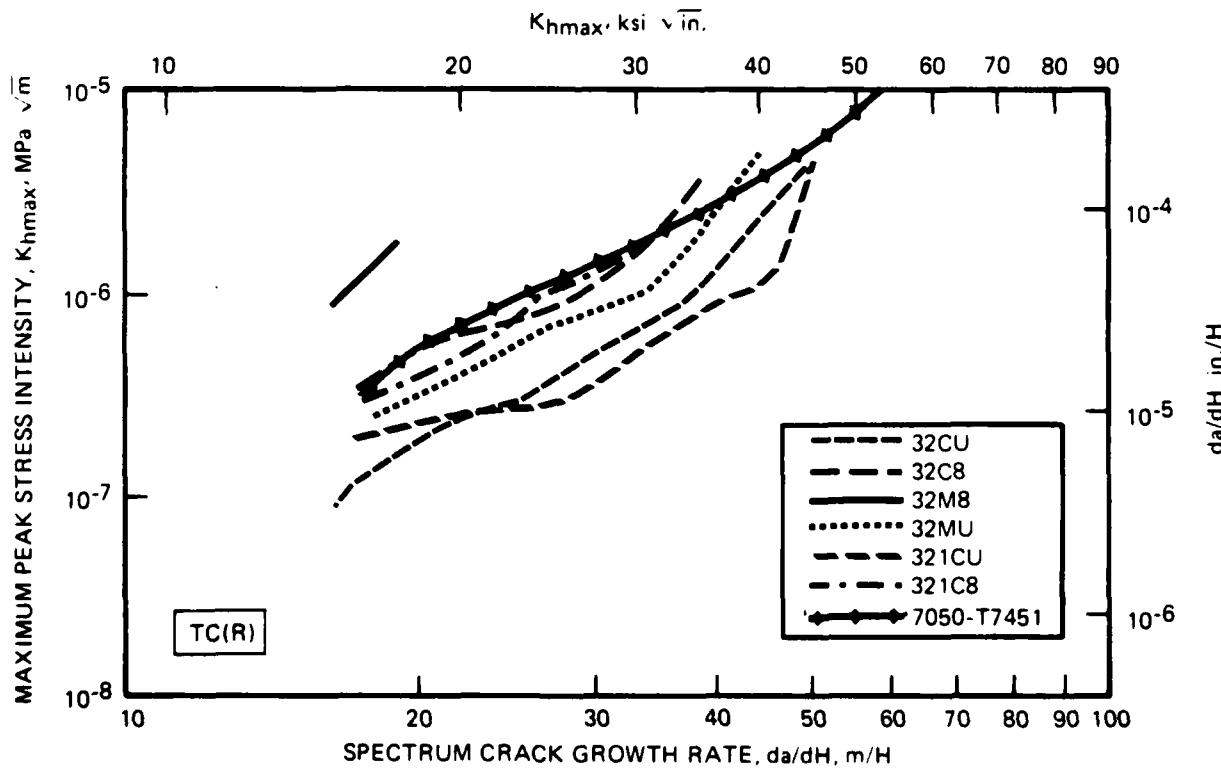


FIGURE 22. SPECTRUM FATIGUE LIVES FOR TD AND TC SPECTRUMS



a. TENSION-DOMINATED SPECTRUMS



b. TENSION-COMPRESSION SPECTRUMS

FIGURE 23. SPECTRUM FCGR CURVES

Figure 24 and Table 8, in presentations similar to those for the constant amplitude data in Figure 20 and Table 6.

3.5.1 Ranking of Materials

In Figure 22, the average of results under the baseline and racetrack spectrum are shown. These averages are designated TD(R) and TC(R). Several observations can be made based on this comparison for crack growth from 6mm to failure:

1. The most significant observation is that the underaged temper resulted in significantly longer spectrum fatigue lives.
2. In the same temper, the coarse-grained alloys have longer lives than the mixed microstructure alloys.
3. The lives for the coarse-grained alloys with and without magnesium are similar for the same temper (321CU versus 32CU and 321C8 versus 32C8) with the magnesium-free alloy generally having longer lives.
4. The three experimental underaged alloys had longer spectrum fatigue lives than the commercial alloys evaluated in this program (represented in the graphs by 2024-T351 and 7050-T7451).

However, the mixed microstructure peak aged alloy (32M8) had shorter lives than any alloy evaluated previously (2024-T851 with lives of about 8,000 flight hours).

3.5.2 Spectrum Crack Growth Behavior

To develop an understanding of the material behavior, more information can be obtained from observations of the behavior as the crack grows, either from crack length versus simulated flight hours or more easily by spectrum FCGR versus maximum peak stress intensity. These data are given in Appendices B and C of this report for the SCM alloys and for the commercial alloys in Appendices B and C of the previous reports.^(1,2) A comparison of these FCGR data for alloys with SCM and for the commercial alloys will show that the alloys with SCM have much more scatter. That is, the change

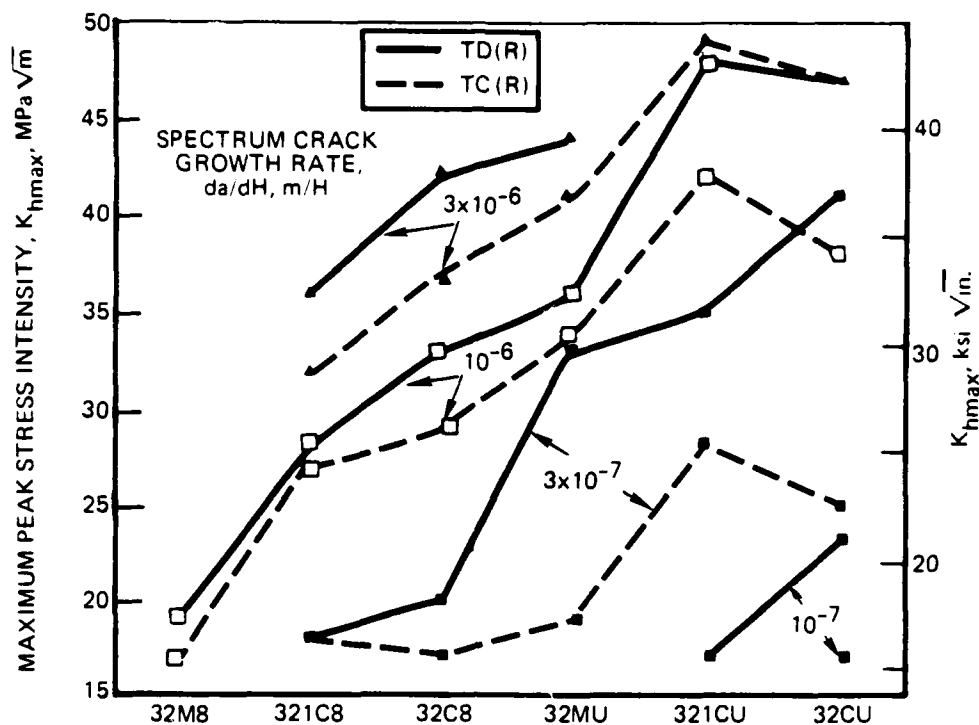


FIGURE 24. MAXIMUM PEAK STRESS INTENSITY NEEDED TO OBTAIN A GIVEN SPECTRUM FCGR

TABLE 8. RANKING OF MATERIALS IN SPECTRUM FATIGUE BY MAXIMUM PEAK STRESS INTENSITY TO OBTAIN A GIVEN FATIGUE CRACK GROWTH RATE

FCGR	K _{hmax} , MPa \sqrt{m}											
	10^{-7} m/H (1.2×10^{-5} in./H)			3×10^{-6} m/H (1.2×10^{-5} in./H)			10^{-6} m/H (4×10^{-5} in./H)			3×10^{-5} m/H (1.2×10^{-4} in./H)		
SPECTRUM	TD(R)	RANK	TC(R)	TD(R)	RANK	TC(R)	TD(R)	RANK	TC(R)	TD(R)	RANK	TC(R)
MATERIAL												
321CU	-	2	17	35	2	28	48	1	42	-	1	49
321C8	-	-	-	18	5	18	28	5	17	36	5	32
32CU	23	1	17	41	1	25	47	2	38	-	2	47
32C8	-	-	-	20	4	17	33	4	29	42	4	37
32MU	-	-	-	33	3	19	36	3	34	44	3	41
32M8	-	-	-	-	6	-	19	6	17	-	6	-

of spectrum FCGR with increasing stress intensity was much less consistent. In general, the scatter was greater for the underaged alloys than for the peak aged alloys. (To obtain the data for Figure 23 and Table 8, the data

had to be replotted using additional data smoothing.) Possible reasons for this scatter will be discussed in Subsection 3.6, Fractographic Analysis.

3.5.3 Effects of Load History

As for the commercial alloys, the lives under the tension-dominated spectrums (TD and TDR) were longer than for the tension-compression spectrums (TC and TCR). However, the lives under TCZ spectrum were not always longer than for the TD spectrum as they were for the eight commercial alloys evaluated - the exceptions being for the 321C8 and 32M8 alloys.

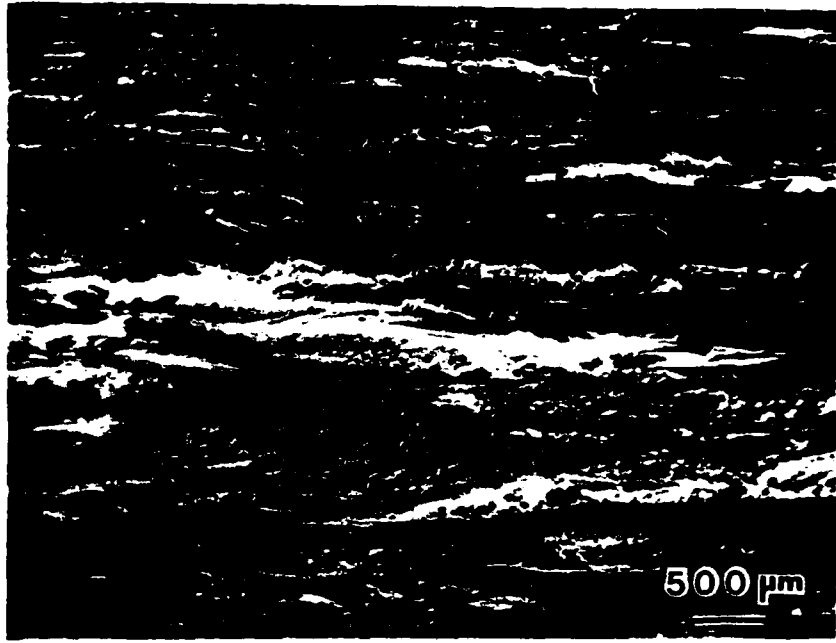
3.6 FRACTOGRAPHIC ANALYSIS OF SPECTRUM FATIGUE SPECIMENS

3.6.1 Macroscopic Appearance

The fracture surfaces of all six alloy/temper/structure combinations were especially rough and coarse. This was true for both the constant-amplitude and spectrum fatigue specimens, though detailed fractographic work was done only on the latter specimens. This roughness corresponds with the generally high crack-closure levels measured during constant amplitude tests, and is expected to contribute towards improved FCP resistance for all types of loading. In some cases, a large amount of dark fretting debris covered parts of the fractures, indicating substantial fracture surface rubbing during the fatigue test. This was especially true for specimens tested with the TC spectrum.

A significant difference in fracture surface roughness was evident between underaged and peak-aged specimens for each structure. Figure 25 shows the fracture surface of 32C8 (TD spectrum) at low magnification ($\times 20$); this surface is relatively coarse, especially at longer crack lengths. There is a substantial amount of "delamination" on planes parallel to the plane defined by the crack-growth direction and the loading axis (parallel to the plate surface) and substantial changes in height both laterally and longitudinally on the surface. Figure 26 shows, however, that the fracture surface for the underaged 32CU specimen is even more tortuous and contains extreme elevation differences. Notice that the fracture surface predominantly consists of planar faces at various angles to one another. These planar faces will be discussed in more detail later, but it is sufficient to point out at this

CRACK GROWTH DIRECTION



X 20

85-03778-29

a. $a = 6.4 \text{ mm (0.25 IN.)}$



X 20

85-03778-28

b. $a = 19.1 \text{ mm (0.25 IN.)}$

FIGURE 25. FRACTURE SURFACE OF ALLOY 32C8, TD SPECTRUM, SHOWING RELATIVELY COARSE SURFACE TOPOGRAPHY

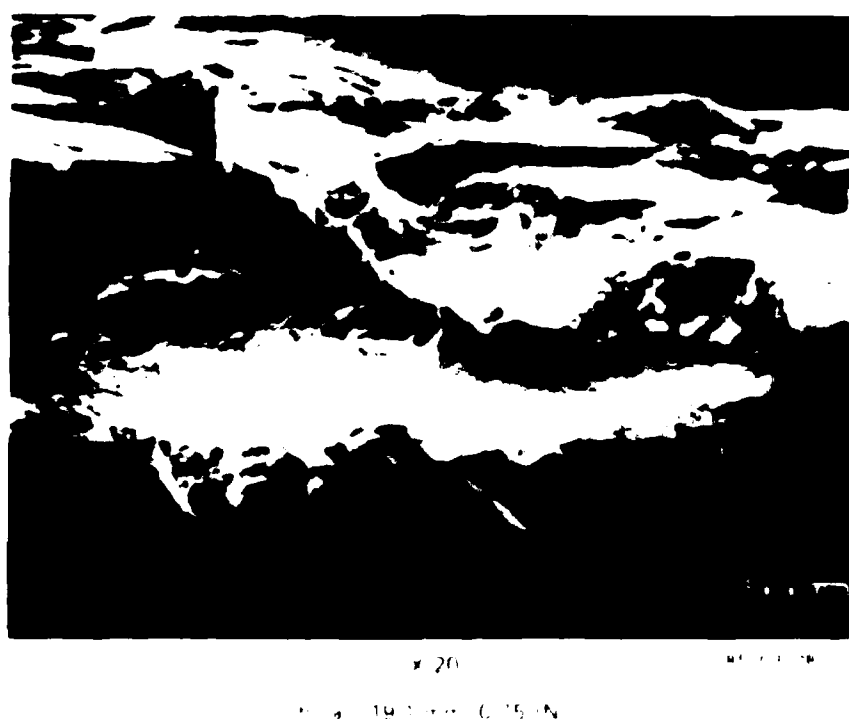
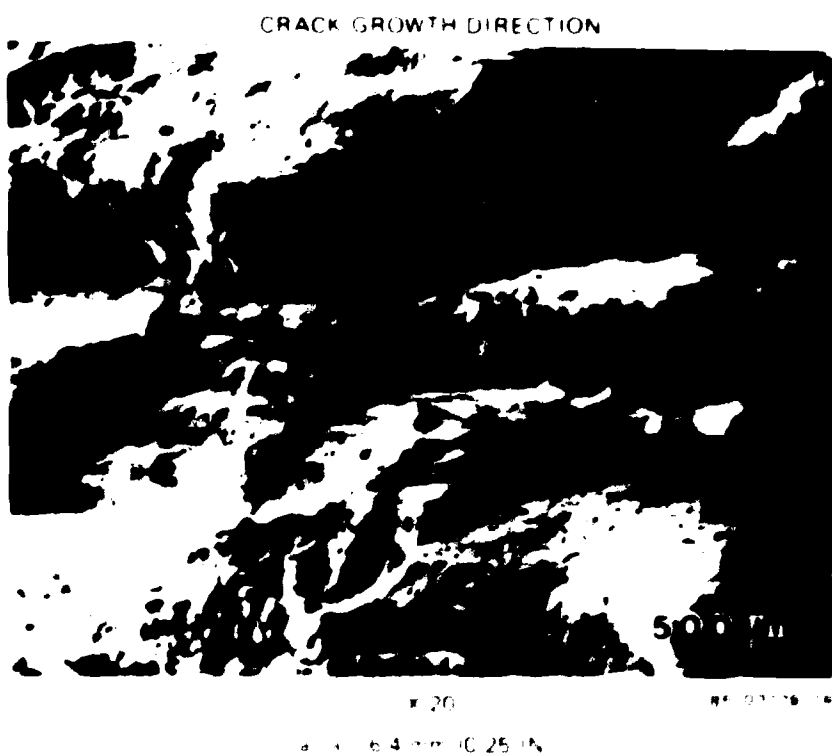


FIGURE 26 FRACTURE SURFACE OF ALLOY 32CU TD SPECTRUM SHOWING EXTREMELY COARSE TOPOGRAPHY

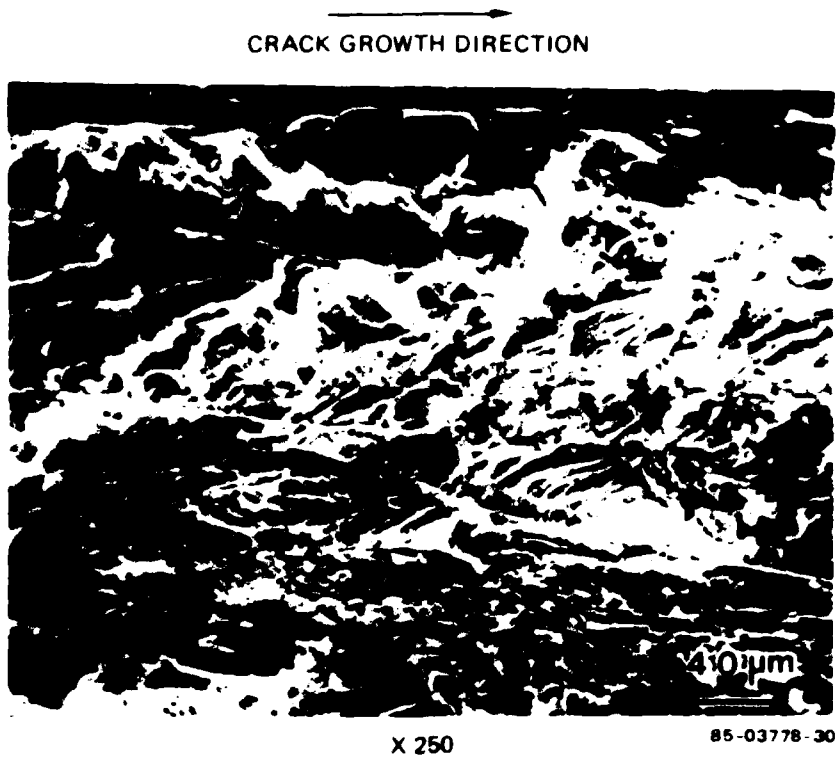
time that such planar fracture corresponds with the expected high degree of slip planarity in an underaged alloy.

It was mentioned in Subsection 3.5.2 that the scatter in spectrum FCP data was greater for the underaged alloys than for the peak aged alloys. The greater degree of surface roughness for the underaged alloys suggests greater degrees of both crack closure and branching, both of which are known to reduce crack-growth rates. Local changes in either crack-tip geometry or fracture surface roughness immediately behind the crack tip will be of greater magnitude in the underaged condition, causing greater local acceleration or deceleration in crack propagation rates and the FCP data to fluctuate more about the mean trend.

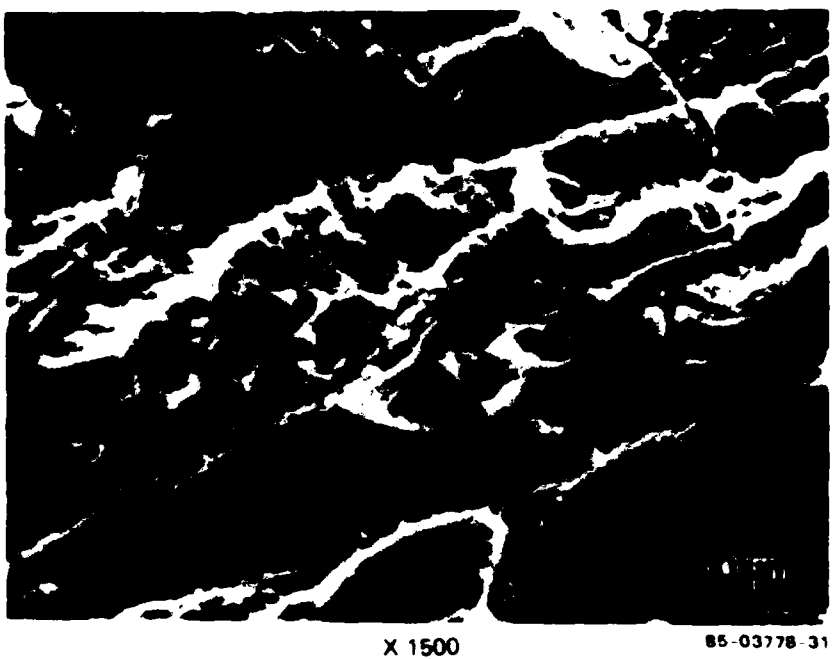
3.6.2 Microscopic Fracture Mechanisms

There are two fracture mechanisms which are most characteristic of the spectrum fatigue surfaces for all of the aluminum-lithium alloys tested. One is basic fatigue "striation" formation, though the lines on the fracture surface cannot be correlated with individual load excursions for such complex spectra. There are, however, noticeable differences in the character of these striations among the specimens; these will be discussed below. The other fatigue fracture mechanism is characterized by the planar faces pointed out in Figure 16, for which very fine-scale dimples often can be seen. Again, more will be said regarding this mechanism subsequently. To streamline the discussion of fractography, the TD fractures will be examined first in some detail. The TC fractures will be discussed later, concentrating only on the differences between TC and TD mechanisms.

The fatigue striations generally are superimposed on the rough background texture of the fracture surface. Figure 27 shows this coarse topography for 110K (TD), with the striations evident at higher magnification ($\times 500$). These striations are relatively flat indicating a relatively small amount of crack tip plasticity and blunting during the fracture process, such shallow markings often are referred to as "brittle" striations. Particularly at the low K_{hmax} levels experienced at this crack length (6.4 mm), there is little evidence of void coalescence as a fracture mechanism. Brittle striation formation persists as the dominant crack growth mechanism at longer crack



a "BRITTLE" STRIATIONS SUPERIMPOSED ON ROUGH SURFACE



b DETAIL OF AN AREA IN a

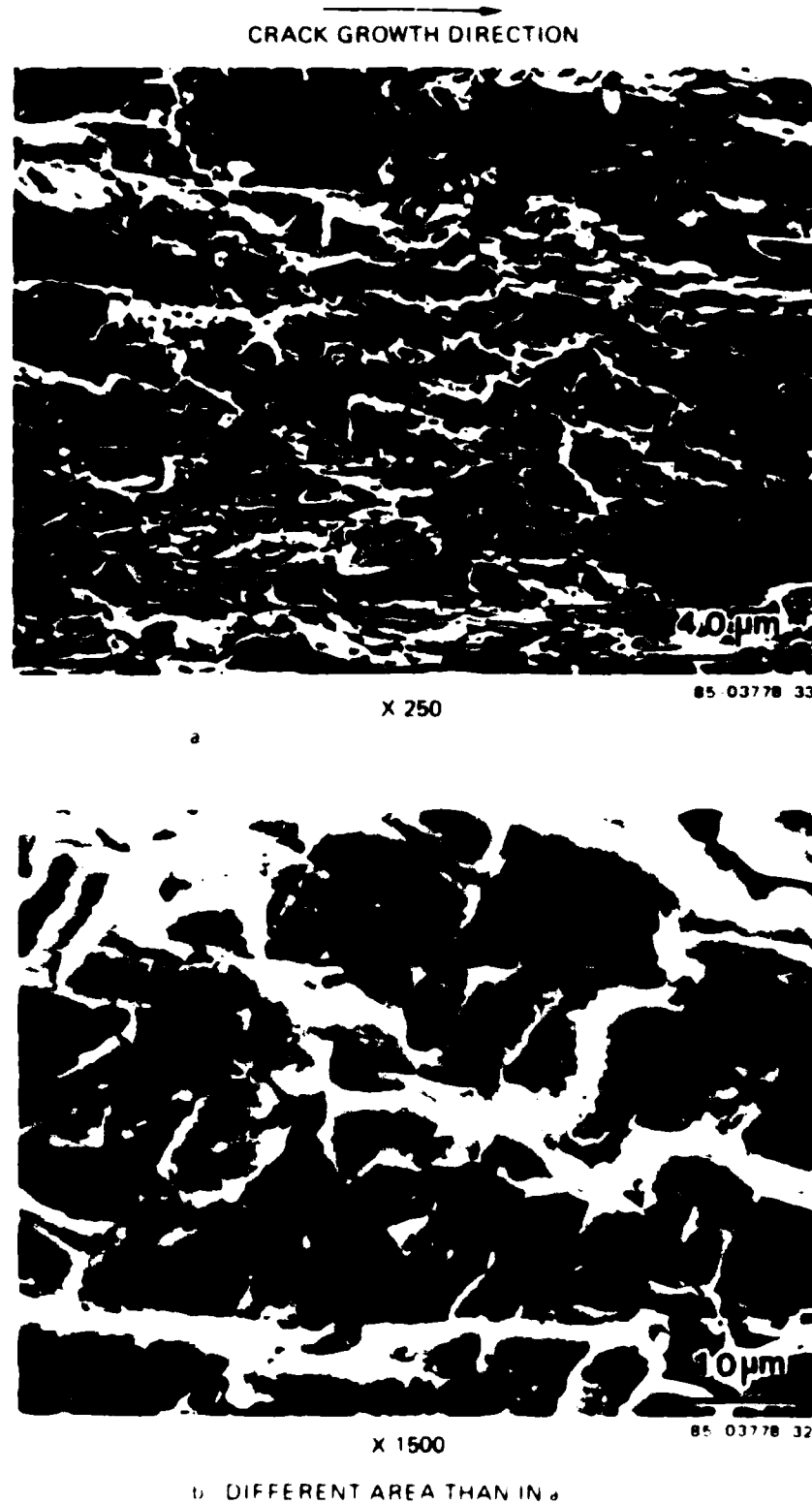
FIGURE 27. FRACTURE SURFACE OF ALLOY 32C8, TD SPECTRUM,
AT $a = 6.4 \text{ mm (0.25 IN.)}$

lengths (19.1 mm - Figure 28), although the general fracture topography changes. This more blocky appearance (Figure 28) begins to take on a character suggestive of intergranular fracture; the continued presence of striations, however, indicates that fracture remains transgranular. Intergranular fracture is characteristic of unstable fracture in all these alloys and will be seen later.

Underaging these alloys results in a mixed fracture mode at all crack lengths. Figure 29 shows striations in 32CU (TD) at both crack lengths; these striations are flat and brittle in appearance, as in the peak-aged alloy. Notice, though, that at 19.1 mm (Figure 29b) there is some secondary cracking (tearing) associated with striations. This has been seen previously in both Phases I and II.^(1,2) These striations occur toward the edges of the specimen, in regions more likely to experience plane stress conditions. At the center of the specimen, the predominant fracture mechanism is the planar type seen in Figure 26. At higher magnifications (Figure 30) these planar features are seen to be covered with very shallow dimples.

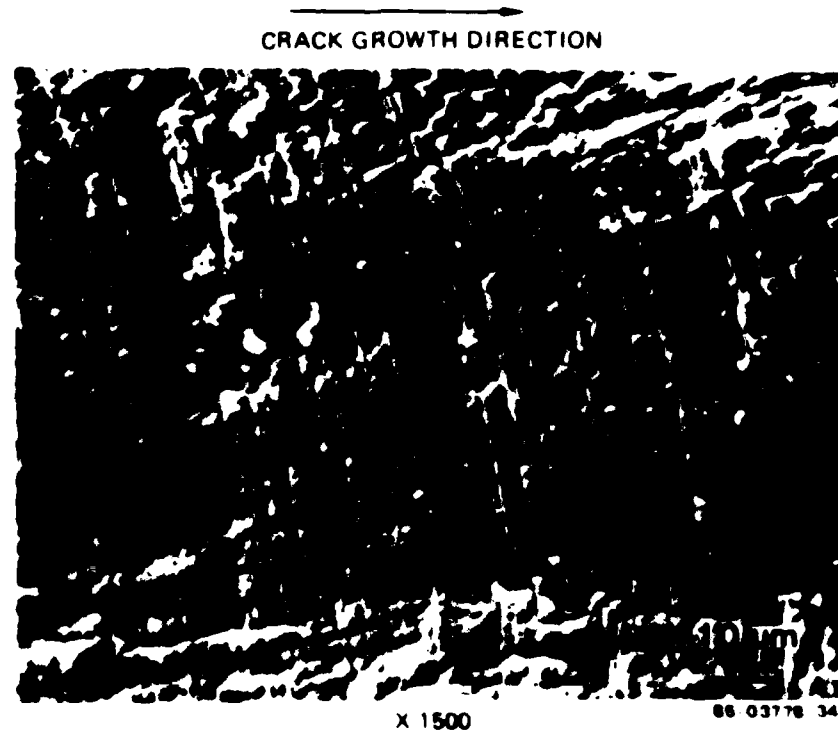
As described previously, these ternary and quaternary Al-Li alloys are especially prone to planar deformation in an underaged temper. The broad, flat fracture planes such as in Figure 26 suggest that crack growth is occurring along slip bands. The inclination of the local slip band fracture plane is at various angles, which incorrectly suggests an intergranular fracture mechanism. Because the grain structures of these alloys are very lamellar with most of the grain boundary area parallel to the rolling plane, intergranular fracture would occur in that orientation. Furthermore, characteristic intergranular fracture is seen during unstable fracture (see below).

For the 321C8 alloy, striation formation once again is the dominant crackgrowth mechanism, as shown in Figure 31. In some instances, though, the fracture surfaces are obscured by large patches of debris (presumably oxides) such as those seen in the right side of Figure 31a. This debris indicates substantial crack closure has occurred, even in the TD spectrum. The minimum loads in this spectrum reach $-0.30P_{max}$, so some surface contact was expected.

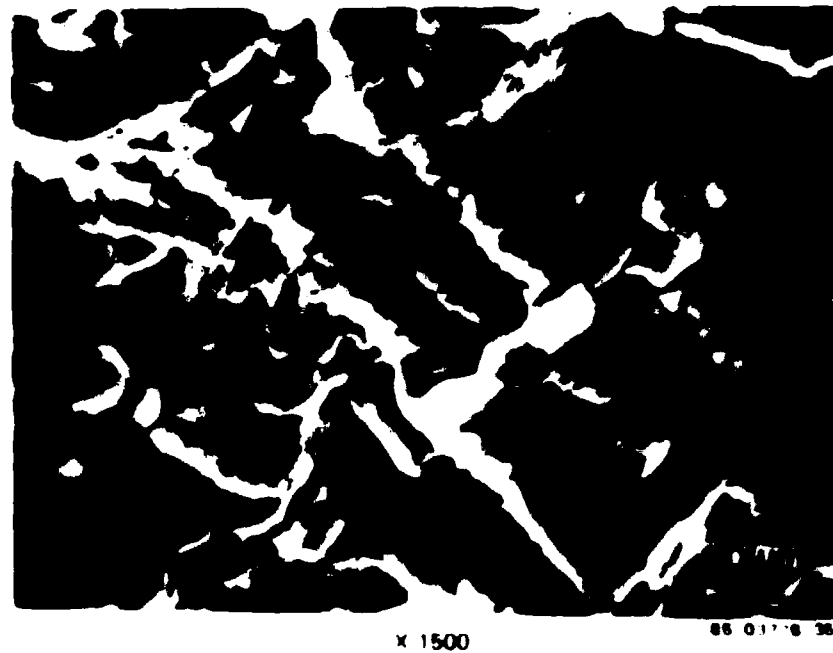


b. DIFFERENT AREA THAN IN a.

**FIGURE 28. FRACTURE SURFACE OF ALLOY 32C8, TD SPECTRUM,
AT $a = 19.2 \text{ mm (0.75 in.)}$ VERY FINE STRIATIONS
SUPERIMPOSED ON A "BLOCKY" FRACTURE**

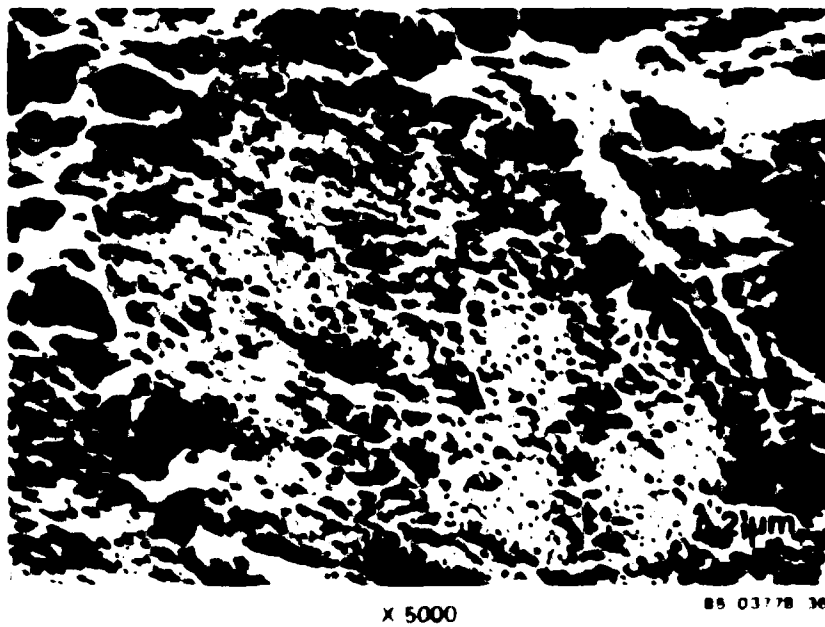
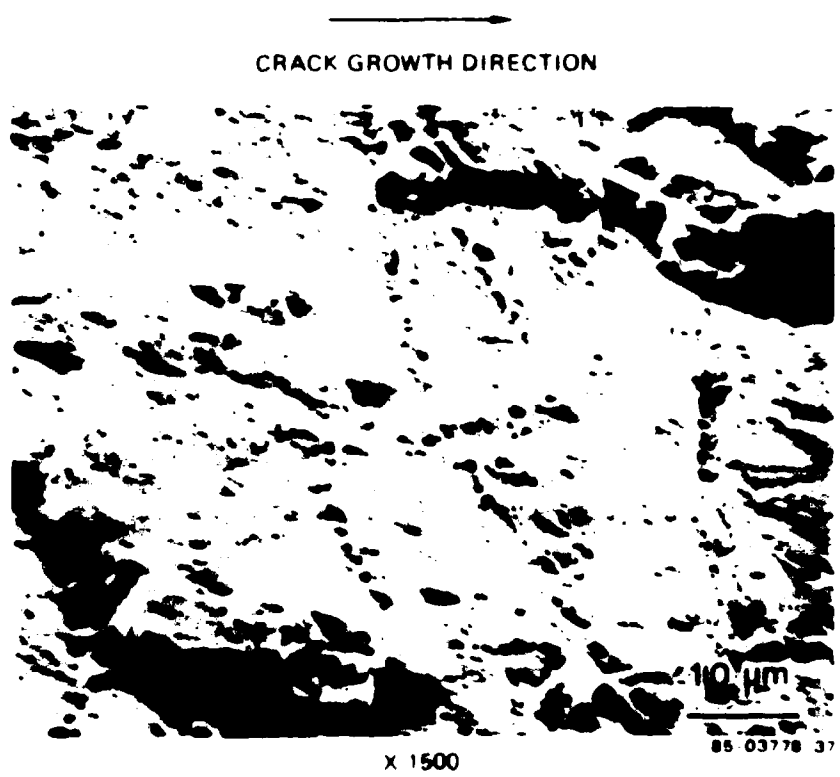


a AT $\dot{a} = 6.4 \text{ mm (0.25 IN) }$ STRIATIONS ARE VERY SHALLOW



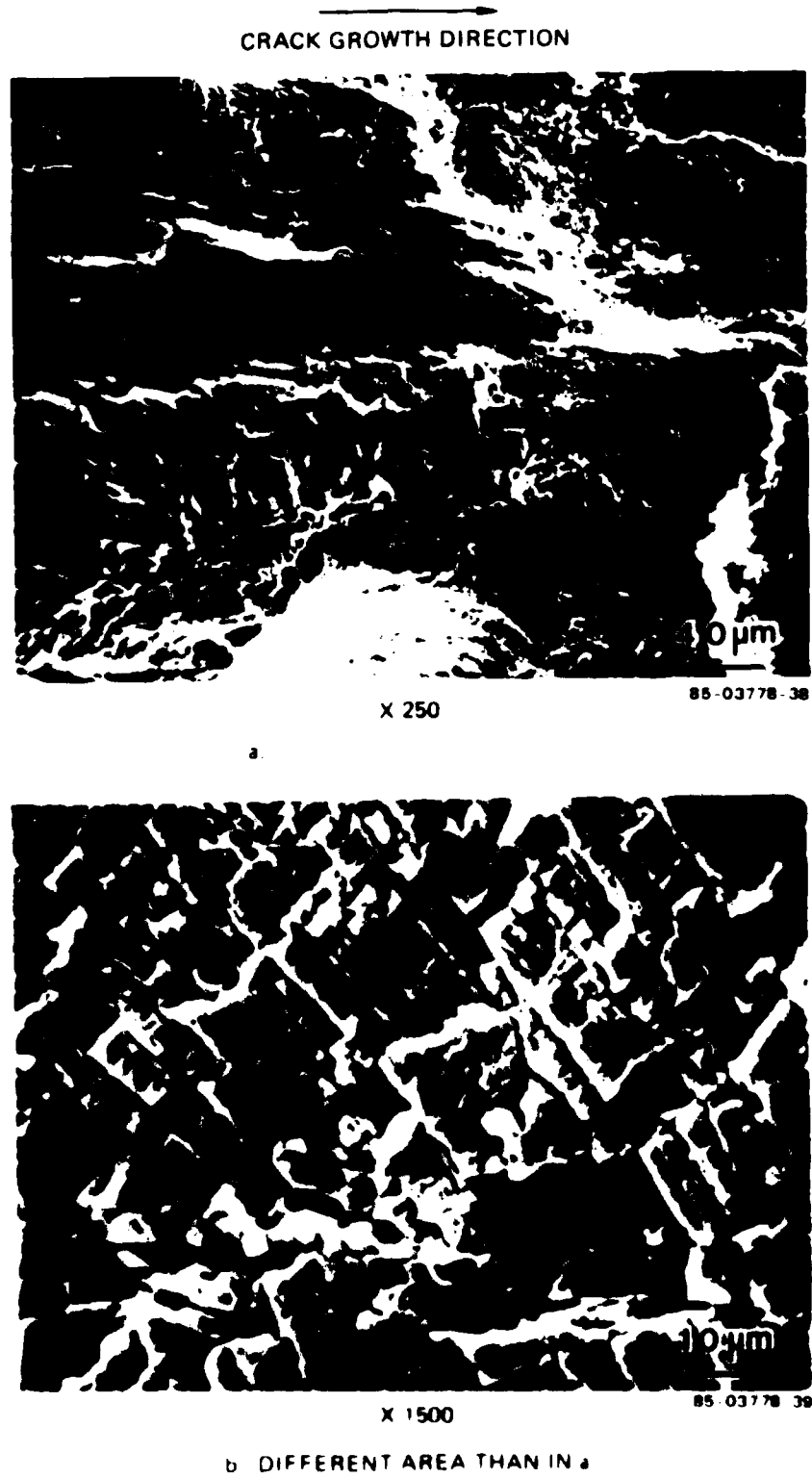
b AT $\dot{a} = 19.1 \text{ mm (0.75 IN) }$ STRIATIONS ARE MORE DUCTILE THAN IN a

FIGURE 29. FRACTURE SURFACE OF ALLOY 32CU, TD SPECTRUM



b. DETAIL OF AN AREA IN a

FIGURE 30 FRACTURE SURFACE OF ALLOY 32CU. TD SPECTRUM,
AT $a = 19.1 \text{ mm (0.75 in)}$ CLOSEUP OF PLANAR REGIONS IN FIGURE 26b
SHOWING SHALLOW DIMPLES SUPERIMPOSED ON THESE FACES



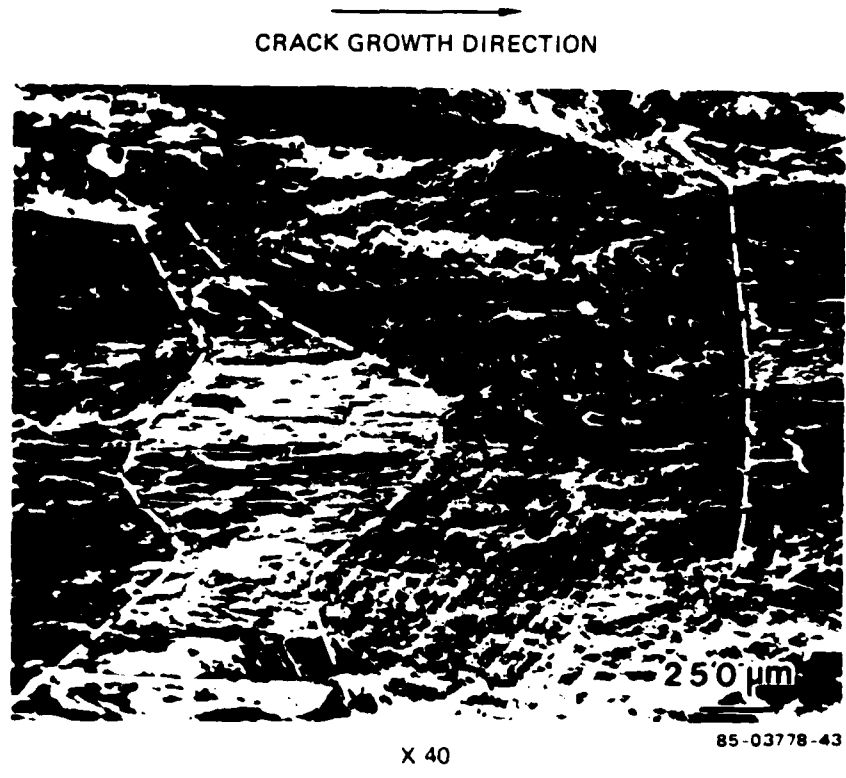
b. DIFFERENT AREA THAN IN a.

**FIGURE 31. FRACTURE SURFACE OF ALLOY 321C8, TD SPECTRUM,
AT $a = 6.4 \text{ mm}$ (0.25 IN.). PREDOMINANTLY STRIATED GROWTH
IN THIS REGION, ALTHOUGH PART OF THE FRACTURE IS
OBSCURED BY HEAVY OXIDE DEBRIS (RIGHT-HAND SIDE OF a.)**

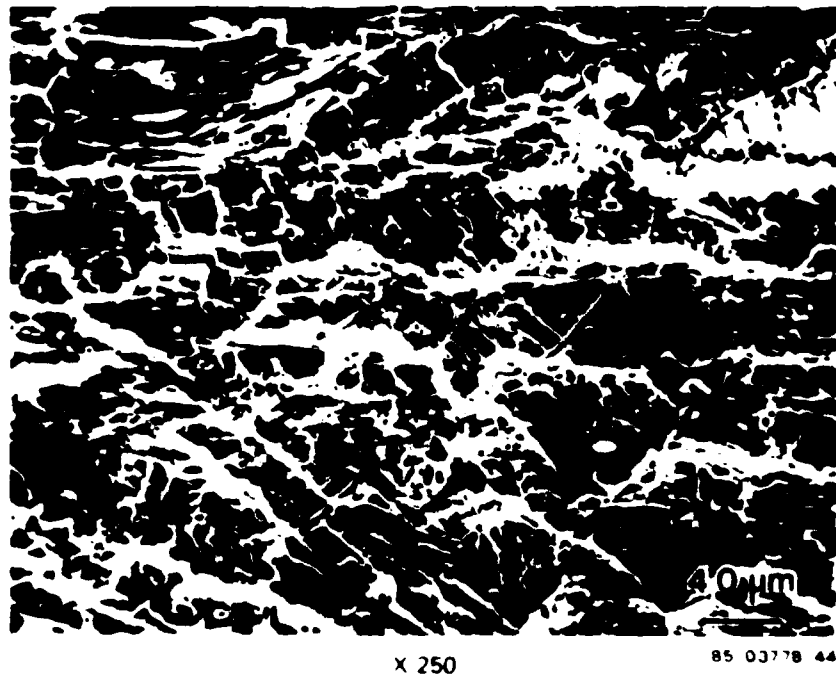
Figure B-2 (Appendix B) shows that crack growth in 321C8 was approaching instability at a crack length of 19.1 mm for all spectra, as evidenced by the extremely high slope of the α versus H curve. The fracture surface similarly indicates incipient fracture by the presence of coarse bands of alternating stable and unstable crack growth. Figure 32a shows a series of these bands; the darker regions, labeled 1 and 3, contain predominantly coarse striations as seen in Figure 32b, while regions 2 and 4 are predominantly intergranular (unstable) fracture (Figure 32c). In fact, region 4 is the final fracture zone for this specimen. Figure 32d shows the abrupt transitions from region 3 to 4 at the onset of final fracture. Upon close examination (Figure 32e), these intergranular regions are seen to consist of very shallow dimples superimposed on the intergranular facets. This type of fracture often has been seen in Al-Li alloys⁽¹⁷⁾ and is attributed to void formation in PFZs. The presence of these coarse bands of alternating fracture mode suggests that local instability occurs during high load excursions in the spectrum as $K_{h\max}$ approaches the toughness of the alloy. The unstable "pop-in" fractures occur in the specimen center, where a more triaxial stress state exists. Final fracture can be delayed, however, as the alloy has the ability to arrest at least several of these instabilities.

In the case of the mixed structure alloy, several fracture modes occurred simultaneously, including the coarse banding indicating local instability even at the beginning of the test. This early instability is consistent with the substantially lower toughness levels in the 32Mx alloys (Table 5). Figure 33a shows the coarse bands at the specimen edge (top of photo), with predominant striation formation occurring toward the specimen center (Figure 33b). As the crack length increases, the crack growth switches to more of the planar mechanism, even in the peak-aged condition (Figure 34).

It was noted in the previous section that a particular difference between TD and TC spectrum fractures was the greater degree of surface abrasion and fretting debris in the latter. Figure 35a indicates the presence of striations for 32CU (TC) near the beginning of the fatigue test, with substantial amounts of debris along the top and bottom of the fractograph. This debris is shown more closely in Figure 35b, and consists mostly of somewhat spherical particles from 0.1 - 5 μm in diameter; macroscopically, these regions of debris are gray to black. The original fracture features have

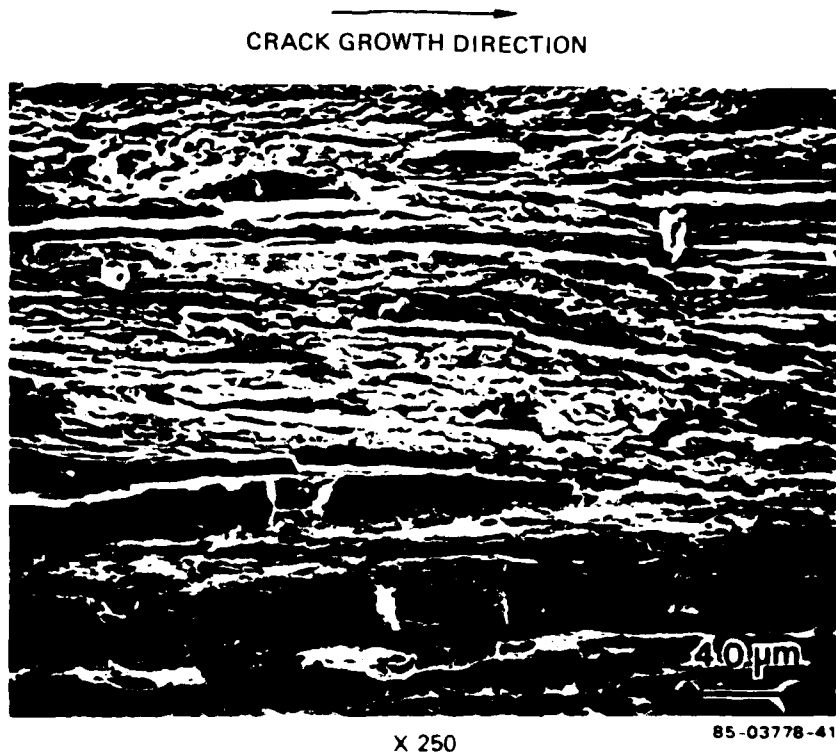


a REGION 2 INDICATES POP-IN FRACTURE AREA PRIOR TO SPECIMEN FRACTURE

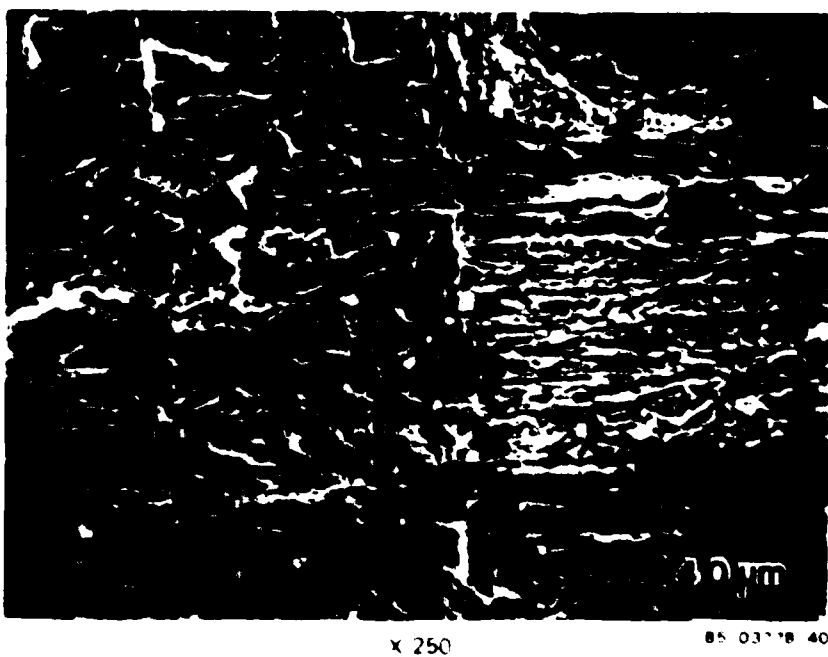


b STRIATED GROWTH (REGION 1 OF a)

FIGURE 32. FRACTURE SURFACE OF ALLOY 321C8, TD SPECTRUM, 19.1 mm (0.75 IN.)

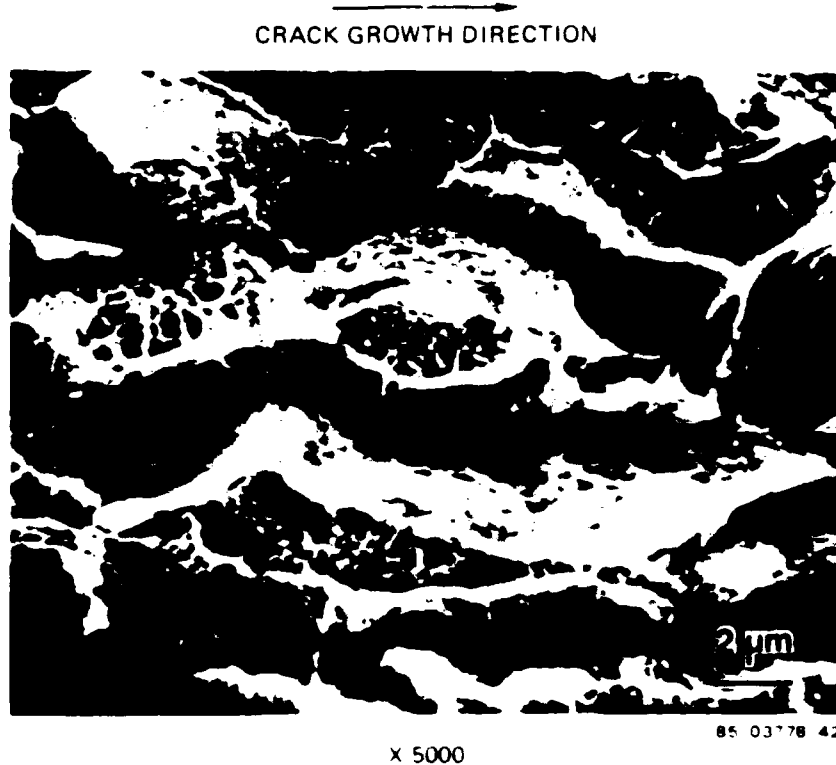


c. UNSTABLE INTERGRANULAR FRACTURE OF REGION 2 OF a



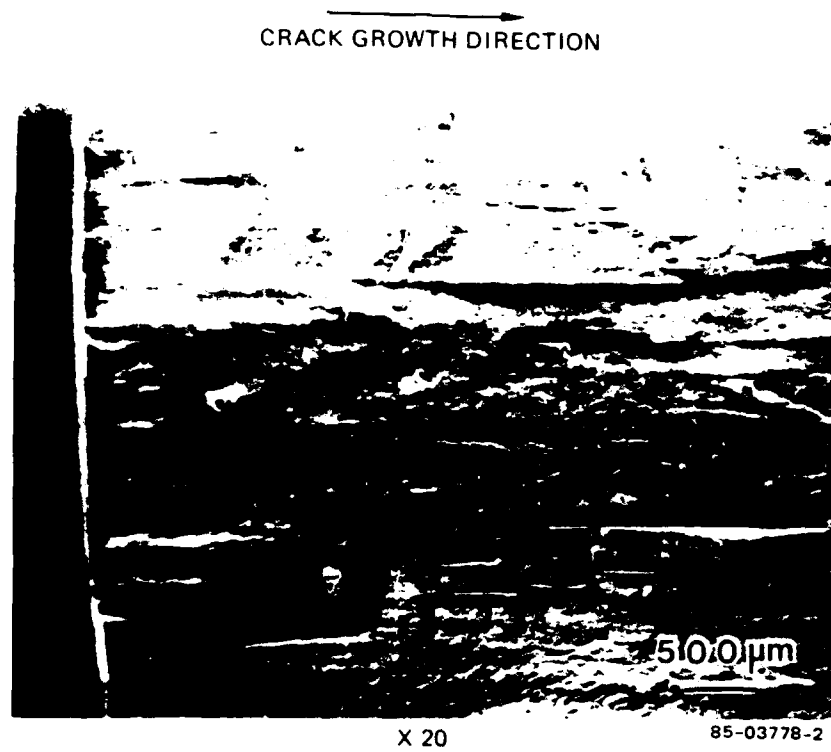
d. TRANSITION FROM STRIATED GROWTH REGION OF c. TO FINAL UNSTABLE FRACTURE REGION 4

**FIGURE 32 FRACTURE SURFACE OF ALLOY 321C8 TD SPECTRUM
19.1 mm (0.75 IN) - CONT**

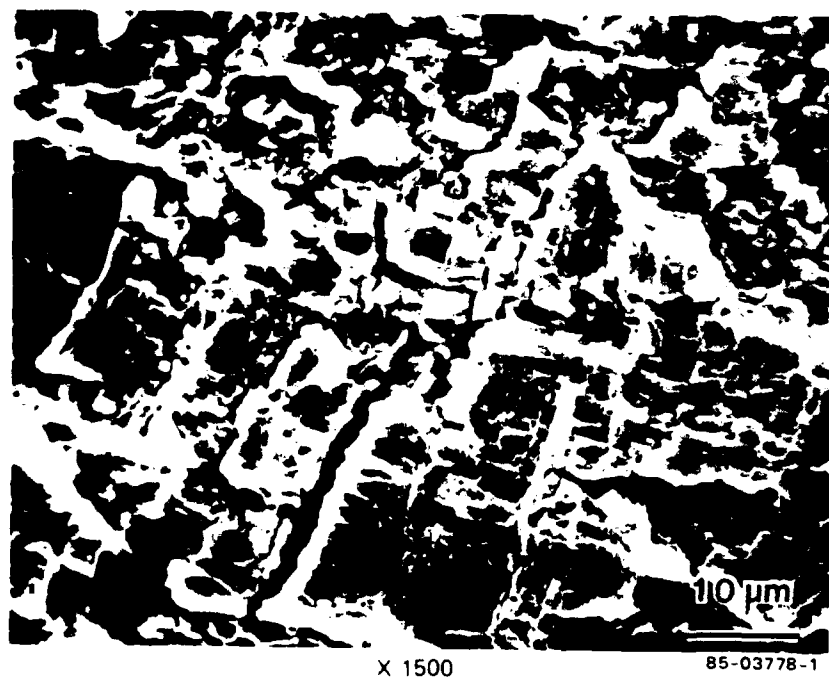


e SHALLOW MICROVOIDS ON INTERGRANULAR FACES IN REGION 4 OF a

**FIGURE 32. FRACTURE SURFACE OF ALLOY 321C8, TD SPECTRUM,
19.1 mm (0.75 IN.) (CONT)**



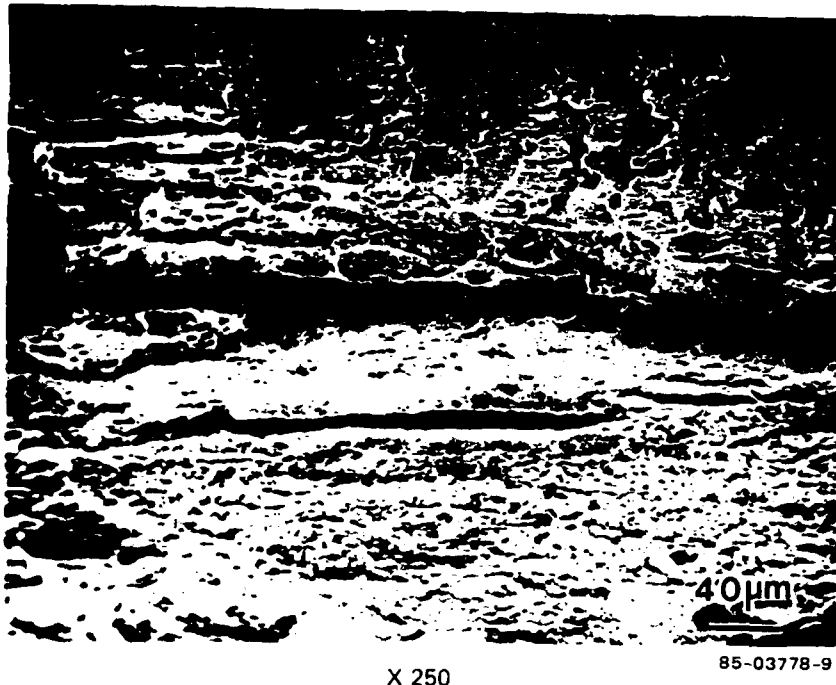
a MIXED FRACTURE MODES WITH UNSTABLE POP-IN FRACTURES NEAR SPECIMEN EDGE



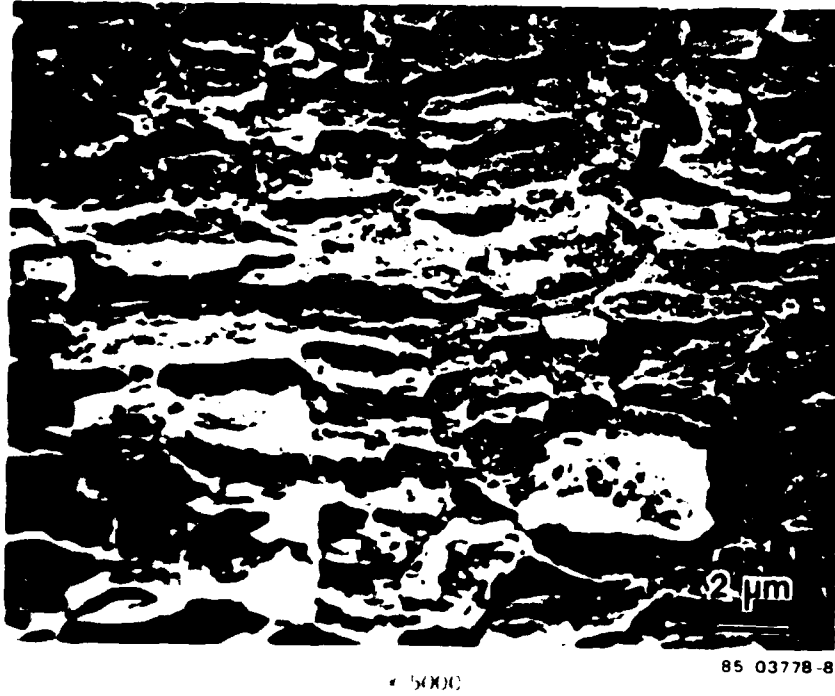
b STRIATIONS IN CENTRAL REGION

FIGURE 33. FRACTURE SURFACE OF ALLOY 32M8, TD SPECTRUM,
AT $a = 6.4 \text{ mm (0.25 IN.)}$

CRACK GROWTH DIRECTION

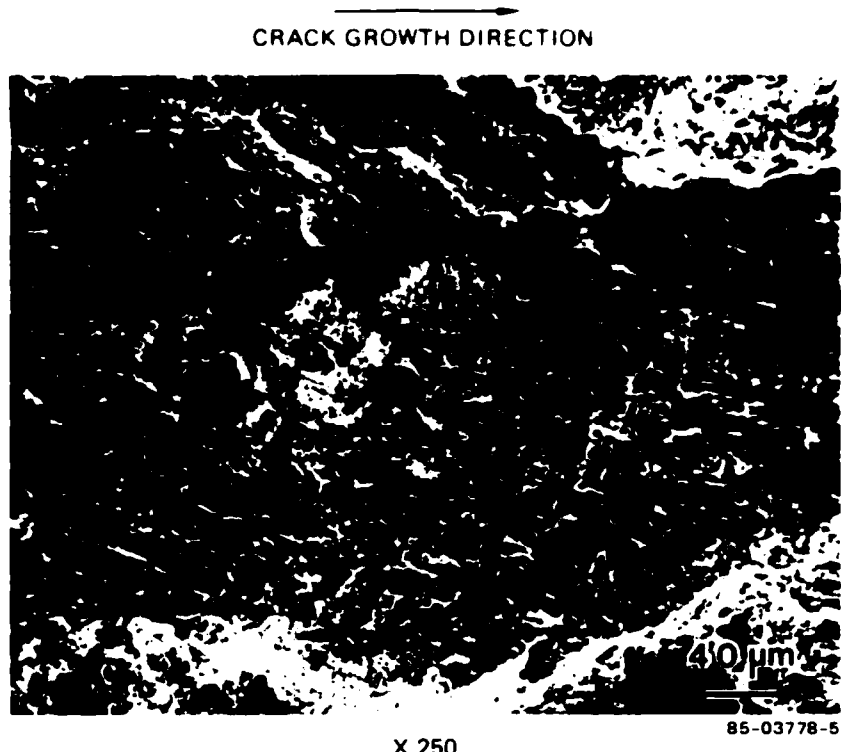


85-03778-9



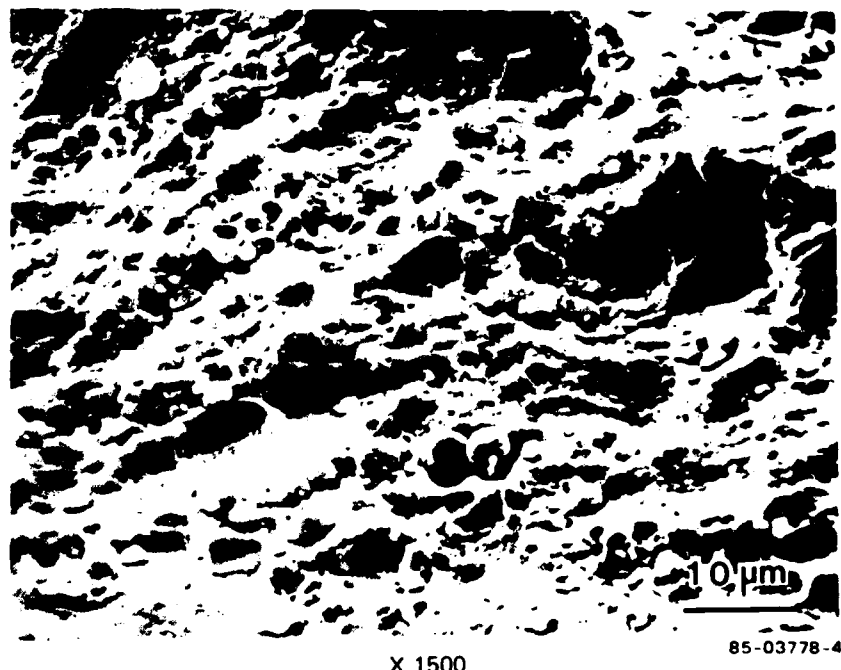
85-03778-8

SCANNING ELECTRON MICROGRAPH OF THE SURFACE OF ALLOY 32M8, TD SPECTRUM, AT 25°C, DURING CRACK GROWTH AND CRACK FRACTURE WITH SHALLOW DIMPLES



X 250

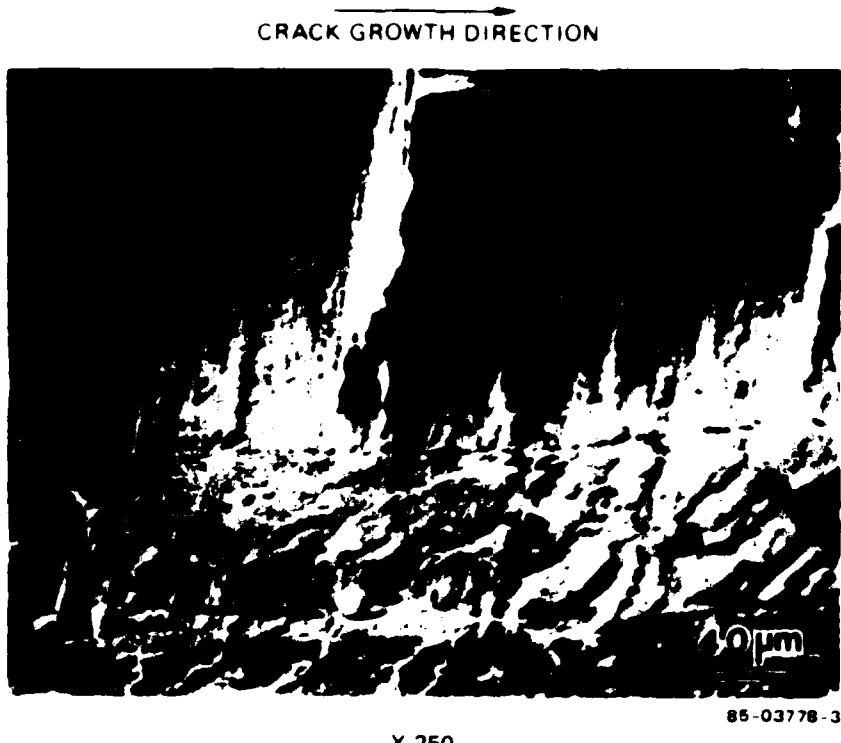
a. STRIATIONS AND SURFACE ABRASION AND DEBRIS AT $a = 6.4 \text{ mm}$ (0.25 IN.)



X 1500

b. SPHERICAL DEBRIS AT HIGHER MAGNIFICATION AT $a = 19.1 \text{ mm}$ (0.75 IN.)

FIGURE 35. FRACTURE SURFACE OF ALLOY 32 CU, TC SPECTRUM

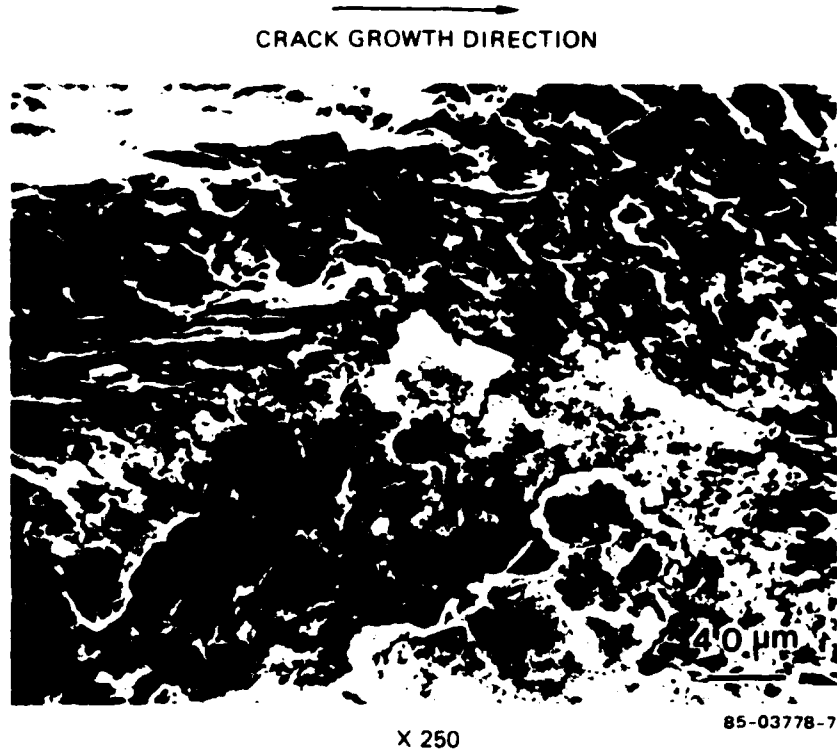


c. PLANAR FRACTURE AT $a = 19.1$ mm (0.75 IN.)

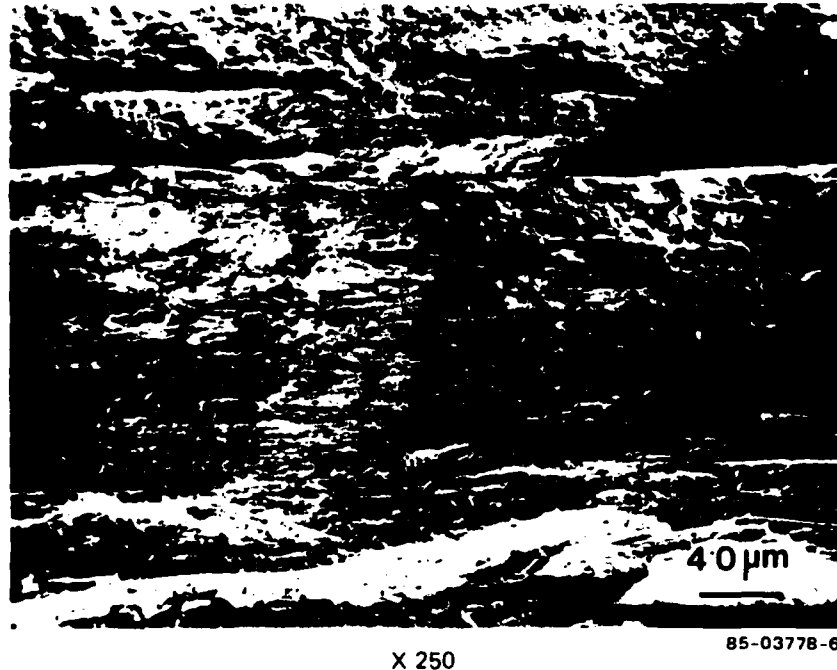
FIGURE 35. FRACTURE SURFACE OF ALLOY 32CU, TC SPECTRUM (CONT)

been obliterated by the repeated rubbing together of the fracture surfaces and the abrading action of the oxide debris. When the original surface is visible at greater crack lengths, the same planar fracture mechanism occurs for the 32CU specimen as was seen in the case of the TD spectrum.

Further evidence of abrasion and debris superimposed on striated fatigue crack growth is seen for the 321C8 alloy tested using the TC spectrum in Figure 36a. This same test specimen also exhibited the banding at high K_{hmax} levels indicative of local crack instability prior to final fracture (Figure 36b), as had been the case for the same alloy tested using the TD spectrum. For the 321CU alloy, oxide debris is littered across the fracture at 6.4 mm but does not cover the flat striations underneath (Figure 37a). Planar fracture again is observed at higher K_{hmax} levels (Figure 37b) in contrast to the mixed striation plus pop-in fracture for the peak-aged alloy at the same crack length (Figure 36b).

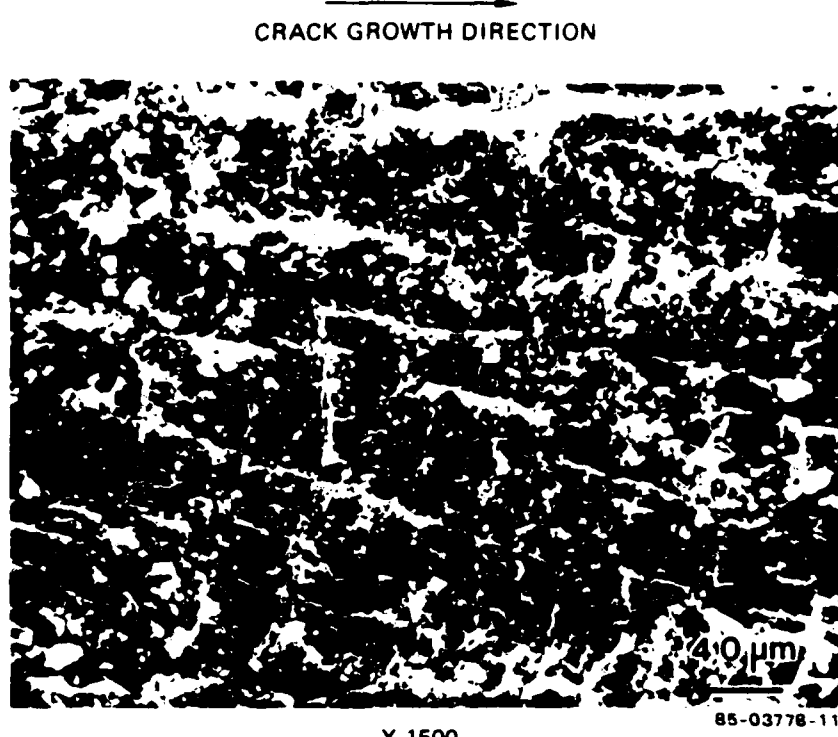


a. SUBSTANTIAL SURFACE ABRASION AND DEBRIS AT $a = 6.4 \text{ mm (0.25 IN.)}$

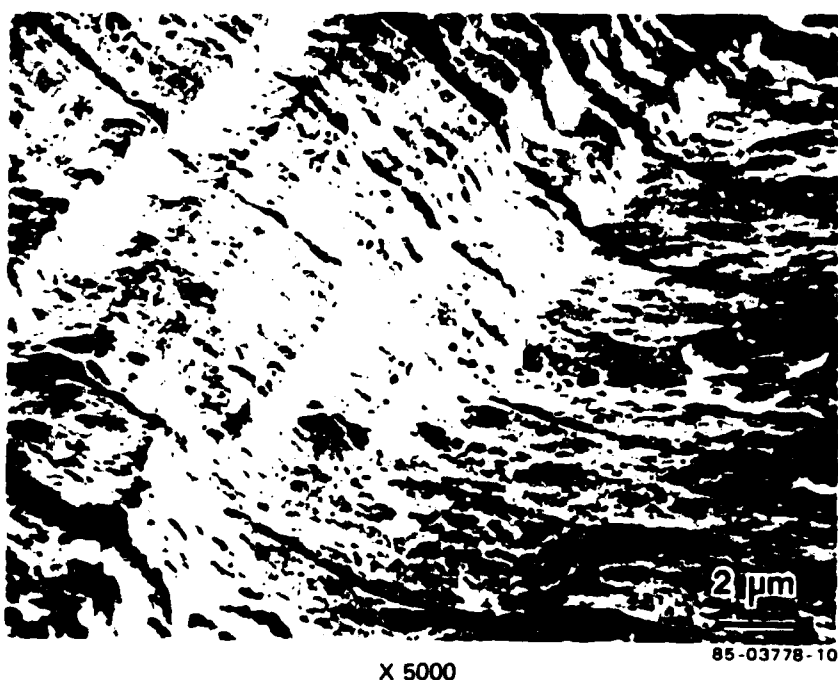


b. BANDED FRACTURE INDICATING MULTIPLE POP-IN FRACTURES AT $a = 19.1 \text{ mm (0.75 IN.)}$

FIGURE 36. FRACTURE SURFACE OF ALLOY 321C8, TC SPECTRUM



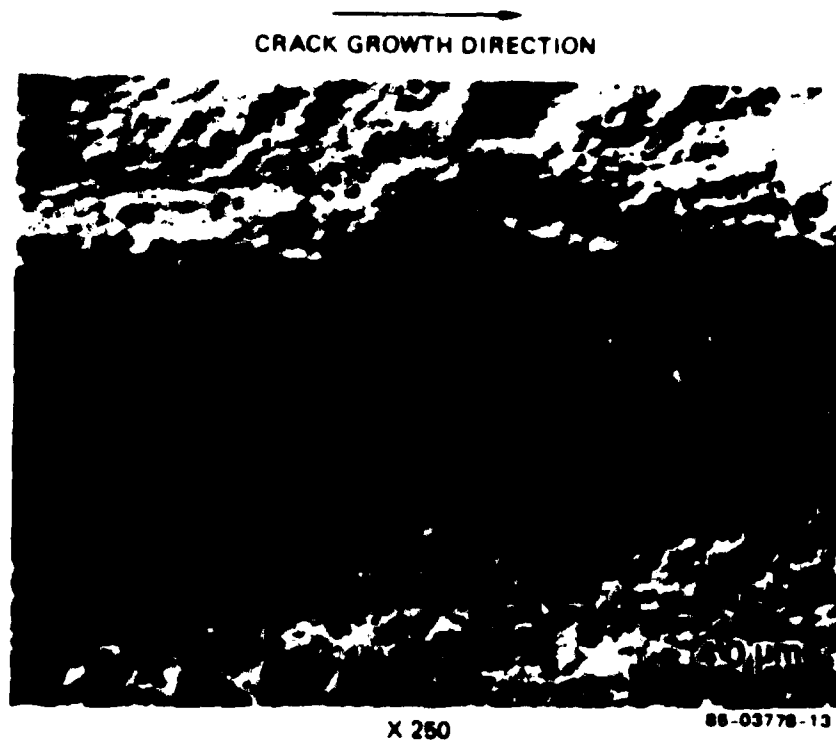
a. FRETTING DEBRIS OVER STRIATIONS AT $a = 6.4$ mm (0.25 IN.)



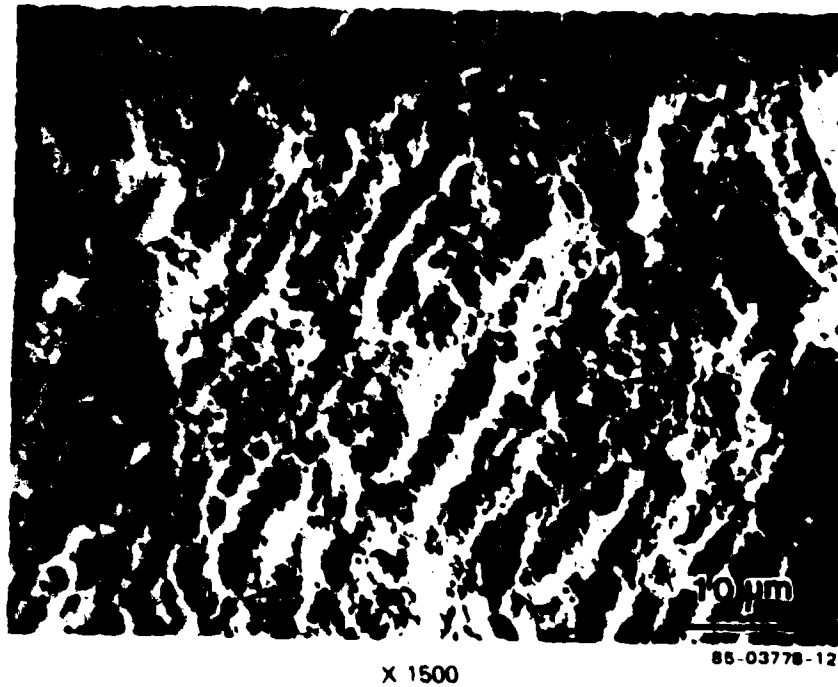
b. PLANAR FRACTURE AT $a = 19.1$ mm (0.75 IN.)

FIGURE 37. FRACTURE SURFACE OF ALLOY 321CU, TC SPECTRUM

A mixture of striations and abrasion also can be seen in Figure 38 for the 32MU alloy. An extreme example of abrasion is shown in Figure 38; the furrows in this fractograph indicate that the hard oxide debris has been pushed along the surface, gouging it out with every load cycle. It is important to remember, in summary, that abrasion and fracture surface debris are not crack-growth mechanisms in themselves, but do indicate that substantial crack closure has occurred. The reduction in effective crack-tip stress intensity factor which results from high-closure levels can decrease the rate of crack growth significantly.



a. STRIATIONS AND ABRASION AT $a = 6.4$ mm (0.25 IN.)



b. SEVERE ABRASION OF SURFACE AND FURROWING OF SURFACE BY DEBRIS INDICATING SUBSTANTIAL CRACK CLOSURE AT 19.1 mm (0.75 IN.)

FIGURE 38. FRACTURE SURFACE OF ALLOY 32MU, TC SPECTRUM

4. SUMMARY AND CONCLUSIONS

An investigation summarized in Volume I of this report led to the selection, fabrication, and critical evaluation of the aluminum-lithium type alloys with systematically controlled microstructures described in Volume II of the report. Underaged and peak aged tempers were studied in two alloy chemistries represented by the nominal compositions Al-3Cu-2Li-0.1Zr and Al-3Cu-2Li-1Mg-0.1Zr. Grain structure was also varied in the Al-Cu-Li-Zr alloy. Microstructure, tensile properties, and fracture toughness were characterized. FCP tests were conducted on specimens of each alloy for both constant-amplitude loading (including the low ΔK region) and two F-18 load spectrums. The spectrum FCP testing was performed at a maximum peak stress of 145 MPa (21 ksi). The alloys were also tested using three modified (simplified) spectrums. Pertinent fracture surface features were documented on the spectrum fatigue specimens.

The constant-load-amplitude FCP tests were performed on each of the six alloy variants to provide a baseline characterization of steady-state FCP response. The following observations can be made about the constant-load-amplitude FCP behavior of these alloys:

1. Resistance to FCP is dependent on temper especially in the near-threshold regime ($da/dN < 10^{-8}$ m/cycle)
2. In each alloy, the underaged condition demonstrates greater resistance to FCP relative to the peak aged condition of that alloy
3. The 32CU alloy possesses the greatest resistance to FCP.

Macroscopic examinations of the constant-load-amplitude FCP specimen fracture surfaces were performed. All six of the alloy/temper/grain structure combinations exhibited especially rough and coarse fracture surfaces. In some cases, a significant amount of fretting oxide debris covered areas of the fracture surfaces, which indicated substantial fracture surface rubbing.

Spectrum FCP tests were conducted on each of the six alloy variants, using two complex F-18 load histories. These results provide baseline information for the analysis of spectrum modifications.

Several observations can be made based on the results of spectrum fatigue tests conducted at a maximum peak stress of 145 MPa (21 ksi):

1. The fatigue life was longer for each alloy in the underaged condition relative to the peak aged condition regardless of the particular spectrum
2. The 32CU alloy demonstrated the longest life under the TD spectrum followed by the 321CU alloy, while the 321CU alloy possessed the greatest resistance to the TC spectrum followed by the 32CU alloy; the ranking of the other four alloys was consistent under these spectrums, which in order of decreasing life, was 32MU, 32C8, 321C8, 32M8
3. The underaged alloys showed the greatest difference in life between the TD and TC spectrums, with the 32CU alloy having only 25 percent of the TD life under the TC spectrum
4. The relative TD ranking of the six alloys remained unchanged under the TDR racetrack modification; but under the TCR spectrum, the positions of the 321CU and 32CU alloys were reversed, relative to the TC ranking
5. The TCZ modification of the TC spectrum reversed the ranking of the 321CU and 32CU alloys, but the other four alloys remained in the same relative positions
6. Elimination of all compressive loads through the TCZ modification resulted in the longest spectrum life relative to the other spectrums for the alloys in the underaged condition; however, this trend was not evident for alloys in the peak aged condition
7. In the same temper, the coarse-grained alloys have longer lives than the mixed microstructure alloys
8. The lives for the coarse-grained alloys with and without magnesium are similar for the same temper, with the magnesium-free alloy generally having slightly longer lives

9. The experimental underaged alloys had longer spectrum fatigue lives than the commercial alloys evaluated in this program (see Volume I of this report).

The most significant trend in the FCP data (constant and variable load amplitude) is that the underaged alloys with predominant planar slip deformation had longer fatigue lives than the peak aged alloys that deform more homogeneously. The characteristics of the age-hardening precipitates control the degree of slip planarity, with the predominant strengthening phase being the shearable Al_3Li (δ') in the underaged temper leading to enhanced slip planarity. Concentrated planar slip results in greater crack path tortuosity and branching, which causes enhanced crack closure and a reduction in stress intensity at the crack tip (ΔK_{eff}).

REFERENCES

1. Chanani, G.R., Telesman, I., Bretz, P.E., and Scarich, G.V., "Methodology for Evaluation of Fatigue Crack-Growth Resistance of Aluminum Alloys Under Spectrum Loading," Technical Report (Phase I, Final Report), Naval Air Systems Command, Contract N00019-80-C-0427, April 1982.
2. Scarich, G.V. and Bretz, P.E., "Investigation of Fatigue Crack Growth Resistance of Aluminum Alloys Under Spectrum Loading," Technical Report (Phase II, Final Report). Naval Air Systems Command, Contract N00019-81-C-0550, April 1983.
3. Chanani, G.R., Scarich, G.V., Bretz, P.E., and Sheinker, A.A., "Spectrum Fatigue Crack Growth Behavior of Aluminum Alloys," Proceedings of the Sixth International Conference on Fracture (ICF6), New Delhi, India, December 1984, Vol. 3, p. 1609.
4. Scarich, G.V., Gambone, M.J., Chanani, G.R., and Bretz, P.E., "Correlation of Fatigue Behavior With Microstructure of 2XXX and 7XXX Aluminum Alloys," Proceedings of the Sixth International Conference on Fracture (ICF6), New Delhi, India, Pergamon Press, "Advances in Fracture Research," December 1984, Vol. 3, p. 2015.
5. Yoder, G.R., Cooley, L.A., and Crooker, T.W., in "Titanium '80," Proceedings of the 4th International Conference on Titanium, Kyoto, 3, Kimura, H. and Izumi, O., Eds., TMS-AIME, 1981, p. 1865.
6. Ibid, in "Fracture Mechanics," Proceedings of the 14th National Symposium on Fracture Mechanics, Los Angeles, Lewis, J.C. and Sines, G., Eds., ASTM STP XXX, 1982, in press.
7. Ibid, Scripta Met., 16, 1982, p. 1021.
8. Lin, G.M. and Fine, M.E., "Effect of Grain Size and Cold Work on the Near Threshold Fatigue Crack Propagation Rate and Crack Closure in Iron," Scripta Met., Vol. 16, 1982, p. 1249.

9. Gray, G.T., III, Williams, J.C., and Thompson, A.A., Met. Trans., 14A, 1983, p. 421.
10. Lindigkeit, J., Terlinde, G., Gysler, A., and Lohrmann, H., Acta Met., 27, 1979, p. 1717.
11. King, J.E., Metal Science, 16, 1982, p. 345.
12. Kuo, V.W.C. and Starke, E.A., Jr., Met. Trans., 14A, 1983, p. 431.
13. Bretz, P.E., Petit, J.L., and Vasudevan, A.K., in Fatigue Crack Growth Threshold Concepts, Davidson, D.L. and Suresh, S., Eds., TMS-AIME, 1984, p. 163.
14. Vasudevan, A.K. and Bretz, P.E., in Fatigue Crack Growth Threshold Concepts, Davidson, D.L. and Suresh, S., Eds., TMS-AIME, 1984, p. 25.
15. Suresh, S., Engineering Fracture Mechanics, 18, 1983, p. 577.
16. Suresh, S., Met. Trans., 14A, 1983, p. 2375.
17. Sanders, T.H., Jr., "Factors Influencing Fracture Toughness and Other Properties of Aluminum-Lithium Alloys," Final Report, Naval Air Development Center Contract N62269-76-C-0271, 1979.
18. Welpmann, K., Peters, M., and Sanders, T.H., Jr., Aluminum, 60, 1984, p. 641.
19. Bretz, P.E. and Sawtell, R.R., "ALITHALITE^R Alloys: Progress, Products and Properties," Proceedings of the 3rd International Aluminum-Lithium Conference, Oxford, 1985 July 8-11, in press.
20. Vasudevan, A.K., Malcolm, R.C., Fricke, W.G., and Rioja, R.J., "Resistance of Fracture, Fatigue, and Stress-Corrosion of Al-Cu-Li-Zr Alloys," Final Report, Naval Air Systems Command Contract N00019-80-C-0569, 1985.
21. Ronald, T.M.F., Hall, J.A., and Pierce, C.M., "Usefulness of Precracked Charpy Specimens for Fracture Toughness Screening Test of Titanium Alloys," Met. Trans., 3, 1973, p. 813.
22. Saxena, A., Hudak, S.J., Jr., Donald, J.K., and Schmidt, D.W., "Computer Controlled K-Decreasing Test Technique for Low Rate Fatigue Crack Growth Testing," JETVA, Vol. 6, 1978.

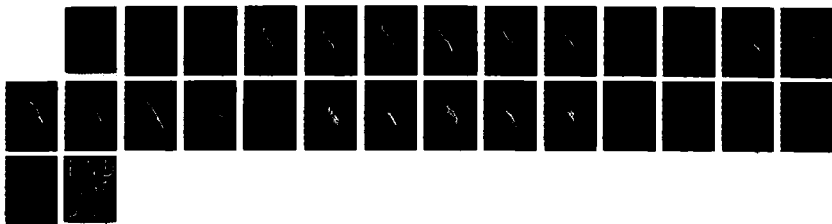
13. Hunt, R.J., "Development of a Proposed Standard Practice for Near-Threshold Fatigue Crack Growth Rate Measurements," ASTM STP 714, 1980.
14. Wetzel, R.V., Ed., "Fatigue Under Complex Loading - Analysis and Experiment," SAE Advances in Engineering, Vol. 6, 1977, pp. 159-162.
15. Chanani, G.R., "Fundamental Investigation of Fatigue Crack Growth Retardation in Aluminum Alloys," AFML-TR-76-156, 1976.
16. Sanders, T.H., Sawtell, R.R., Stanley, J.T., Bucci, R.J., and Thakker, A.B., "The Effect of Microstructure on Fatigue Crack Growth of 7XXX Aluminum Alloys Under Constant Amplitude and Spectrum Loading," NADC Contract No. N00019-76-C-0482, 1978.
17. Bucci, R.J., Thakker, A.B., Sanders, T.H., Sawtell, R.R., and Stanley, J.T., "Ranking 7XXX Aluminum Alloy Fatigue Crack Growth Resistance Under Constant Amplitude and Spectrum Loading," ASTM STP 714, 1980.
18. Bucci, R.J., "Spectrum Loading - A Useful Tool to Screen Effects of Microstructure on Fatigue Crack Growth Resistance," ASTM STP 631, 1977.
19. Jonas, O. and Wei, R.P., "An Explanatory Study of Delay in Fatigue-Crack Growth," Int. J. of Fracture Mechanics, Vol. 7, 1971, p. 116.
20. Schijve, J., "Effect of Load Sequences on Crack Propagation Under Random and Program Loading," Eng. Frac. Mech., Vol. 5, 1973, p. 269.
21. Stephens, R.I., Chen, D.K., and Hom, B.W., "Fatigue Crack Growth With Negative Stress Ratio Following Single Overloads in 2024-T3 and 7075-T6 Aluminum Alloys," ASTM STP 595, 1976.
22. Alzos, W.X., Skat, A.C., Jr., and Hillberry, B.M., "Effect of Single Overload/Underload Cycles on Fatigue Crack Propagation," ASTM STP 595, 1976.
23. Chanani, G.R., "Effect of Thickness on Retardation Behavior of 7075 and 2024 Aluminum Alloys," ASTM STP 631, 1977.

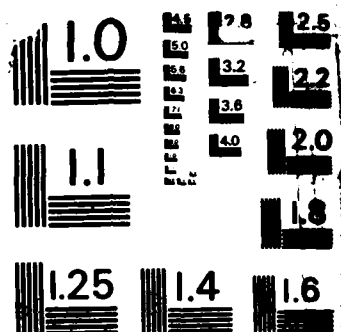
34. Chanani, G.R., "Investigation of Effects of Saltwater on Retardation Behavior of Aluminum Alloys," ASTM STP 642, 1977.
35. Schijve, J., "Observations on the Prediction of Fatigue Crack Growth Propagation Under Variable-Amplitude Loading," ASTM STP 595, 1976.
36. Marrisen, R., Trautmann, K.H., and Nowack, H., "Analysis of Sequence Effects under Variable Amplitude Loading on the Basis of Recent Crack Propagation Models," Presented at the TMS-AIME Fall Meeting, 24-28 October 1982, St. Louis.
37. Mills, W.J. and Hertzberg, R.W., "Load Interaction Effects on Fatigue Crack Propagation in 2024-T3 Aluminum Alloy," Eng. Frac. Mech., Vol. 8, 1976, p. 657.
38. McMillan, J.C. and Hertzberg, R.W., "Application of Electron Fractography to Fatigue Studies," ASTM STP 436, 1968, p. 89.
39. Hsu, T.M. and McGee, W.M., "Effects of Compressive Loads on Spectrum Fatigue Crack Growth Rate," ASTM STP 714, 1980, p. 79.
40. Hardy, H.K. and Silcock, J.M., J. Inst. Met., 84, 1955, p. 423.
41. Von Schneider, K., and Von Heimandahl, M.Z., Metallkde., "Precipitation Behavior of a Commercial Aluminum Copper Lithium Alloy. Part I: The Microstructure After Isothermal Heat Treatment," Vol. 64, 1973, p. 342.
42. Starke, E.A., Jr., Sanders, T.H., Jr., and Palmer, I.G., Journal of Metals, August 1981.
43. Rioja, R.J. and Ludwiczak, E.A., "Identification of Metastable Phases in an Al-Cu-Li Alloy (2090)," Proceedings of the 3rd International Conference on Al-Li-Alloys, 1985 July 8-11, Oxford, in press.
44. Sanders, T.H., Jr., Gu, B.P., Mahalingam, V., and Rioja, R.J., "Coarsening of Al_3Li in a Variety of Al-Li Alloys," Proceedings of the 3rd International Conference on Al-Li Alloys, 1985 July 8-11, Oxford, in press.

AD-A180 355 FATIGUE CRACK-GROWTH RESISTANCE OF ALUMINUM ALLOYS 2/2
UNDER SPECTRUM LOADING (U) NORTHROP CORP HAWTHORNE CA
AIRCRAFT GROUP G V SCARICH ET AL DEC 85

UNCLASSIFIED NOR-85-141-VOL-2 N00014-82-C-0425

F/G 11/6 1 NL





MICROCOPY RESOLUTION TEST CHART
NATIONAL BUREAU OF STANDARDS 1963-A

45. Vasudevan, A.K., Suresh, S., Howell, P.R., and Tosten, M.H., "Influence of Li Content and Aging Treatment on the Mechanical Properties of Al-Li-Cu Alloys," presented at the AIME Annual Meeting, New York, 1985 February.
46. Suresh, S., "Fatigue Crack Deflection and Fracture Surface Contact Micromechanical Models," Met. Trans., Vol. 16A, 1985, p. 249.

APPENDIX A

CONSTANT AMPLITUDE FATIGUE CRACK GROWTH RATE,
 da/dN VERSUS ΔK

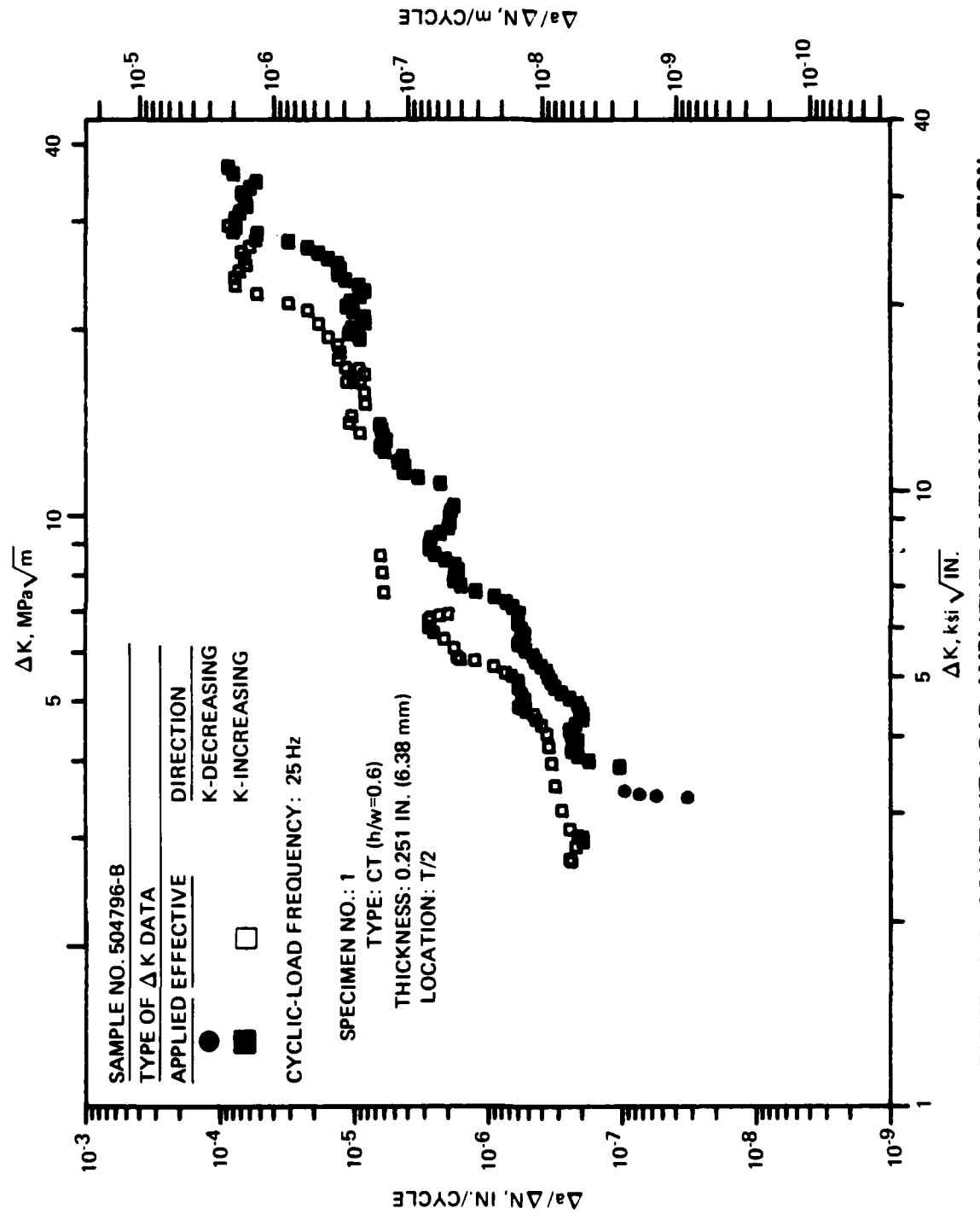


FIGURE A-1. CONSTANT-LOAD-AMPLITUDE FATIGUE CRACK PROPAGATION DATA FOR LABORATORY FABRICATED ALUMINUM ALLOY 321CU PLATE, 0.300 IN. (7.62 mm) THICK L-T ORIENTATION, R-RATIO = +0.33, HIGH HUMIDITY (R.H. > 90%) AIR

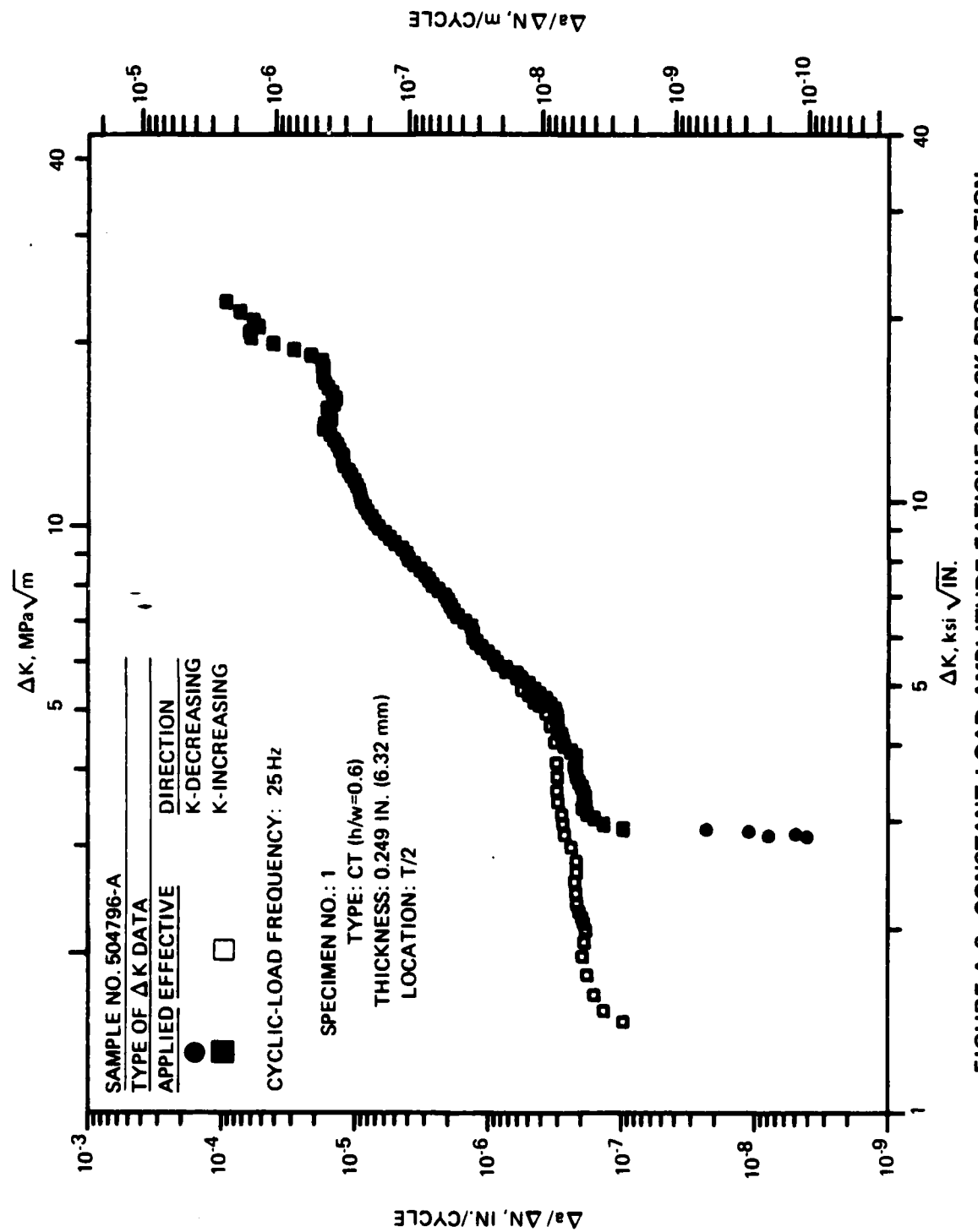


FIGURE A-2. CONSTANT-LOAD-AMPLITUDE FATIGUE CRACK PROPAGATION DATA FOR LABORATORY FABRICATED ALUMINUM ALLOY 321C8 PLATE,
 0.300 IN. (7.62 mm) THICK L-T ORIENTATION, R-RATIO = +0.33,
 HIGH HUMIDITY (R.H. > 90%) AIR

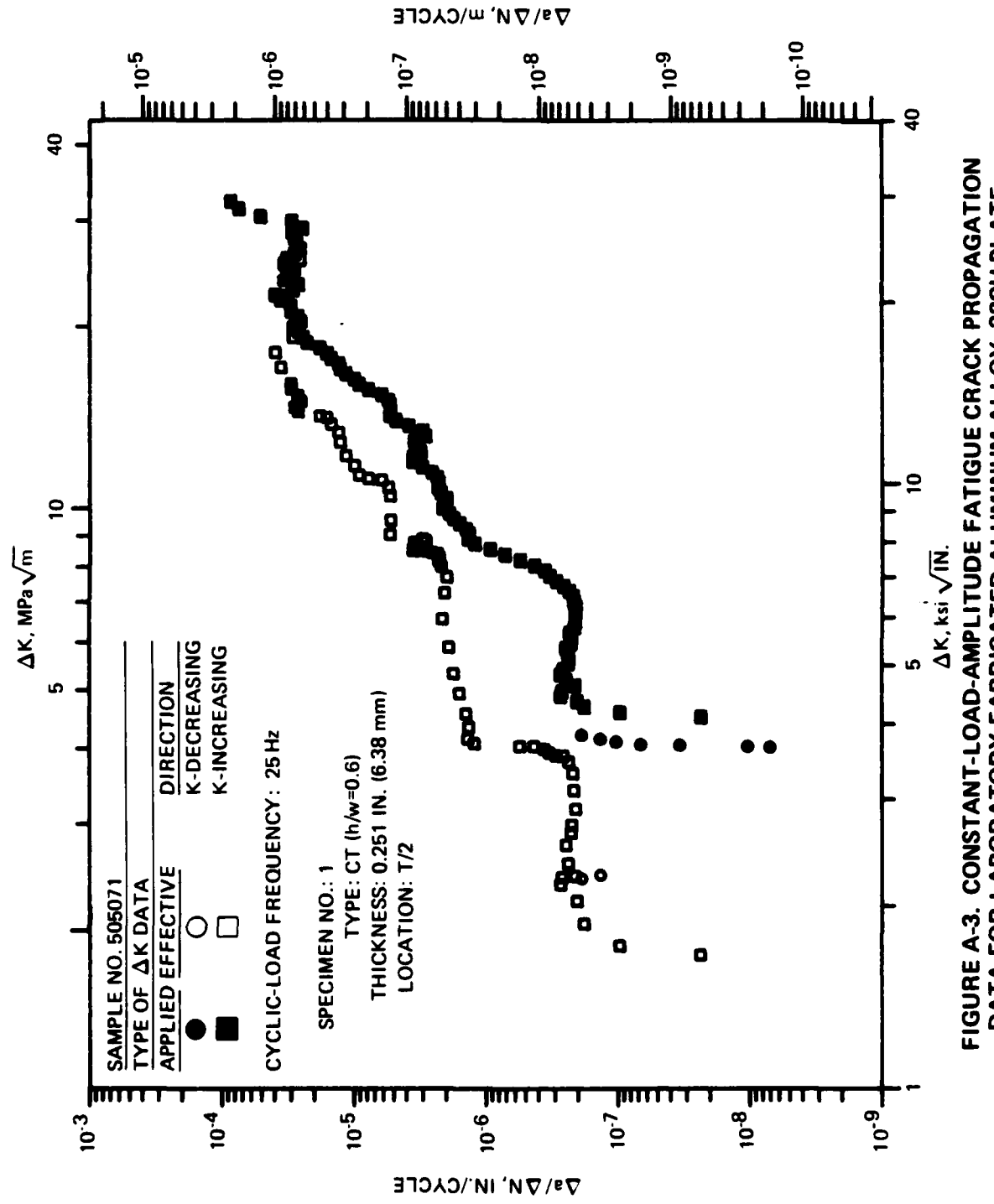


FIGURE A-3. CONSTANT-LOAD-AMPLITUDE FATIGUE CRACK PROPAGATION DATA FOR LABORATORY FABRICATED ALUMINUM ALLOY 32CUPLATE, 0.300 IN. (7.62 mm) THICK L-T ORIENTATION, R-RATIO = +0.33, HIGH HUMIDITY (R.H. > 90%) AIR

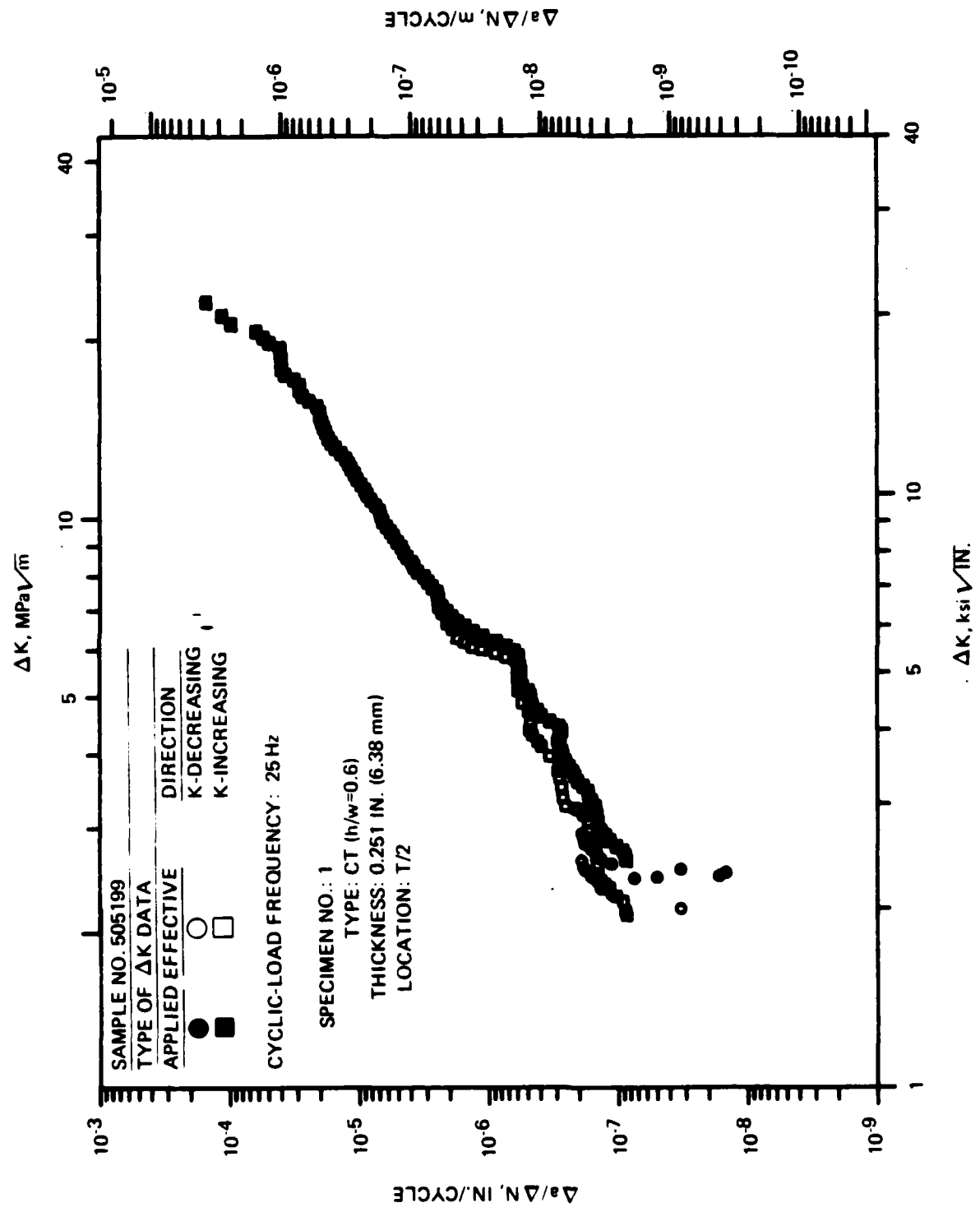


FIGURE A-4. CONSTANT-LOAD-AMPLITUDE FATIGUE CRACK PROPAGATION DATA FOR LABORATORY FABRICATED ALUMINUM ALLOY 32C8 PLATE, 0.300 IN. (7.62 mm) THICK L-T ORIENTATION, R-RATIO = +0.33, HIGH HUMIDITY (R.H. > 90%) AIR

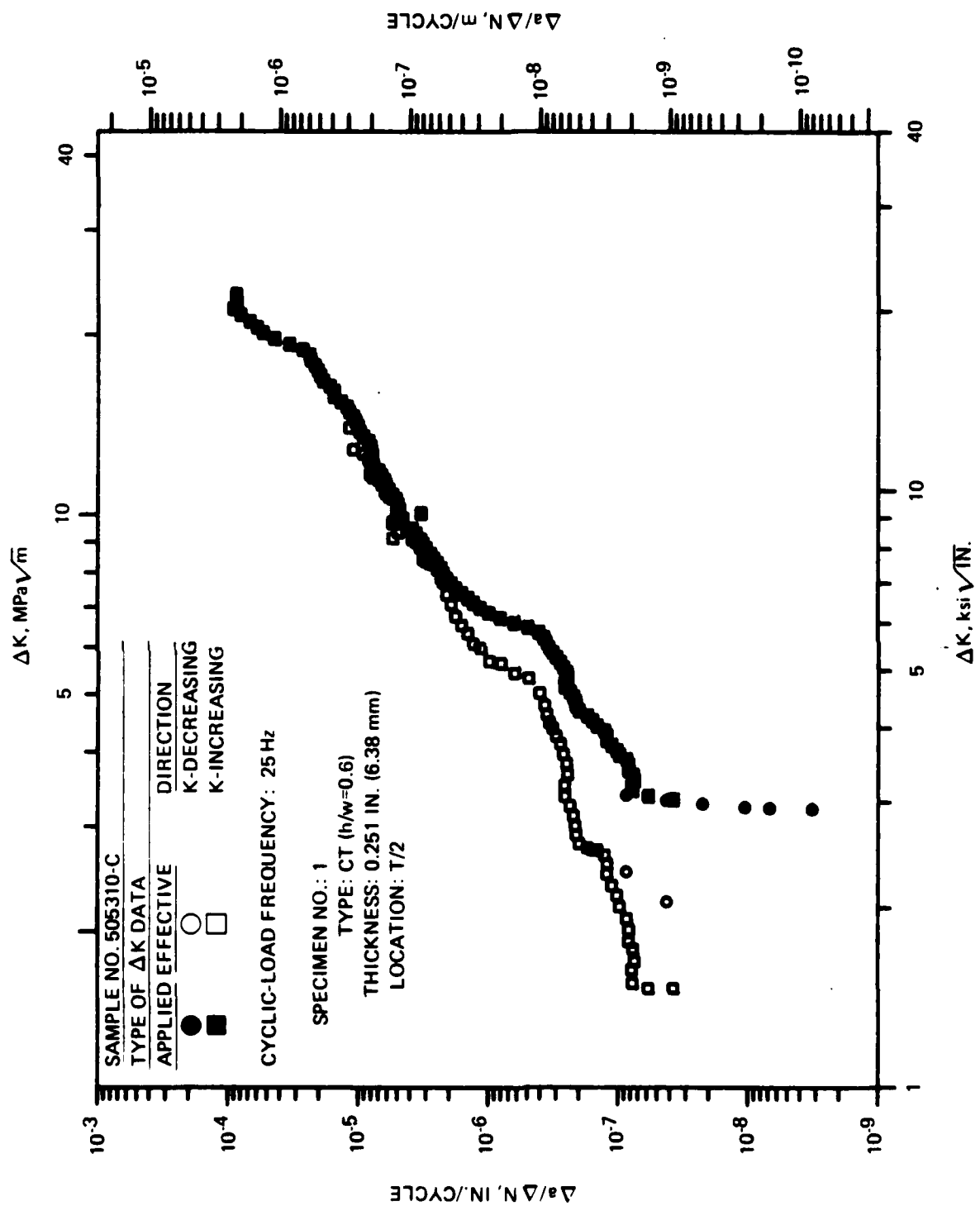


FIGURE A-5. CONSTANT-LOAD-AMPLITUDE FATIGUE CRACK PROPAGATION DATA FOR LABORATORY FABRICATED ALUMINUM ALLOY 32M1 PLATE, 0.300 IN. (7.62 mm) THICK L-T ORIENTATION, R-RATIO = +0.33, HIGH HUMIDITY (R.H. > 90%) AIR

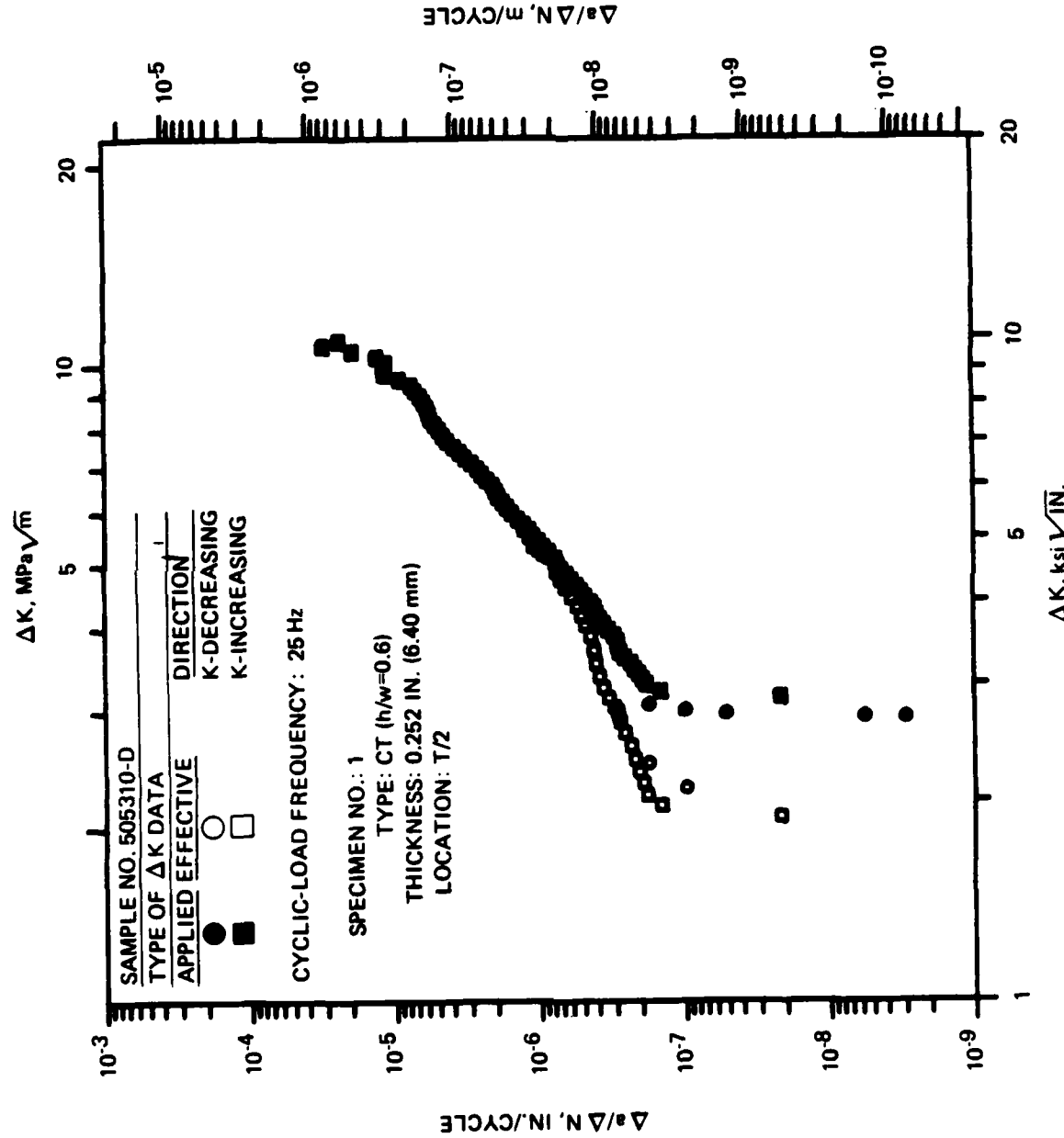
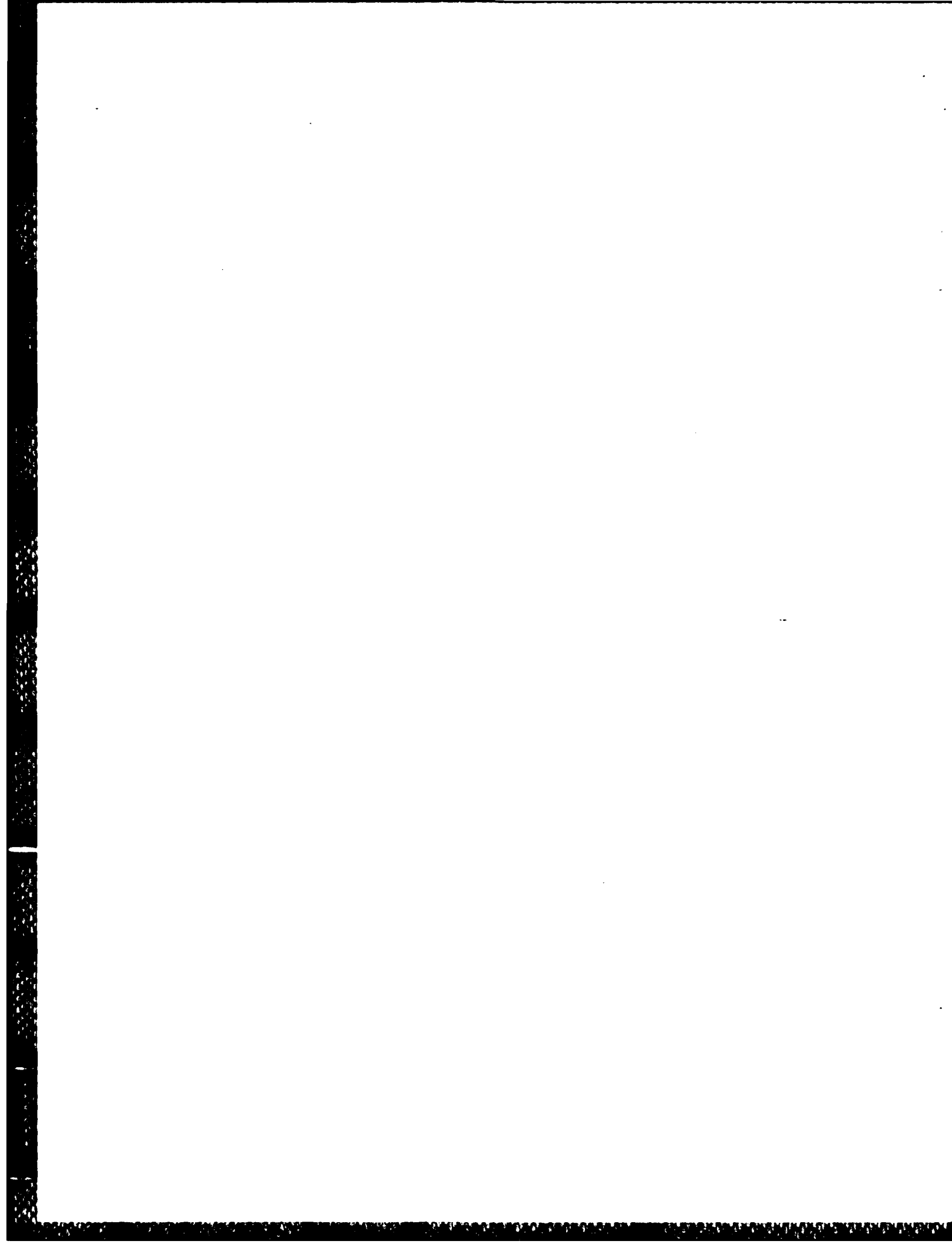


FIGURE A-6. CONSTANT-LOAD-AMPLITUDE FATIGUE CRACK PROPAGATION DATA FOR LABORATORY FABRICATED ALUMINUM ALLOY 32M6 PLATE, 0.300 IN. (7.62 mm) THICK L-T ORIENTATION, R-RATIO = +0.33, HIGH HUMIDITY (R.H. > 90%) AIR



APPENDIX B

CRACK LENGTH VERSUS SIMULATED FLIGHT HOURS a VERSUS H

1. The scale for the ordinate (a) is the same for each graph; the scale for the abscissa (H) varies, and to make comparisons easier, the abscissa was adjusted so that a crack length of 6 mm corresponded to zero simulated flight hours.
2. Data are in numerical order by alloy designation with TD spectrum first, then TC spectrum.
3. The tension-dominated (TD) spectrum representing the lower wing root load history of the F-18 is coded C2 at Northrop and the tension-compression (TC) spectrum representing the horizontal hinge tail moment load history is coded E3. The TDR, TCR and TCZ spectrums, which are modifications of the TD and TC spectrums, are coded TDR25, SCARC2 and F18E3A.
4. Crack length was measured at the end of one or more passes (300 simulated flight hours per pass) of the spectrum, which at the beginning of the 103 and 145 MPa tests resulted in the crack growth increment being less than 0.25 mm which is required by ASTM E647. (Note that ASTM E647 is a method for constant amplitude fatigue crack growth.) However, in calculating crack growth rates, the 0.25 mm increment requirement was observed. At the higher crack growth rates, the one per pass crack measurement resulted in larger crack growth increments than required by ASTM E647.
5. Graphs were plotted using a Northrop Support Services Laboratory computer program designated \$DDNPT1 from data on files designated .DDN, created from crack length measurement versus pass raw data.

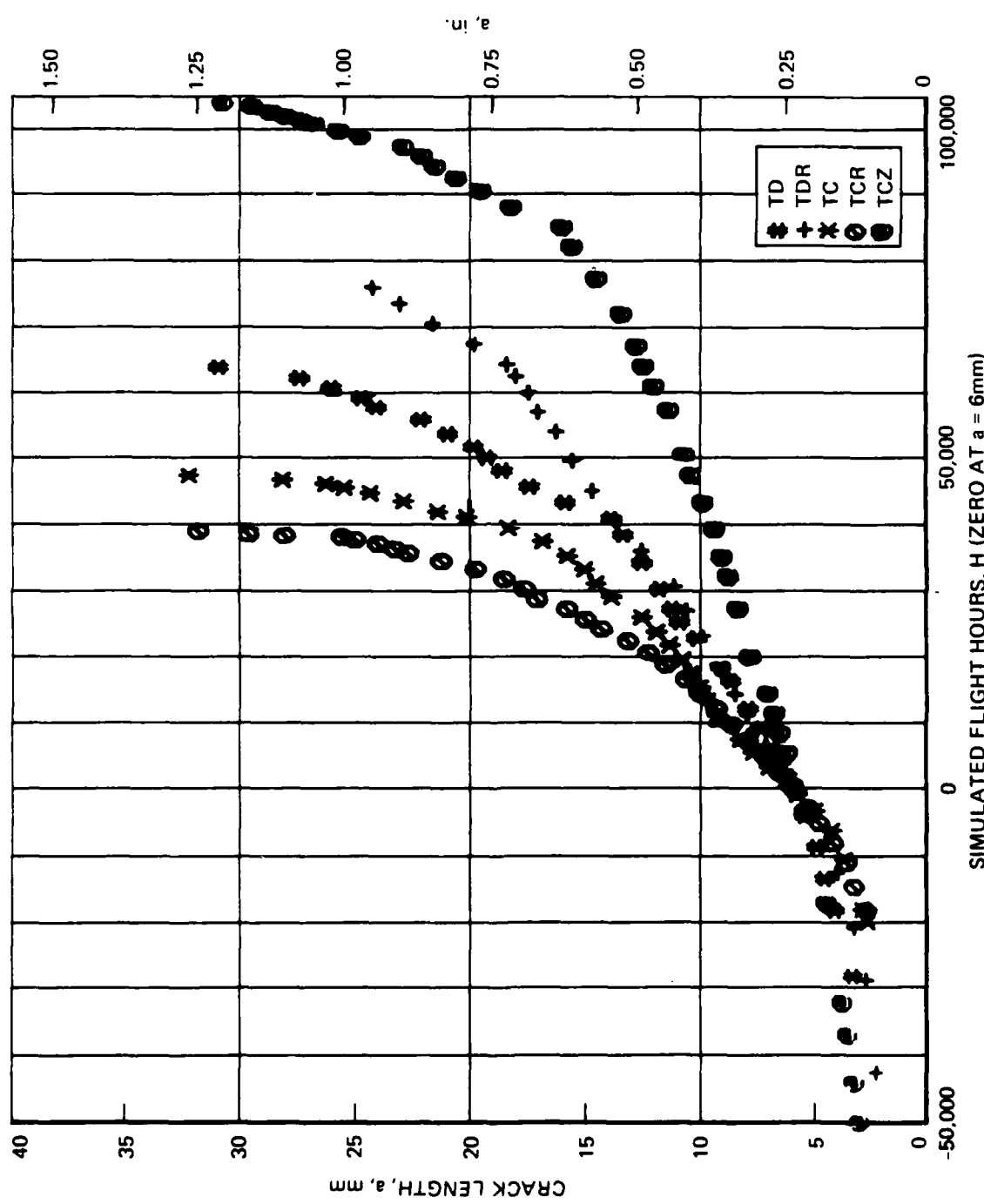


FIGURE B-1. 321CU

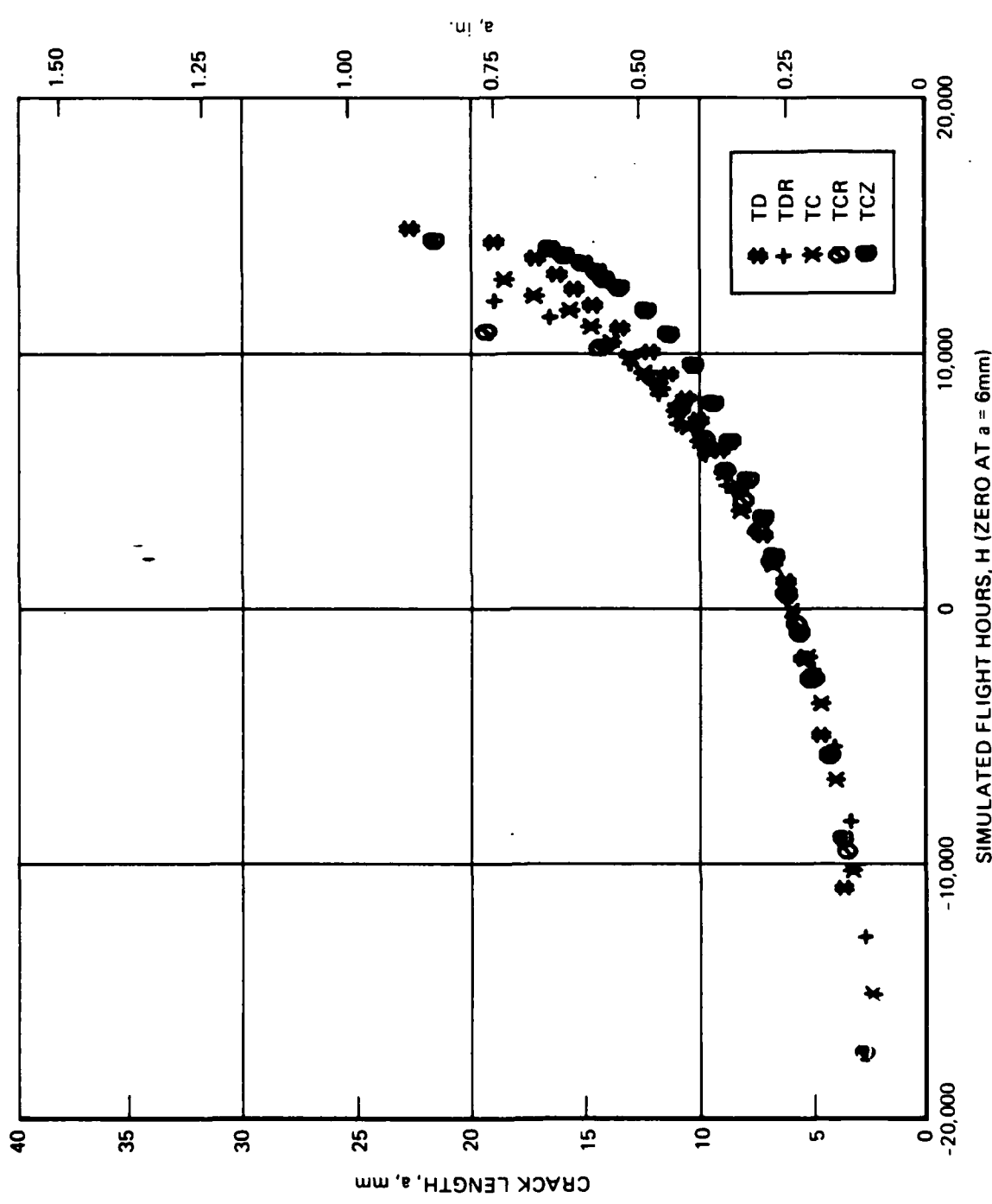


FIGURE B-2. 321C8

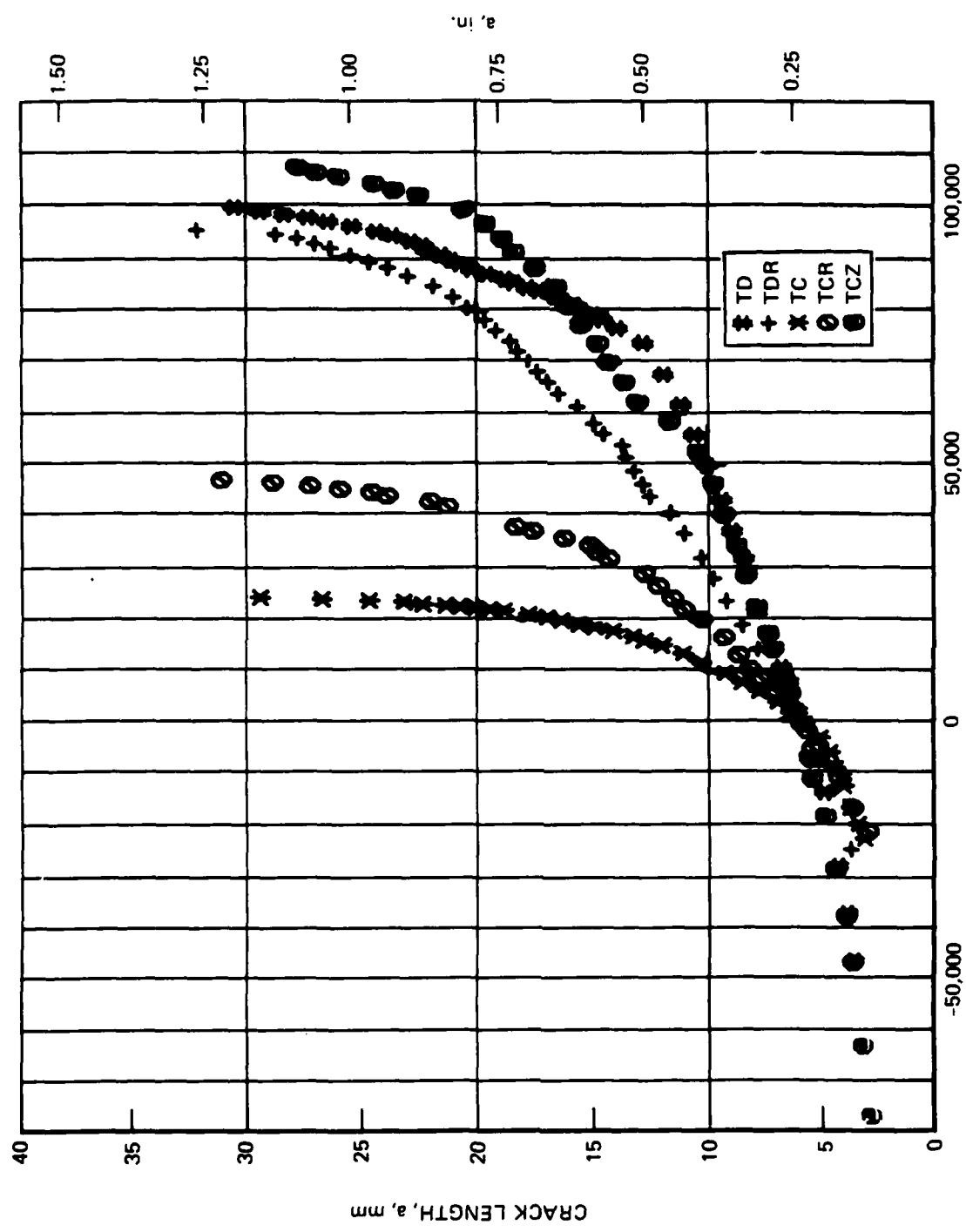


FIGURE B-3. 32CU

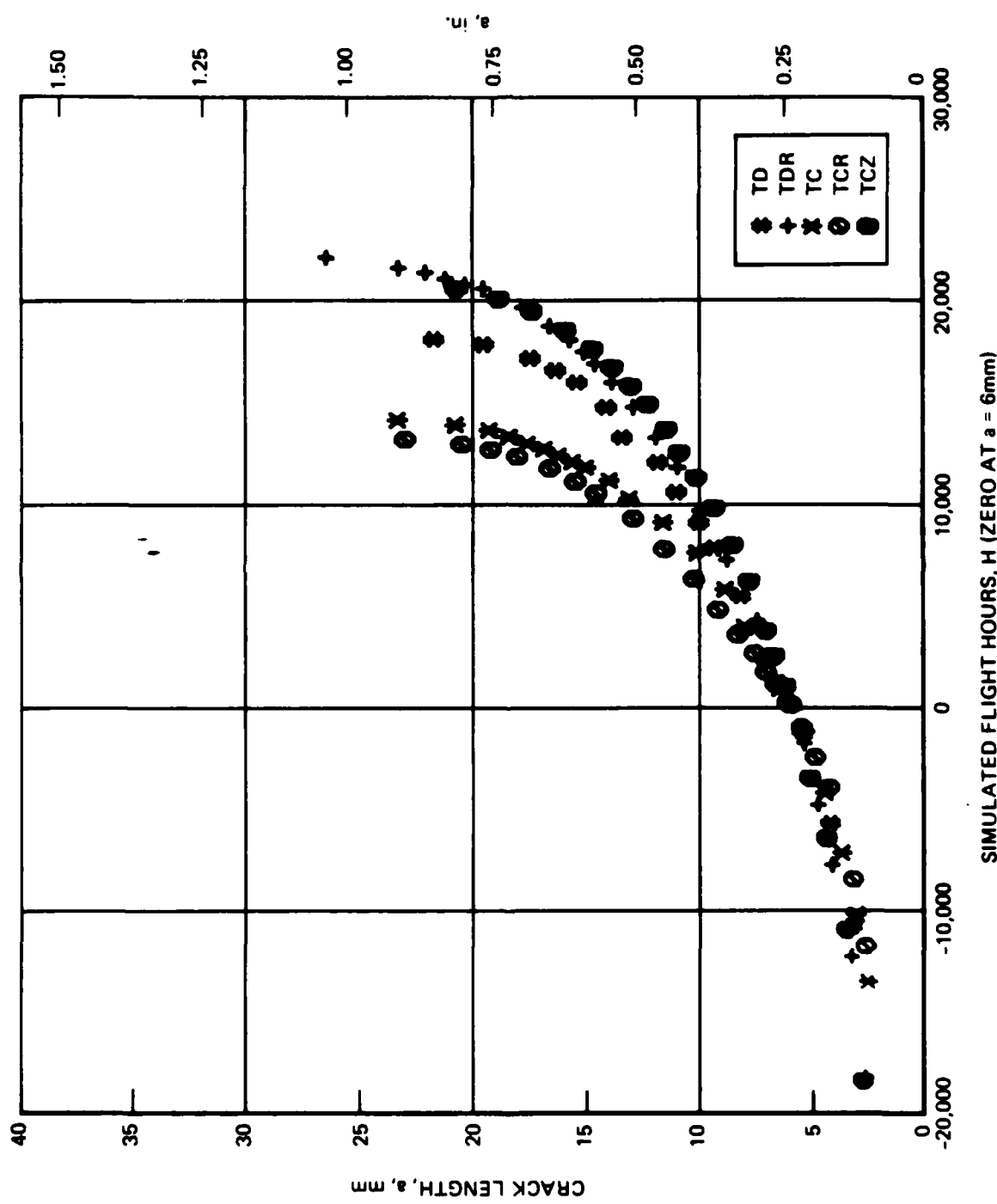
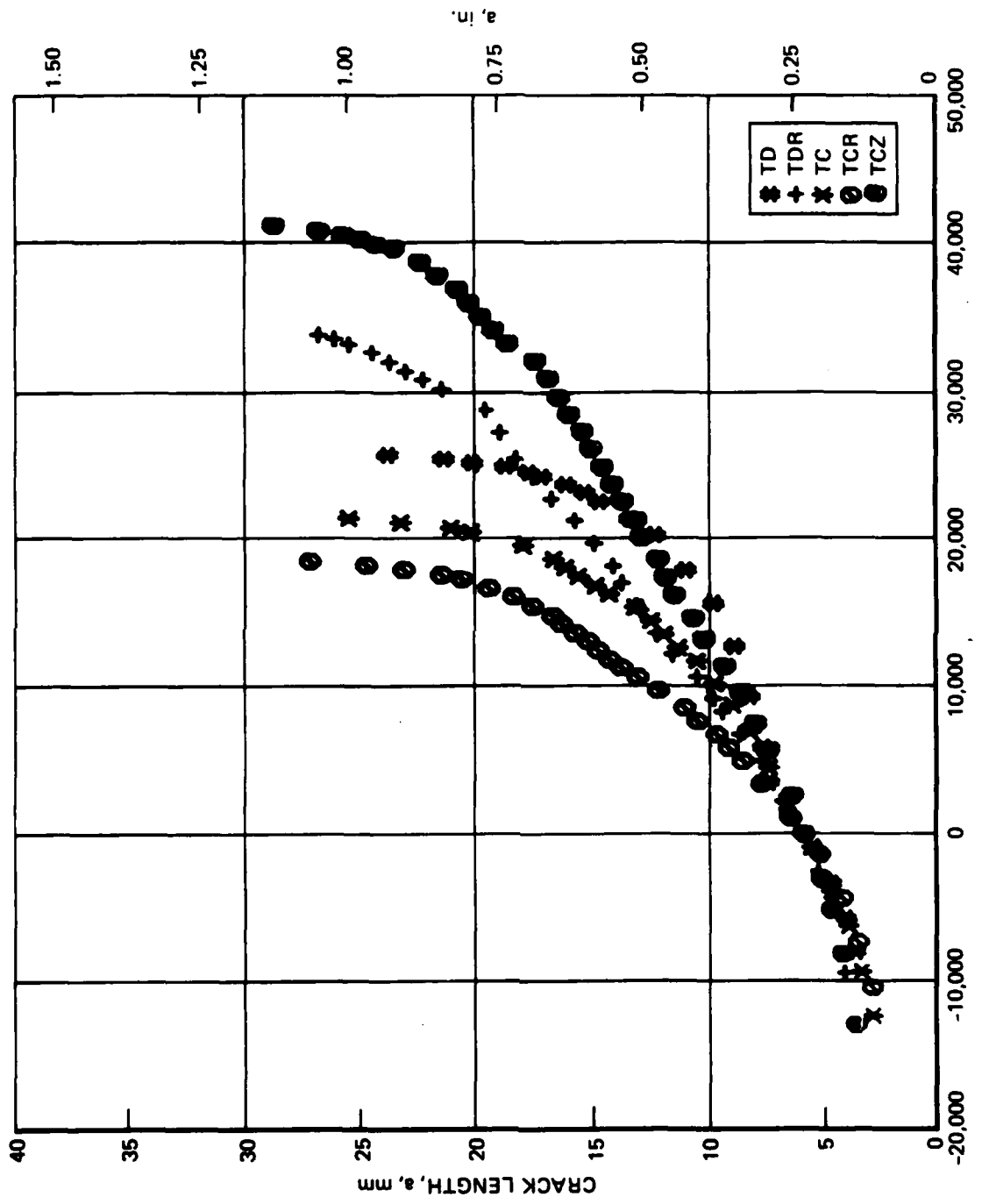


FIGURE B-4. 32CB



SIMULATED FLIGHT HOURS, H (ZERO AT $a = 6\text{mm}$)

FIGURE B-5. 32MU

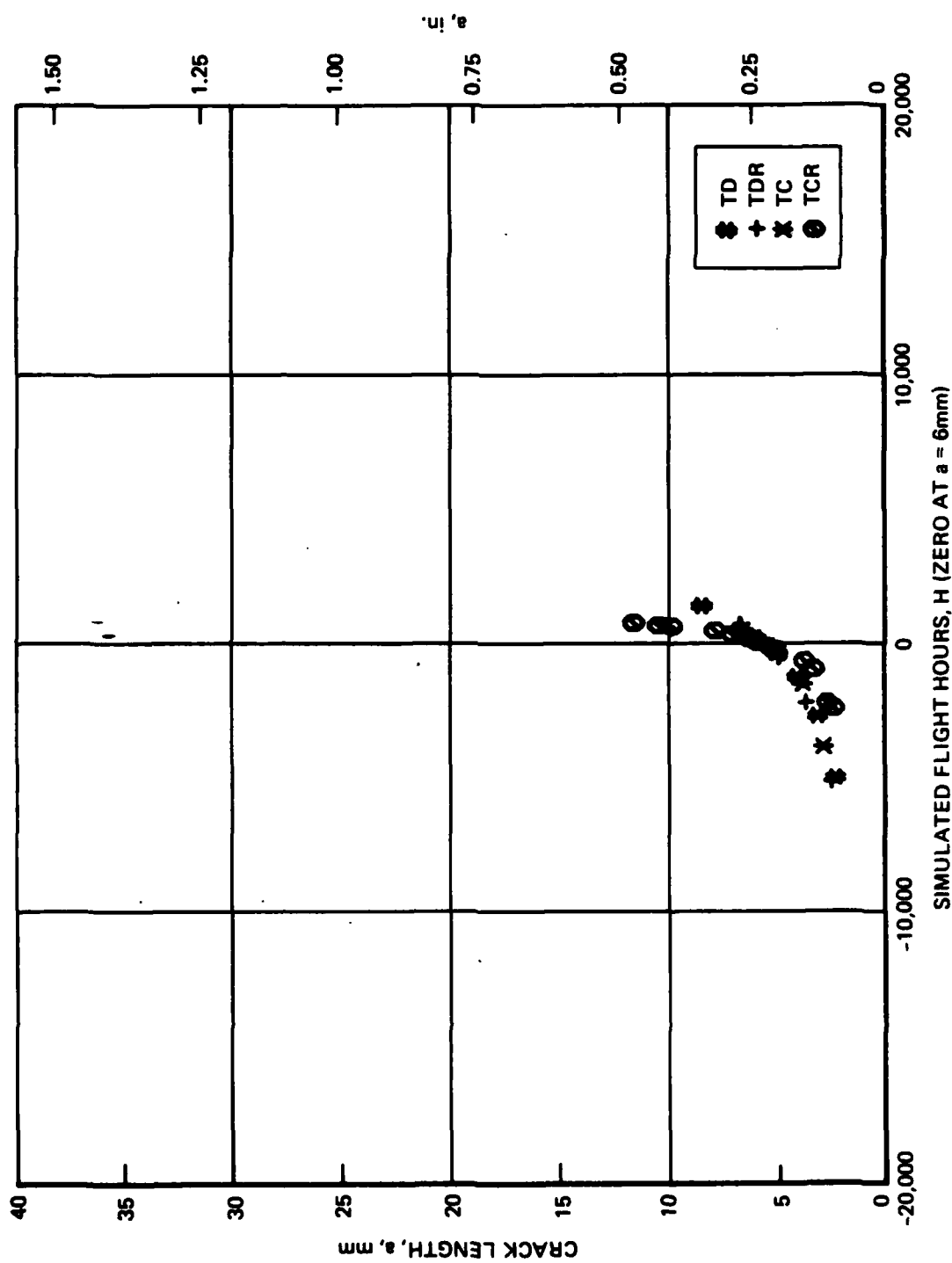


FIGURE B-6. 32MB

APPENDIX C

SPECTRUM CRACK GROWTH RATE VERSUS MAXIMUM PEAK STRESS INTENSITY da/dH VERSUS K_{hmax}

1. The scales for both axes are identical on each graph.
2. Crack growth rates are calculated by two-point secant method per ASTM E647 based on the data in Appendix B, and applying the ASTM E647 requirement that the minimum crack growth interval, a , be greater than or equal to 0.25 mm. This is performed using Northrop Support Services Laboratory computer program designated \$FITPTO from data on files designated .DDN, created from crack length measurement versus pass raw data. The data are plotted with a program designated \$SPCPT1.

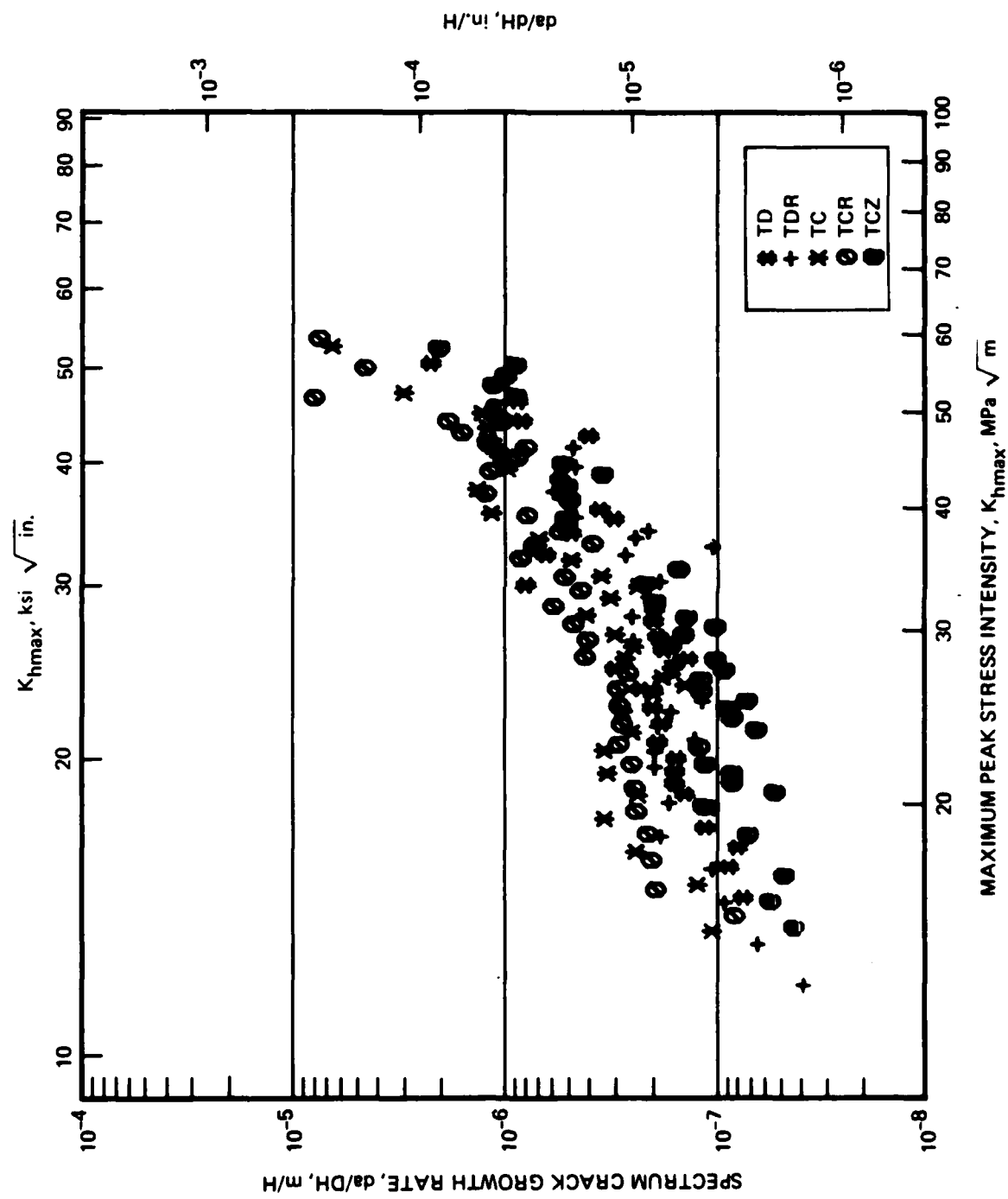
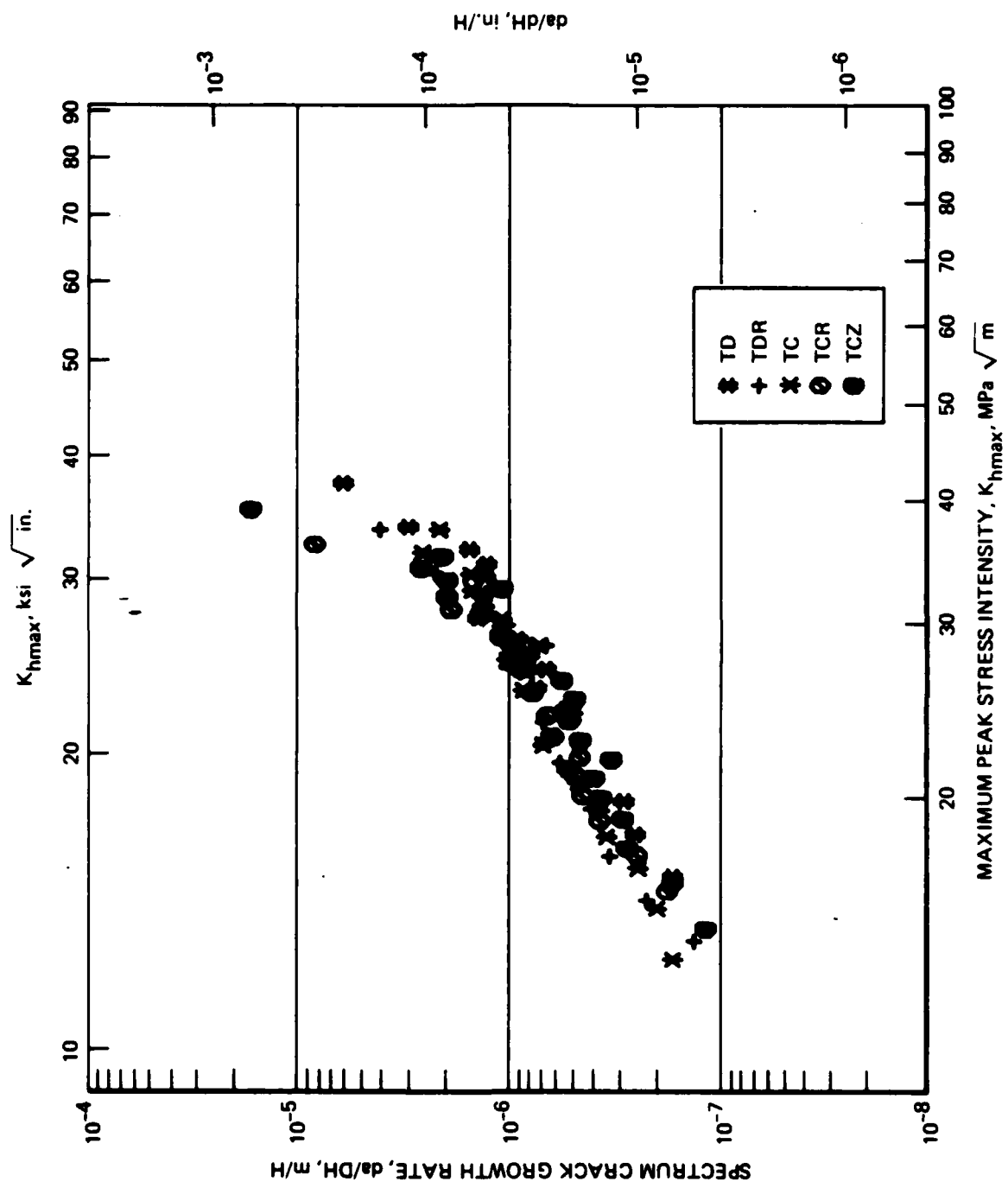


FIGURE C-1. 321CU



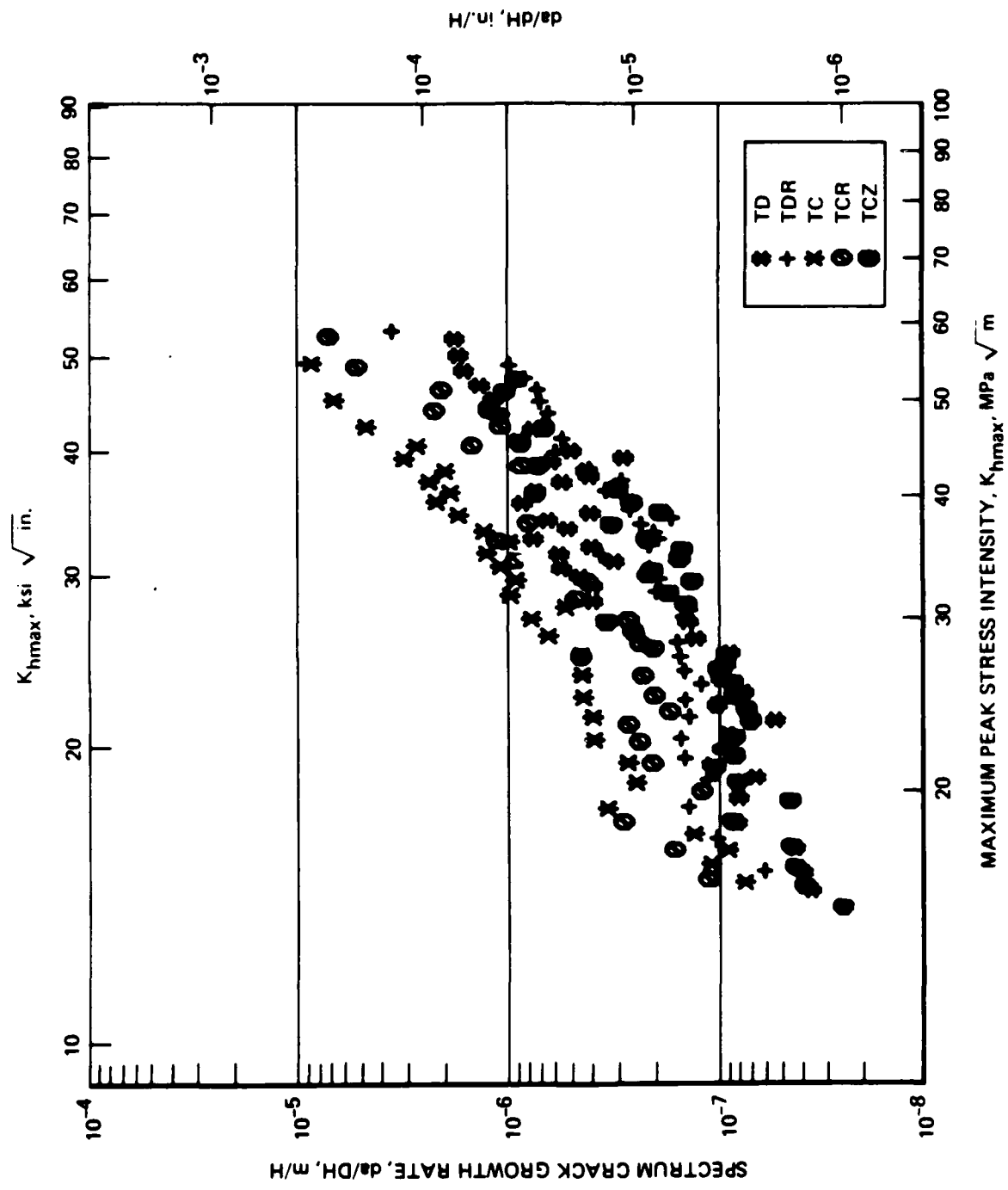


FIGURE C-3. 32CU

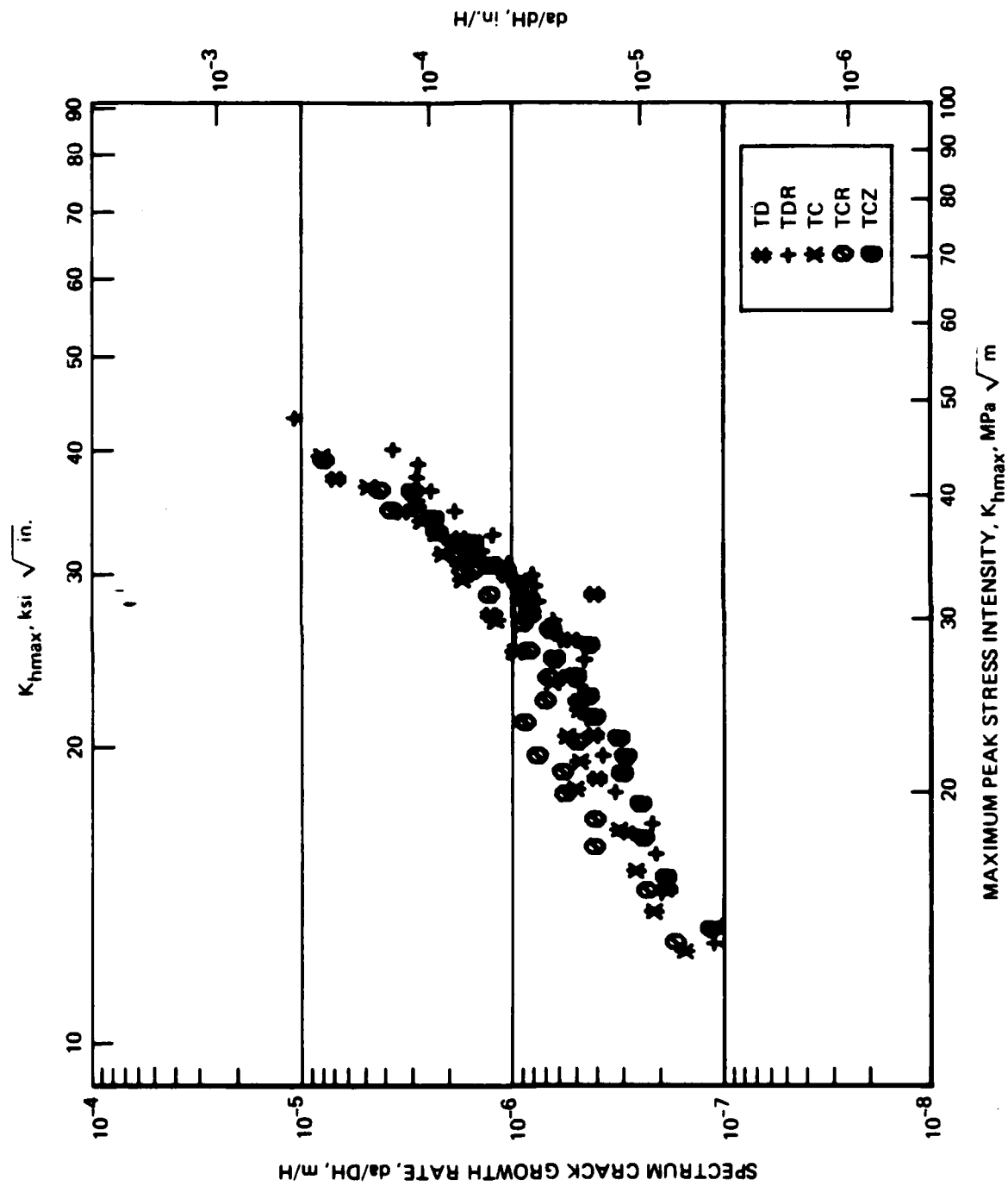


FIGURE C-4. 32C8

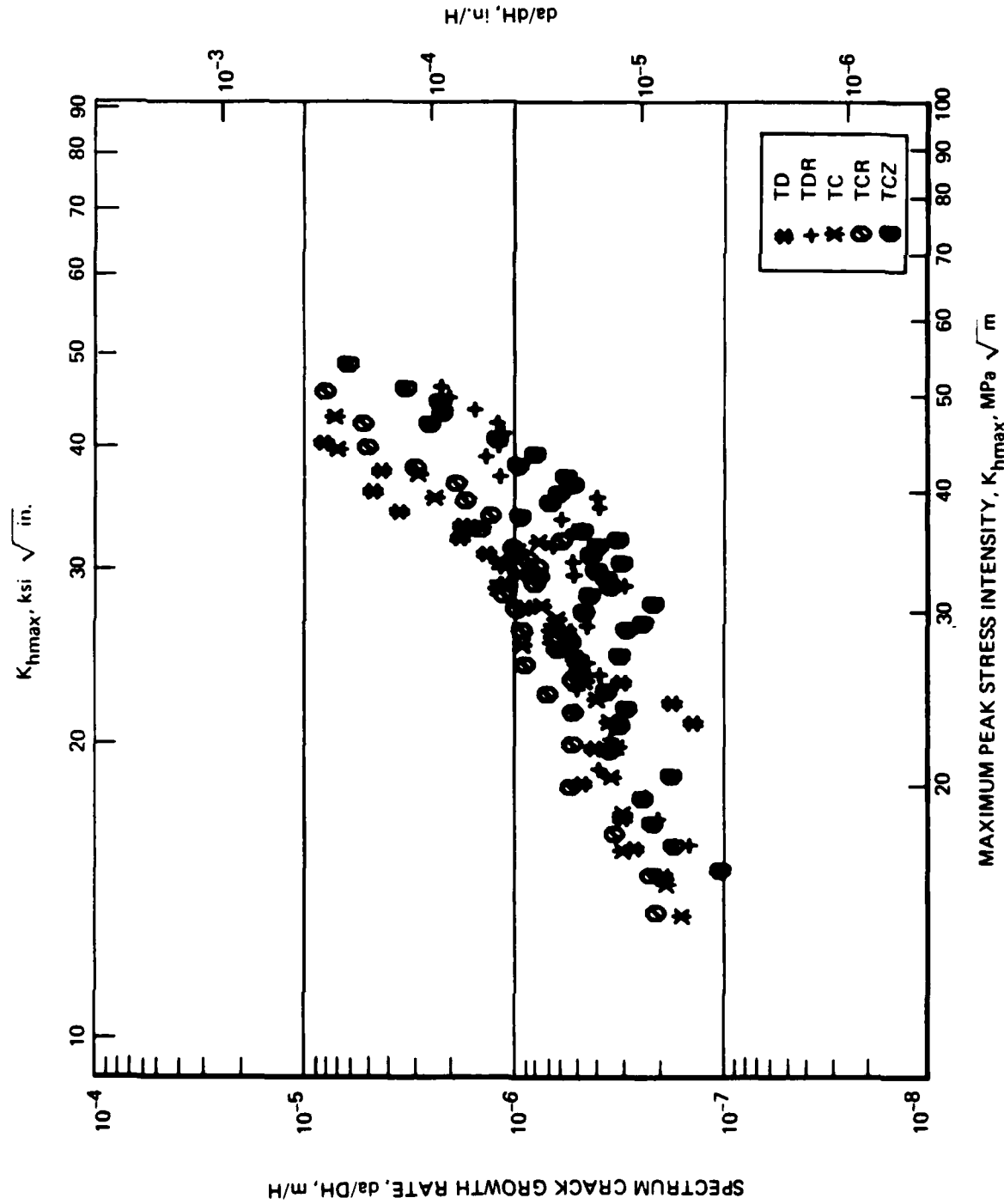


FIGURE C-5. 32MU

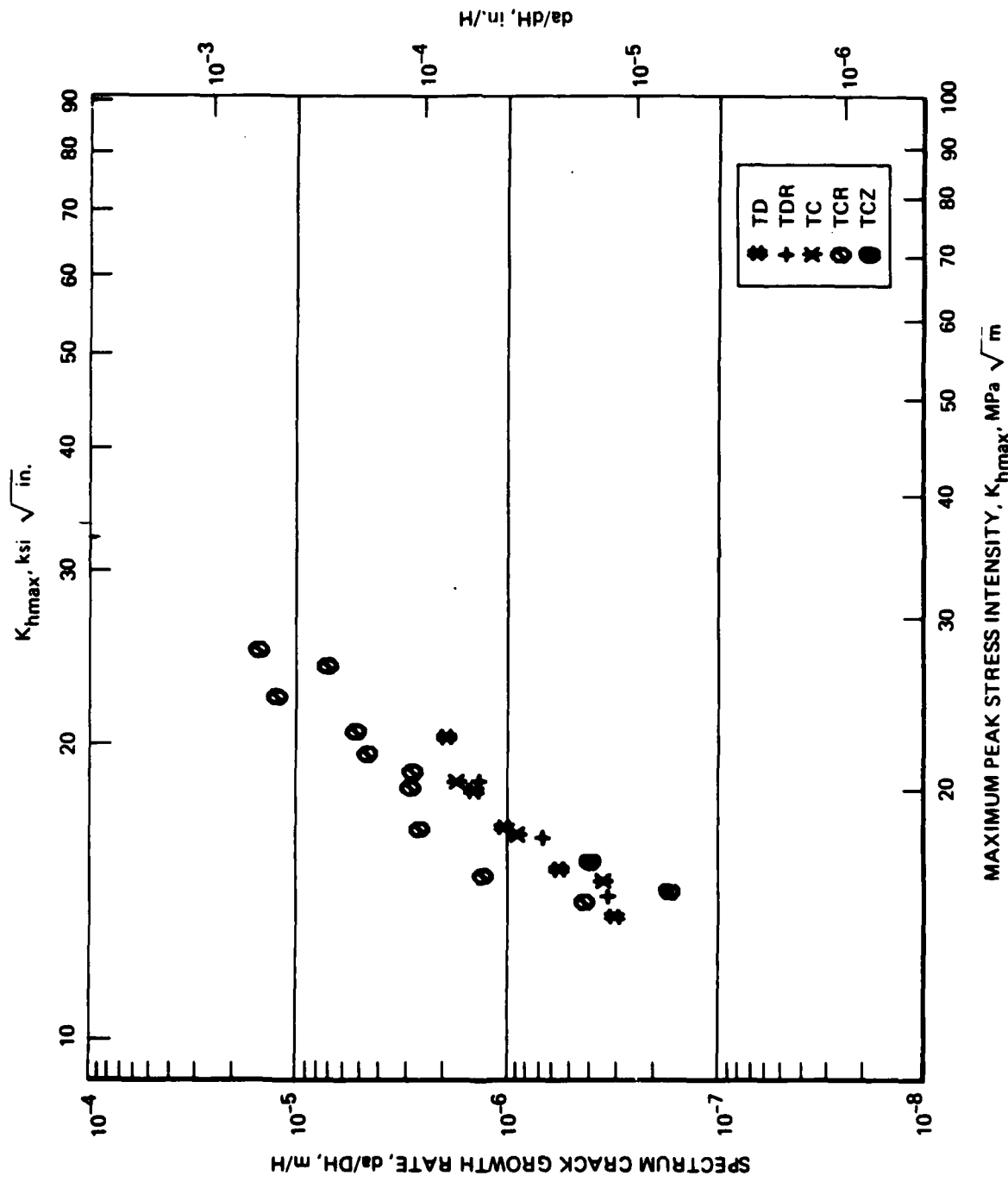


FIGURE C-6. 32MB

DISTRIBUTION LIST
(One copy only unless otherwise noted)

Commander
Naval Air Systems Command
Attn: Code AIR-5304B6 (2 copies)
Washington, D.C. 20361

AIR-7226 (4 copies)
AIR-5302 (1 copy)
AIR-310A (1 copy)
AIR-310B (1 copy)

Commander Naval Air Development Center
Attn: M. Thomas, Code 6063
(1 copy)
E. Tankins, Code 6063
(1 copy)
R. Mahorter, Code 6063
(1 copy)
Warminster, PA 18974

Commander
Naval Sea Systems Command
Code 05R -
Department of the Navy
Washington, D.C. 20361

Commander
Naval Weapons Center
Code 5516
China Lake, CA 93555

Commander
Naval Surface Weapons Center
Metallurgy Div. -R32-D. Divecha
White Oak,
Silver Spring, MD 20910

Chief of Naval Research
Code ONR 423
ONR 431
800 N. Quincy Street
Arlington, VA 22217

Director
Naval Research Laboratory
Attn: Codes 6300 (1 copy)
6370 (1 copy)
6390 (1 copy)
Washington, D.C. 20375

Air Force Wright Aeronautical Laboratory
Attn: Code LLM (1 copy)
LLN (1 copy)
Metals Branch, Mfg.
Tech Div (1 copy)
Wright-Patterson AFB
Dayton, OH 45433

Army Aviation Systems Command
P.O. Box 209
Attn: Mr. R. Vollmer-AMSAV-FRE
St. Louis, MO 63166

Army Research & Tech. Lab
Applied Technology Lab
DAVDL-ATL-ATS
Attn: T. Mazza
Ft. Eustis, VA 232604

Army Research Office
Box CM, Duke Station
Attn: Metallurgy & Ceramics Div
Durham, NC 27706

Army Mat'l's & Mech. Research Ctr
Attn: Dr. George Thomas
Watertown, MA 02171

Defense Advanced Research Project Agency
Attn: Dr. B.A. Wilcox Code 641
1400 Wilson Boulevard
Arlington, VA 22209

NASA
Ames Research Center
Code 240-10
Moffett Field, CA 94035

NASA Jet Propulsion Laboratory
4800 Oak Grove Drive
Pasadena, CA 91103

NASA
Langley Research Ctr
Attn: R.A. Pride
Langley Station, MS 15d
Hampton, VA 23365

Air Force Office of
Scientific Research
Dept. of the Air Force
Bolling Air Force Base
Washington, D.C. 20322

U.S. Department of Energy
Division of Reactor Research
& Technology
Attn: A. Van Echo
Mail Station B-107
Washington, D.C. 20545

National Academy of Sciences
National Materials Advisory Board
2101 Constitution Ave.
Attn: Dr. J.C. Lane
Washington, D.C. 20418

National Science Foundation
1800 G St., N.W.
Washington, D.C. 20550

Battelle Memorial Institute
Mfg. & Design Interaction
Attn: Dr. Bryan R. Noton
505 King Ave.
Columbus, OH 43201

Bell Helicopter Co.
Adv. Sys. Programs
Attn: James Kenna
P.O. Box 482
Ft. Worth, TX 76101

The Boeing Company
Aerospace Division
P.O. Box 3707, M/S 73-43
Attn: Mr. Rod Boyer
Seattle, WA 98124

Boeing Company
Vertol Division/MS P62-06
Attn: R. Pinckney
P.O. Box 95006
Philadelphia, PA 19142

EXXON Materials Division
Attn: Jerry Dixon
P.O. Box 95006
Raleigh, NC 27625

NASA
Marshall Space Flight Ctr
Attn: R. Schwinghamer
Huntsville, AL 35812

General Dynamics
Attn: C.F. Herndon
P.O. Box 748, MS 2830
Ft. Worth, TX 76101

General Dynamics Materials
Research
Attn: W.G. Scheck
P.O. Box 80847, MZ 640-00
San Diego, CA 92138

Grumman Aerospace Corp.
MS AD-12, Materials & Proc. Dept.
Attn: R.J. Herizman
South Oyster Bay Road
Bethpage, NY 11714

Grumman Aerospace Corp.
Ad. Mtls & Process Div.
Attn: Carl Micillo
Dept. 447, Plan 12
Bethpage, NY 11714

Hughes Aircraft Co.
Components & Materials Lab
Attn: L.B. Keller
Bldg. 6, Main Station, D-134
Culver City, CA 90230

Kaman Aerospace Corp.
Matl's & Process Engineering
Attn: A.S. Falcone
Old Windsor Road
Bloomfield, CT 06002

LTV Aerospace Corp.
Vought Systems Division
P.O. Box 5907
Attn: Mr. A.E. Hohman, Jr.
Dallas, TX 75222

Lockheed California Co.
Department 76-31 Bldg. 63
Attn: R. Kaseko/J. Pengra
Burbank, CA 91520

Lockheed Missile & Space Co., Inc.
Dept. 86-73
Attn. F.B. Yarborough
P.O. Box 504, Bldg. 153
Sunnyvale, CA 94088

Martin Marietta Corp.
Denver Division
Attn: Dr. A. Feldman
P.O. Box 179, MZ 1630
Denver, CO 80201

McDonnell Douglas Aircraft Co.
Mrg. R&D Dept (MS1-22)
Attn: Robert Zwart
3855 Lakewood Blvd.
Long Beach, CA 90846

McDonnell Douglas Corporation
Engineering Division
Attn. B.B. Leonard
5301 BOLSA/MS A3-248/13-3
Huntington Beach, CA 92847

McDonnell Douglas Research Labs
P.O. Box 516
Attn: Dr. D.F. Ames
Dr. Charles Whitsett
St. Louis, MO 63166

Northrop Corporation
Attn: E. Jaffe
One Northrop Ave
Hawthorne, CA 90250-3277

Rockwell International Corp.
Attn. M. Mahoney
Science Center
1049 Camino Dos Rios
Thousand Oaks, CA 91830

Sikrosky Aircraft
Mfg. Engineering Dept.
Attn. J.D. Ray
North Main Street
Stratford, CT 06602

United Technologies Company
Research Center
400 Main Street
East Hartford, CT 06108

Kaiser Aluminum Chemical Corporation
Aluminum Division of Research
Center for Technology
P.O. Box 870
Pleasanton, CA 94566
Attn: T.R. Prichett

Reynolds Metals Company
Metallurgical Research Division
4th and Canal Streets
Richmond, CA 23219
Attn: Dr. Grant Spangler

Professor R. Ritchie
Department of Materials Science
and Mineral Engineering and
Lawrence Berkeley Laboratory
University of California
Berkeley, CA 94720

Professor S. Suresh
Brown University
Division of Engineering
Providence, RI 02912

Dr. E.A. Starke, Jr.
School of Engineering and Applied
Science
University of Virginia
Charlottesville, VA 22903

Prof. A.J. McEvily
Department of Metallurgy
U-136
University of Connecticut
Storrs, CT 06268

Southwest Research Institute
8500 Culebra Road
P.O. Box 28510
San Antonio, TX 78284
Attn: Mr. J. Fitzgerald
Dr. D. Davidson

Aluminum Company of America
1200 Ring Bldg.
Washington, D.C. 20036
Attn: Mr. G. Barthold

Aluminum Company of America
Alcoa Center, PA 15069
Attn: Mr. Paul L. Mehr

D. Brook
123 Meadow Drive
Patafkala, OH 43062

Roy L. Hewitt, P. Engr., PhD.
Research Officer
Structures and Materials
Laboratory
National Aeronautical
Establishment
Montreal Road
Ottawa, Canada
K1A OR6

Prof. J. Schijve
Delft University of Technology
Dept of Aerospace Engineering
P.O. Box 5058
2600 GD Delft
The Netherlands

Anders F. Blom, PhD.
The Aeronautical Research
Institute of Sweden
P.O. Box 11021
S-161 11 Bromma, Sweden

Douglas Aircraft Company
3855 Lakewood Blvd.
Long Beach, CA 90808
Attn: P.R. Abelkis
Mail Code 36-90
Dept. C1-E84

Douglas Aircraft Company
3855 Lakewood Blvd.
Long Beach, CA 90846
Attn: Dr. David Cho
Mail Code W5-20

Dr. Richard Hertzberg
Lehigh University
Bethlehem, PA 18015

Metals & Ceramics Info. Center
Battelle, Columbus Laboratories
505 King Avenue
Columbus, OH 43201

END

6 - 81

DTIC